INVESTIGATION OF CADMIUM ZINC TELLURIDE DETECTOR FOR MEDICAL IMAGING APPLICATIONS

INVESTIGATION OF CADMIUM ZINC TELLURIDE DETECTOR FOR MEDICAL IMAGING APPLICATIONS

By

Xiaoqing Zheng

B.A.Sc. Xi'an Jiaotong University, 2009

M.A.Sc. Xi'an Jiaotong University, 2012

A Thesis

Submitted to the School of Graduate

Studies in Partial Fulfillment of the

Requirements for the Degree of

Doctor of Philosophy

McMaster University

Hamilton, Ontario, Canada

Doctor of Philosophy (2017) McMaster University

(Electrical and Computer Engineering) Hamilton, Ontario

TITLE:	Investigation of Cadmium Zinc Telluride Detector for Medical Imaging Applications
AUTHOR:	Xiaoqing Zheng, B.A.Sc. Xi'an Jiaotong University, Xi'an, China M.A.Sc. Xi'an Jiaotong University, Xi'an, China
SUPERVISOR:	Prof. M. Jamal Deen
NUMBER OF PAGES:	154

Abstract

The wide band gap semiconductor Cadmium Zinc Telluride (CZT) is of recent interest for medical imaging at room temperature. A number of properties, including superior energy resolution, 3D photon position sensitivity, compact size, direct photon conversion and energy-resolving capability, make CZT a promising candidate for positron emission tomography (PET) and photon-counting X-ray imaging systems. Despite these advantages, drawbacks, such as low mobility of holes, hole trapping, charge sharing effect and characteristic X-ray escape degrade the performance of large volume CZT detectors.

In this research, characterization and evaluation of single-crystal CZT photon detector using simulation and experimental studies were done. First, a comprehensive analytical model was developed and implemented by using Monte Carlo simulation and finite element analyses. This model includes the generation and transportation of charge carries within CZT detectors, and it provides useful guidance in optimizing the electrode design and associated readout circuits.

Second, the performance of a $20\times20\times5mm^3$ CZT crystal with 8×8 pixel anodes and a planar cathode was integrated with readout electronics that can be used to build a PET system was studied. The experiments demonstrate an energy resolution of ~2.26±0.84% full width half maximum (FWHM) at 662 keV and 19±3 ns coincidence time resolution with planar parallel field configuration. A novel algorithm based on charge sharing effect and transient signal analysis targeting the improvement of spatial resolution, was proposed. The sub-pitch spatial resolution is found to be ~30 μm and ~250 μm under signal-to-noise ratio of ~17, for inside and outside the valid range of charge sharing, respectively.

Finally, the feasibility of CZT in photon-counting Computed Tomography (CT) was studied by using monoenergetic sources, with a special attention paid to energy degradation due to characteristic X-ray escape and the charge sharing effect. The effects of detector configuration and incident beam location were also investigated. The results show that the pixel size can be reduced to 500 μm without significant count loss (~5%) and charge loss (~15%) for the photo-counting X-ray applications.

Acknowledgements

Firstly and foremost, I would like to express my sincere gratitude and appreciation to my supervisor, Distinguished University Professor Dr. M. Jamal Deen. It's a great opportunity and precious experience to join his group and learn knowledge from his brilliant mind. Being always motivational and supportive, Dr. Deen has helped, encouraged and guided me throughout my Ph.D. research work. He is a role model to me, from professional research, to teaching and to personal aspect. It has been such a pleasure to work with someone so enthusiastic and knowledgeable in the fields of both electrical engineering and biomedical engineering.

I would like to express my deepest appreciation and thanks to my co-supervisor, Professor Hao Peng, who has been a great teacher, friend, and mentor, as well as a steadfast source of support and encouragement to me. He led me into the domain of nuclear medical, guided me through the project and assisted me in every possible aspect.

I would also like to thank my committee members, Professor Nicola Nicolici and Professor Chih-Hung Chen for their insightful instructions and advices during my Ph.D. research. This work would not have been possible without their patient guidance, inspiring suggestions and continuous support.

Thanks to Dr. Zhiyun Li, Dr. Darek Palubiak, Dr. Tianyi Guo and Dr. Yiheng Qin for inspiring me with interdisciplinary knowledge and sharing experience in their expertise. Thanks to other dear colleges, Hythm Afifi, Hani Alhemsi, Mrwan Alayed, Si Pan and Sumit Majumder for lots of helpful suggestions and discussions in our weekly group meetings. It is the glad and memorable experience working together with them. I would also like thanks to the technical staff Tyler Ackland for spending lots of time helping me with the printed circuit boards used in my experiments. My thank also goes to our lovely secretary, Cheryl Gies. My studying at McMaster University cannot be such a lovely memory to me without them.

Finally, I sincerely thank my parents, my dear husband, Dr. Zeng Cheng and our baby son, Marvin Z. Cheng. Whenever I'm depressed and frustrated, their endless love and unconditional support gave me hope and encouraged me to continue to go on. I love you forever!

Table of Contents

List of Abbreviations

ADC	Analog-to-Digital Converter
APD	Avalanche Photodiode
ASIC	Application Specific Integrated Circuit
C/A Ratio	Cathode-to-Anode Ratio
CdTe	Cadmium Telluride
CFD	Constant Fraction Discrimination
CNR	Contrast-to-Noise Ratio
CS	Compton Scattering
CSA	Charge Sharing Addition
CT	Computed Tomography
CZT	Cadmium Zinc Telluride
DECT	Dual-Energy CT
DoI	Depth-of-Interaction
FDG	Fluorodeoxyglucose
FEM	Finite Element Method
FoM	Figure-of-Merit
FoV	Field-of-View
FPGA	Field-Programmable Gate Array
FWHM	Full-Width at Half-Maximum
GATE	Geant4 Application for Tomographic Emission
GUI	Graphical User Interface
HgI_2	Mercury Iodide
HPGe	High Purity Germanium
HU	Hounsfield Units
kVp	Peak kilo-Voltage
LoR	Line-of-Response

MAF	Moving Average Filter
NEC/NECR	Noise Equivalent Count Rate
NIM	Nuclear Instrumentation Module
PC	Personal Computer
PCB	Printed Circuit Board
PE	Photoelectric
PET	Positron Emission Tomography
PMT	Photomultiplier Tube
PPF	Planar Parallel Field
PTF	Planar Transverse Field
RENA	Readout Electronics for Nuclear Applications
SiPM	Silicon Photomultiplier
SNR	Signal-to-Noise Ratio
SPECT	Single-photon emission computed tomography
TlBr	Thallium bromide
VR_{CSE}	Valid Range of Charge Sharing Effect
VR_{TSA}	Valid Range of Transient Signal Analysis

List of Figures

List of Tables

Chapter 1

INTRODUCTION

CZT-based semiconductor detectors have recently attracted intensive research interests in the field of nuclear physics, gamma-ray imaging and nuclear medicine. This is due to their unique advantages such as relatively high atomic number, high density, large band-gap energy (resulting in reduced leakage current caused by less thermal carrier generation) [1]–[4], high spatial resolution through fine electrodes [5], [6], and superior energy resolution due to direct charge carrier generation/collection rather than indirect process of scintillation photon emission as in the scintillator or photomultiplier tube (PMT) modules [7]. In addition, CZT detectors have shown great promise when used as a three-dimensional positioning detector by incorporating depth of interaction (DoI) resolution, which can help mitigate the parallax error in Positron Emission Tomography (PET) systems [8], [9].

PET is a non-invasive, in vivo, imaging technology, which plays a critical role in cancer detection [10]–[13]. It utilizes radioactive tracers to generate images representing the physiology of tumors. PET is categorized as functional imaging [14], and it can visualize and quantify biological processes at the cellular and molecular levels, instead of anatomical structures. Organ dedicated PET systems, for example breast cancer detection, require higher contrast recovery and more accurate event location compared with a whole-body PET system, which makes CZT an ideal candidate for the detector technology [2].

Another widely used imaging modality for clinical diagnosis is X-ray imaging. It has been playing an important diagnostic role since the first X-ray imaging of a human hand was made by Roentgen in 1895 [15]. Several technological advancements in X-ray imaging methods have been made to produce high quality

imaging for heart disorders, cancers, and bones. In particular, the photon counting, energy-resolving capability of the CZT detector makes it possible to measure the energy of each photon, which leads to lower patient dose and shorter scan time. As a result, the photon counting CT, also known as spectral CT, is able to provide more capability than that currently available in a conventional CT [16], [17].

Nevertheless, the performance of CZT detectors suffer from several weaknesses [18], including low charge mobility, hole trapping, characteristic X-ray escape and charge diffusion. Studying these effects is a critical step to allow us to optimize the detector design and eventually improve system's performance.

In this chapter, first, we present a brief background of PET and X-ray imaging. Second, a brief review of commonly used radiation detectors is provided. Third, the motivation of this thesis is discussed, as well as the structure of the thesis and research contributions.

1.1. Positron Emission Tomography (PET) Imaging

1.1.1. PET Physics

PET is an in-vivo imaging modality that visualizes physiological processes by observing the spatial distribution and concentration of biologically active chemical compounds. A positron-emitting radionuclide must be injected into the subject prior to a PET scan. Then, anti-parallel photon pairs result from the annihilation of positrons produced in the β^+ decay of particles, such as fluorine-18 (^{18}F), oxygen-15 (^{15}O), nitrogen-13 (^{13}N) and carbon-11 (^{11}C) [19].

For example, glucose is a key source of energy for many organisms. The distribution and concentration of glucose in the organism can be used to visualize the distribution and rate of metabolism in it. A compound commonly used in PET to visualize metabolism is fluorodeoxyglucose (FDG), which is a biological analog of glucose. In FDG, one of the hydroxyl groups is replaced by the positron-emitting atom ^{18}F. The radioactive and biologically active chemical compounds such as FDG are called radiotracers [19]–[21].

After being introduced into an organism (usually by injection into the tail vein), FDG establishes a direct link between the distribution of positron radioactivity and

the rate of internal metabolism in the organism. Another example is ^{11}C, which is used in ^{11}C-L-methionine compound. It is analogous to the amino acid, which can be used to indicate cancer malignancy based on amino acid utilization [19]. A short half-life of these positron emitters is desired (i.e., ^{18}F-110 minutes, ^{15}O-2 minutes, ^{13}N-10 minutes, and ^{11}C-20.4 minutes), in order to minimize accumulated dose and imaging time [14], [22], [23].

When ^{18}F decays, 97% of the nuclear decay events result in an emitted positron and a stable ^{18}O nucleus. The emitted positron penetrates the surrounding tissue, loses energy and eventually pairs up with a tissue electron to form positronium (an unstable system of a bound positron-electron pair). Positronium can exist only briefly before the positron and electron annihilate with each other, producing two or three gamma-rays, depending on the relative spin states. However, two 511 keV photons are generated preferentially and travel anti-parallel to each other due to the conservation of momentum. [19], [24], [25].

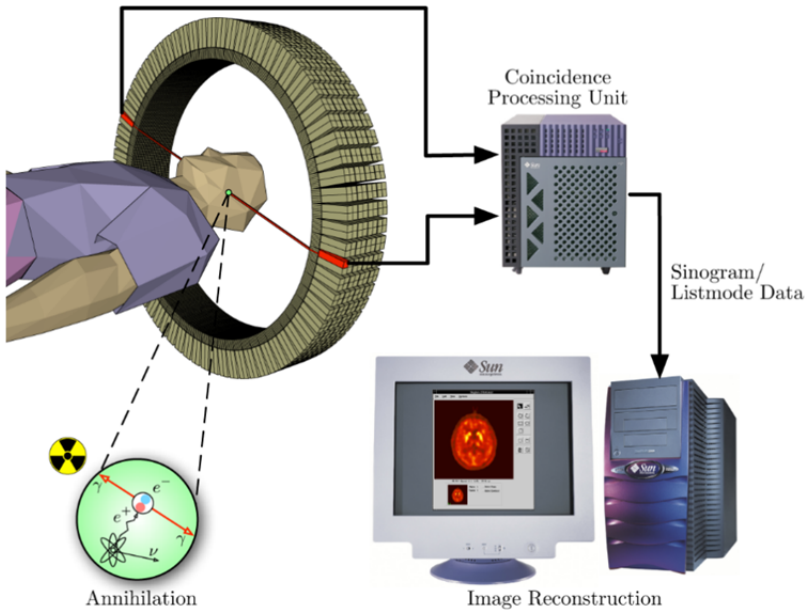

Figure 1-1, Schematic illustration of a PET imaging system. (Reprinted from [26], [27] with permission granted).

The schematic illustration of a PET imaging system is presented in Figure 1-1. A 511keV photon has an average path length of ~ 10 cm (i.e., mean free path) and thus has a high probability of escaping from a patient. If both 511 keV photons can be detected and localized in space, they form a "coincidence" event and can be traced

back to locate the position where the original emission occurs. A PET scan consists of the collection of a huge number of these coincidence events (i.e., millions). Using imaging reconstruction and data correction methods, it is possible to obtain the distribution of positron-emitting radionuclides inside an object [24].

In the coincidence detection mode (i.e., two 511 keV events trigger the detection circuit in a very narrow time window), the output signals are considered valid, and are referred to as a true coincident event. Hence, the two gamma rays in a true coincidence event are assumed to stay along the line connecting two opposed detector units and to form a line-of-response (LoR).

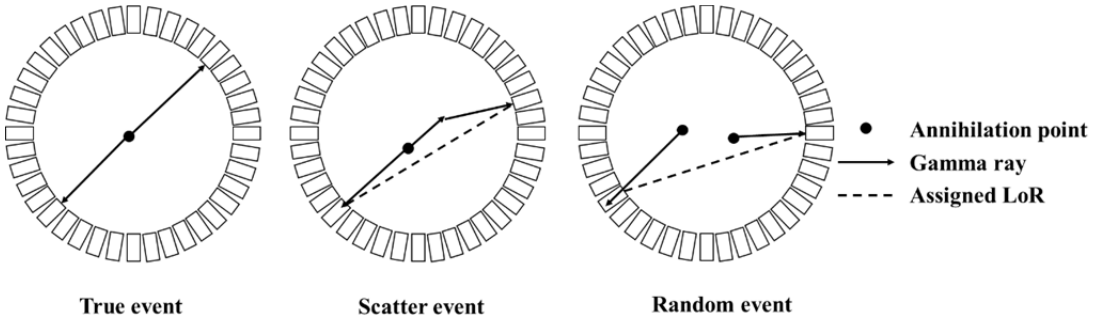

Figure 1-2, True, scatter and random coincidence events

In addition to the true coincidence events, there are another two types of events occurring in a PET system, both of which are not desired. The first one is a scatter event. When one photon scatters, it will change direction with energy loss, and the two photons detected are no longer in their original opposite directions. The second one is a random or accidental event. In this case, two photons are resulted from unrelated annihilations. Since they are close to each other in time, they will be considered as a coincident event when collected by the detection circuits. As shown in Figure 1-2, both scatter and random events could create inaccurate LoRs, which will degrade both spatial resolution and contrast recovery of lesions to be detected [14].

It is noted that not every annihilation will yield a counted event. This is because both annihilation photons must strike the coincident detectors for an event to be counted. As a result, the signal count rate in PET is typically much higher than the true count rate. Therefore, noise equivalent count rate (NECR) is widely used to

evaluate and optimize the performance. It is a good indicator to represent the signal quality for a PET system [19].

$$NECR = \frac{T^2}{T + S + R} \tag{1-1}$$

where T, S and R represent the true, scatter and random coincidence count rates, respectively. According to the equation above, there exist two ways to improve the NECR: 1) by increasing the total counts following Poisson statistics; and 2) by minimizing scatter and random events.

1.1.2. Detector technologies for PET Imaging System

(a) Scintillation photon detectors

Nowadays, as shown in Figure 1-3 scintillation crystals combined with silicon-based photodetectors are used to convert 511 keV gamma rays into electrical signals. The scintillator crystal converts the energy deposited* by incident gamma rays during attenuation into visible light photons. Electrons from the valence band in the scintillator are excited into the conduction band (mobile electrons) and leave vacancies, or 'holes,' in the valence band. As an electron from the conduction band return to the valence band and combines with a hole, it releases it excess energy in the form of visible light photons[14], [28]. The ratio between the number of free electron-hole pairs and the deposited energy is defined as conversion efficiency. The visible photons are emitted isotropically within the scintillator and thus the reflective materials are needed to be wrapped around to guide the photons towards one open face where the detector is located [24], [29], [30].

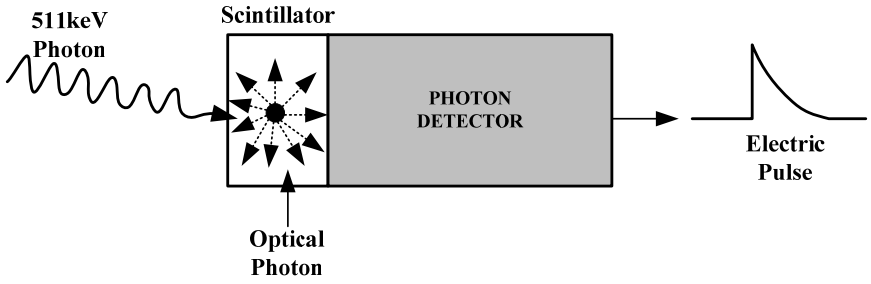

* The term "energy deposited" is commonly used in in nuclear medical science, which is equivalent to "energy absorbed" in electrical engineering

Figure 1-3, General design of a PET detector with scintillator crystal. The output current signal is then processed by the electronics of the system.

Ideal scintillator crystals need to exhibit high density and effective atomic number, high light output, and fast decay time [31]. A large mass number and effective atomic number will increase the stopping power of the crystal (i.e., linear attenuation coefficient μ) and therefore the detection efficiency [32]. In addition, a large atomic number will have a high proportion of photoelectric conversion relative to Compton interactions, thus improving energy resolution. The photoelectric absorption is the desired interaction for studies in this thesis because it is the most viable way of complete energy deposition. Also, the larger data size means less statistical noise which results in better energy resolution. Light output is defined as the number of scintillation photons per unit energy deposited, usually expressed as photons/MeV. High light output would reduce statistical uncertainty (noise) in the scintillation process and associated electronic signal, and improve energy resolution and scatter rejection [30][33]. For time measurement, a fast scintillator (i.e., a crystal with a short scintillation decay time) has a high rate of photon emission and leads to output pulses with fast rise time. The fast rise time allows the use of a narrow coincidence timing window to efficiently reduce random events. For energy measurement, a fast scintillation crystal of small decay time will have a shorter tail on its output signal, which is more likely to eliminate the pile-up effect, as well as to handle high counting rates [25].

NaI(Tl) crystals were the primary choice as a scintillator crystal in the PET scanners due to its high light output (~41,000 photons/MeV) [34]. However, it has a relatively low detection efficiency for 511 keV photons and its and poor timing resolution leads to high random coincidence events. Other candidates such as BGO, LSO and GSO have higher density and larger atomic numbers, and they have been recently used in PET systems [35]–[37].

After the creation of photons from the scintillation crystals, these visible photons are detected by photodetectors to produce electrical signals. These electrical signals need to be amplified because of the low light level from the scintillation process.

Commonly used detector technologies in PET include PMT, avalanche photodiodes (APD), and silicon photomultipliers (SiPM) [38].

Generally speaking, the working principle of PMTs, APDs and SiPMs all rely on 1) the generation of current carriers via excitation by scintillation photons; and 2) signal multiplication under applied bias voltage. Carrier generation is generally confined within a carrier-scarce environment, so that the device outputs very little or no current in the absence of scintillation photons. For PMTs, the carrier-scarce environment is realized by the vacuum condition within the tube. For semiconductor-based APDs and SiPMs, the carrier scarcity is established through a depletion region within a reverse-biased P-N junction [39]–[43].

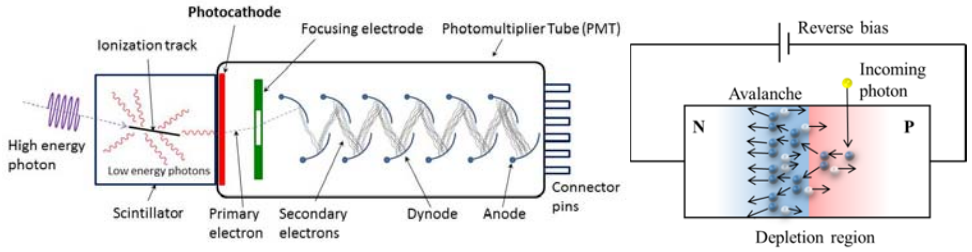

(a) (b)

Figure 1-4, (a) Schematic diagram of a typical PMT coupled to a scintillator (Reprinted from [44] with permission granted) . (b) Photocurrent is produced in APD operating in proportional mode (blue dots: electrons, white dots: holes).

Table 1-1, Three types of photodetectors used in PET systems[22]

	PMT	**APD**	**SiPM**
Gain	10^6	50-1000	10^6
Rise time (ns)	~1	~5	~1
QE@420nm(%)	25	70	25-75 (PDE)
Bias (V)	>1000	300-1000	30-80
Temperature Sensitivity (%/^{o}C)	<1	~3	1-8
Magnetic field sensitivity	Yes	No	No
Sensitive area	cm^2	mm^2	mm^2
Price/channel ($)	>200	~100	~50

A standard structure of a PMT is shown in Figure 1-4 (a), which essentially consists of a photocathode, a series of multiplication stages (dynodes) and an anode. Its conversion efficiency, also known as the quantum efficiency, is typically 1 to 3 photoelectrons per 10 visible light photons. When a high-speed photoelectron strikes the first dynode surface, it will eject several secondary electrons. The electron

multiplication factor of this stage depends on the energy of the photoelectron, which in turn is determined by the voltage difference between the dynode and the photocathode. Then, secondary electrons ejected from the first dynode are attracted to a second dynode, which is maintained at a 50-150V higher potential than the first dynode, and then such multiplication process is repeated at each subsequent dynode stages (typically 9 to 12 in total), before they are collected at the anode. A typical electron multiplication gain is in the range between 3 and 6 per dynode. Hence, the overall electron multiplication gain is up to 6^{10} for a 10-stage tube with an average multiplication factor of 6 at each dynode.

For APDs and SiPMs in Figure 1-4 (b), a depletion region exists due to the diffusion of electrons and holes, which becomes wider under the reversed bias condition. When incident photons are absorbed, electron-hole pairs will be generated mostly in the depletion region. These electron-hole pairs migrate towards electrodes under the external applied electric field and undergo impact ionization, which results in avalanche breakdown of the device, thus contributing to the formation of photocurrent. In each case, the amplitude of the resulting photocurrent can be several orders of magnitude greater than that without the avalanche process involved. However, due to their significantly long response time, APDs are not preferred for use in the PET application. In addition, their low multiplication gain usually results in weak output signals and thus requiring further amplification [45]. Table 1-1 summarizes the basic performance features of the three types of photodetectors [22].

(b) Semiconductor photon detectors

When semiconductor detectors are ionized by a radiation event, the electron-hole pairs are produced, and then collected by an external applied voltage, as shown in Figure 1-5. Semiconductor detectors are essentially solid-state analogs of gas-filled ionization chambers. Because the solid detector materials used in semiconductor detectors are about 2000 to 5000 times denser than gases, they yield much higher stopping power and detection efficiency.

Two commonly used semiconductor detector materials are silicon (Si) and germanium (Ge). Due to its low atomic number, silicon detectors are well-suited only for very low energy gamma rays and X-ray detection. The use of germanium

detectors at room-temperature is avoided due to thermally-induced leakage current caused by its small band gap energy [25]. Therefore, germanium detectors must be cooled to temperatures of around 77 K by coupling with liquid nitrogen or a mechanical cooler, which may take hours.

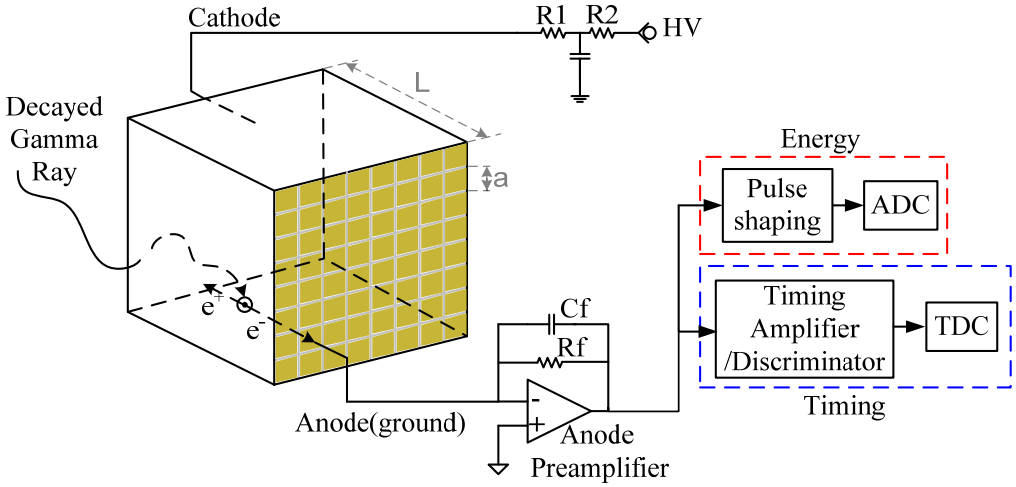

Figure 1-5, Operation and signal processing of pixelated semiconductor detector.

High purity germanium (HPGe) detectors have a slightly higher atomic number (32) and can be grown to relatively large sizes (750 cm^3) [25]. Compared to other detectors, it has a small band gap energy of 0.7 eV and only 3 eV is required to generate an electron-hole pair, allowing for excellent energy resolution due to the improved statistics of more information carriers for the same amount of gamma-ray energy deposited. Therefore, HPGe detector is a good choice for laboratory measurements that require excellent energy resolution, but less suitable for field measurements Alternative wide-band gap detector candidates are cadmium telluride (CdTe), CZT, mercury iodide (HgI_2), and thallium bromide (TlBr).

HgI_2 has been investigated as a room temperature X-ray and gamma ray detector since the early 1970s [46]–[48]. It has a higher effective atomic number than germanium, high density (6.4g/cm^3), high stopping power and a larger bandgap energy (2.13 eV). Therefore, the operation at room temperature is feasible because it suffers less from thermally generated leakage current compared to HPGe. Unfortunately, poor charge mobility (~10^{-5} cm^2/V for holes and ~$10^{-4}cm^2$/V for electrons), material non-uniformity and crystal polarization limit the use of HgI_2 in

planar detector geometries [49]. Better performance has been achieved using a pixelated anode configuration [50]–[52], but growth of HgI_2 continues to be plagued by defects and poor charge collection [53].

TlBr has recently gained interest as another possible room temperature semiconductor detector. With a large atomic number and density, TlBr is an efficient gamma-ray detector. The performance for TlBr (5 mm thickness) is reported to achieve 1% energy resolution at 662 keV [54]. Detectors up to 18 mm thick have been developed but their performance is degraded [55][55]–[57].

1.1.3. PET System Performance

1.1.3.1. Energy Resolution

Following the Beer-Lambert's Law, once annihilation photons are emitted, there is a finite probability of Compton scattering of soft tissue electrons before they leave the scan subject. When this happens, the LoR is no longer collinear from the point of photon emission, thus leading to an incorrect estimation of the radiotracer location. This photon scatter in tissue degrades PET imaging accuracy according to the definition of NECR in section 1.1.1. Because the annihilation photons will lose energy in Compton scattering, an energy measurement of less than 511 keV would indicate a photon has scattered, and should be discarded from the data set. This technique is called energy gating, and requires detectors to measure the energy of the detected photon with relatively high precision.

The performance of a radiation detection system is commonly characterized using a specific distribution called response function [25]. In reality, the peak is mathematically described by a Gaussian distribution instead of a delta function as illustrated in Figure 1-6. The width of photopeak is always broader due to the statistical errors, i.e. a large amount of fluctuation from pulse to pulse even though the same energy was deposited in the detector for each event. Thus, the width of the full energy peak reflects the system's energy resolution and its capability to separate two adjacent photon peaks of similar energies. If the amount of these fluctuations is smaller, the width of the corresponding distribution will also become smaller and the peak will approach a sharper spike or eventually a mathematical delta function.

There are a number of potential sources of fluctuation in the response of a given detector, which would result in imperfect energy resolution. These include 1) the operating characteristics of the detector drifting during the measurements; 2) random noise within the detector and instrumentation system, and 3) statistical noise of the measured signal itself. The dominant source of fluctuation is the statistical noise, because it represents an irreducible minimum amount of fluctuation that will always be present in the system, no matter how perfect the remaining components are made. And thus it sets an important limit on the detector's performance.

It is noted that there exists a continuous region (Compton continuum in Figure 1-6) locating at the left side (i.e. lower energies) of the full energy peak in the real energy spectra. This is due to the incomplete deposition of energy by incident radiation, such as energy lost in Compton scattering of 511 keV photons. The curves labeled "Good resolution" and "Poor resolution" illustrate the response of a detector with superior and inferior performance, respectively. When the same number of pulses is recorded in both cases, the areas under each peak are equal. Although both distributions are centered at the same value E_0, the width of the distribution in the poor resolution case is much greater.

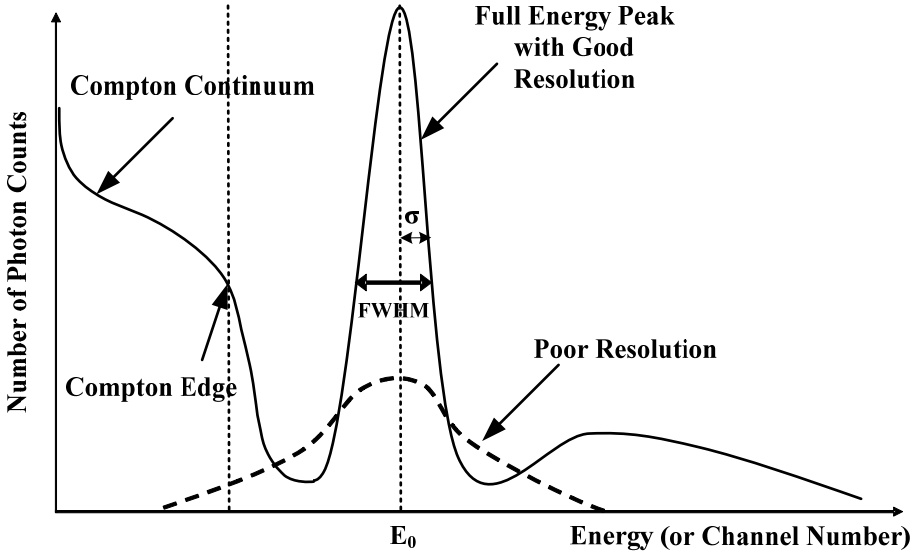

Figure 1-6, Examples of energy spectrum. Good energy resolution (solid line) and poor energy resolution (dashed line) are provided for comparison.

A frequently-used energy resolution metric is the Full-Width at Half-Maximum (FWHM in percent) as defined by equation [25]:

$$\text{Energy Resolution } = \frac{\Delta E}{E_0} \times 100\% \tag{1-2}$$

where ΔE denotes the FWHM width of the full energy peak in measurement, and E_0 is peak center (or the photon energy being measured). Under the assumption that the formation of each charge carrier is a Poisson process, if a total number N of charge carriers is generated on average, the inherent statistical fluctuations expected is the standard deviation $\sqrt{N}$. Typically N is a large number. Besides, other physical factors affecting the energy resolution such as non-linearity of light emission in scintillator materials and photodetectors, the statistical fluctuation can be modelled as a response function of Gaussian-shape:

$$G(E) = \frac{A}{\sigma\sqrt{2\pi}} e^{-\frac{(E-E_0)^2}{2\sigma^2}} \tag{1-3}$$

$$\text{FWHM } = 2\sqrt{2\ln 2}\sigma \approx 2.355\sigma \tag{1-4}$$

where σ is the standard deviation.

The response of many detectors is approximately linear, so that the average amplitude of pulse is $E_0=KN$, where K is a proportionality constant. Then, the standard deviation σ of the peak in the pulse height spectrum is $\sigma=K\sqrt{N}$ and its FWHM is $2.355K\sqrt{N}$. Therefore, we can calculate the energy resolution as [25],

$$\text{Energy Resolution}_{\text{Poisson Limit}} = \frac{2.355K\sqrt{N}}{KN} = \frac{2.355}{\sqrt{N}} \tag{1-5}$$

This equation implies that the energy resolution is fundamentally limited by the number of charge carriers N to be detected, and the resolution improves as N increases. Therefore, in order to achieve an energy resolution better than 1%, one must have N greater than 55,000. An ideal detector would have as many charge carriers generated per event as possible, so that this limiting resolution would be a percentage as small as possible. However, using semiconductor detectors, experiments have achieved energy resolution at least an order of magnitude better than predicted by Poisson statistics given in equation (1-5) above [58]. These results would indicate that the processes that give rise to the formation of each individual charge carrier are not independent, and therefore the total number of charge carriers

cannot be described by a simple Poisson statistics fluctuation. In statistics, the Fano factor F has been introduced to quantify the departure of the observed statistical fluctuations from pure Poisson statistics, and it is defined as

$$F = \frac{\text{observed variation in N}}{\text{Poisson predicted variance(=N)}} = \frac{\mu}{\sigma^2} \tag{1-6}$$

Therefore, the energy resolution of semiconductor detectors can be calculated by equation (1-7). Compared with equation (1-5), the energy resolution is now scaled by a factor of $\sqrt{F}$.

$$\text{Energy Resolution}_{\text{Statistical Limit}} = \frac{2.355K\sqrt{N}\sqrt{F}}{KN} = 2.355\sqrt{\frac{F}{N}} \tag{1-7}$$

The scintillator detectors show a limiting resolution consistent with Poisson statistics and their Fano factor would be unity. For CZT, the Fano factor has been measured to be 0.089±0.005 [59], which means its intrinsic energy resolution is approximately an order of magnitude better than scintillator detectors.

Besides the inherent statistical fluctuations, the overall energy resolution of system is reduced by other factors, such as noise from detector electronics, and operating conditions during measurements such as detector stability. If they are systematic and independent, the overall response function will always tend toward a Gaussian shape according to statistical theory, even if the individual sources are characterized by distributions of different shapes. As a result, we can obtain the overall FWHM of system in equation (1-8)

$$\left(FWHM\right)^2_{overall} = \left(FWHM\right)^2_{statistical} + \left(FWHM\right)^2_{noise} + \left(FWHM\right)^2_{drift} + \cdots \tag{1-8}$$

1.1.3.2. Spatial Resolution

The ability to distinguish two adjacent small points in space in an image is referred as the spatial resolution. For a PET system, this is determined by both the underlying physics as well as instrumentation choice. As shown in (1-9), a semi-empirical framework has been developed to predict the spatial resolution of a PET system based on measurements [24].

$$R_{system} \approx \sqrt{R^2_{det} + R^2_{range} + R^2_{180^o}} \tag{1-9}$$

The overall spatial resolution associated with detector response R_{det}, positron range R_{range}, as well as annihilation photon non-collinearity R_{180^o}. Normally, image blurring due to physics-level effects cannot be easily mitigated.

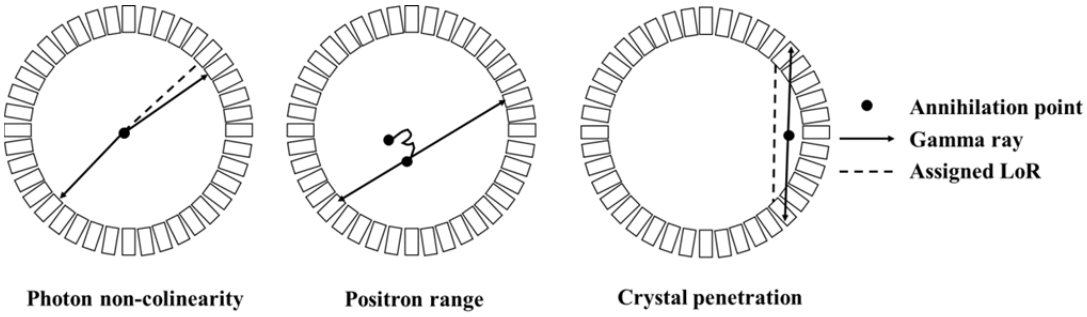

Figure 1-7, Illustration of three factors for PET (scintillator-based) spatial resolution distortion: photon non-collinearity, positron range and crystal penetration.

Positron range originates from the physics of positron-electron annihilations. When a positron is created, it carries certain amount of kinetic energy and travels a short distance before its annihilation with an electron. Positron range is a function of the initial kinetic energy of the emitted positron and the surrounding medium [24]. Since positrons act as a proxy of the radiotracer that emitted them, large positron ranges lead to larger non-collinearity between the LoR and the true location of the radiotracer molecules, which would introduce blurring in PET images. For some isotopes, this can be the dominant limitation in the final image resolution [23].

In reality, a positron or electron would still carry some residual momentum when it reaches the end of its range. Therefore, when a positron annihilates with an electron, a pair of high-energy photons at almost 180-degree or in anti-parallel direction, is created. The effect of this non-collinearity on the spatial resolution is proportional to the diameter of the field-of-view (FoV). This is not expected to be a major source of spatial resolution degradation in the systems with a FoV under ~100 mm, such as small animal or breast cancer imaging systems.

Aside from physical effects, there are numerous instrumentation variables that determine PET spatial resolution. Ideally, we have assumed LoRs to be infinitely thin lines. In reality, the annihilation events are limited to a LoR enclosed somewhere within a tube of response, whose width and shape is defined by the size and shape of

the individual detector elements, which has finite size. Intuitively, the smaller the detector elements, the thinner the tubes of response, and the higher the image resolution we can obtain. Consequently, the detector element size is a dominant determinant in the spatial resolution of a system's reconstructed image. In scintillator crystal photon detectors, the detector element size is set by the physical size of the crystal elements. In semiconductor photon detectors, this is determined by the pixelation discretization of the electrode pattern.

1.1.3.3. Coincidence Time Resolution

The timing precision of a PET imaging system represents the time difference between detected annihilation photons, and it is also referred as coincidence time resolution. Unlike energy resolution, coincidence time resolution is characterized only by the FWHM of a Gaussian distribution fitted to the time spectrum. The centroid of the function is not as important as the accuracy of the measurement.

For a PET scanner based on scintillator and photodetectors, several physical factors limit the time resolution. Here we assume that the time fluctuation due to the photodetector's response and electronics is identical for all detectors. Then, the overall time resolution can be described by [45]:

$$\Delta t_{overall} = \Delta t_{flight} + \Delta t_{DoI} + \Delta t_{OTT} + \Delta t_{CTT}, \tag{1-10}$$

where t_{flight} is the flight time of 511 keV annihilation photons from annihilation site to the front surface of the detector, t_{DoI} is the combination of two processes: 1) propagation time of annihilation photons from the front surface of detector to the interaction sites; and 2) subsequent flight time of the generated scintillation photons (unscattered) within the crystal to the location of photodetector. t_{OTT} is the optical transit time of scintillation photons experiencing significant scattering within crystals, and t_{CTT} is the transit time of photoelectrons before they are detected. Therefore, Δt_{DoI} and Δt_{OTT} terms are inherent time resolution from scintillation crystals. Δt_{CTT} is determined by the property of detectors.

During the measurement, we can derive overall time resolution by the following steps: 1) calculating the time difference measured between the two photon interactions in each pair of true coincidence event (see Figure 1-2), 2) plotting a histogram of all time difference values calculated for a large ensemble of photon pairs,

and 3) finding the FWHM of the histogram distribution peak. Here, the identification of true coincidences can be implemented by specifying a time window combined with an energy gating approach. After rejection of scatter events located outside of the energy window, any pair of photons detected within the duration of the time window would be considered as a true coincidence event. This identifying method is called time gating. In practice, a time window is normally set to twice the time resolution to reject those random (also known as accidental) annihilation photons.

1.2. X-Ray Imaging

X-ray imaging is one of the most commonly used imaging modalities in clinical diagnosis. Besides medical application, X-ray imaging is also widely used in many other industrial applications, such as soil core analysis, nondestructive testing and material characterization [15].

1.2.1. Principles of Medical X-ray Imaging

As the part of the electromagnetic spectrum, X-rays span the spectrum from approximately 100 eV and higher (wavelengths below 10 nm). The illustration of image acquisition is shown in Figure 1-8. The probability of interaction of X-rays with materials at certain energy is linked with the material's attenuation coefficient μ. The transmitted (non-scattered and non-absorbed) X-rays are detected in the detector array. High-density materials block more X-ray interactions and suffer from more radiation dose at the same time.

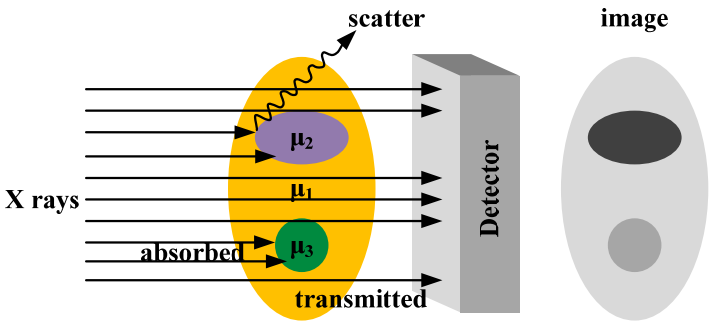

Figure 1-8, Basic principles of X-ray imaging. Incident X-rays will interact differently with an object composed of different materials (heterogeneous). The resulting image is the shadow cast by the object being illuminated by X-rays ($\mu_1>\mu_2>\mu_3$).

As illustrated above, the general principle of X-ray imaging is based on the attenuation of an X-ray beam of intensity I_0 by the object and the transmitted intensity I. This intensity reduction as a function of the attenuation coefficient μ of the absorber is described by the Beer-Lambert's law [60]. When the monochromatic rays penetrate through a homogeneous object of thickness x as shown in Figure 1-9, the attenuation can be described as follows:

$$I = I_0 \cdot e^{-\mu x} \tag{1-11}$$

In practice, organs in human body are not only inhomogeneous tissues, but also the thicknesses of tissues are different, as illustrated in Figure 1-9 [61]. Therefore, the Beer-Lambert Law needs to be modified to:

$$I = I_0 \cdot e^{-(\mu_1 x_1 + \mu_2 x_2 + \mu_3 x_3 + \cdots + \mu_n x_n)} \tag{1-12}$$

$$I = I_0 \cdot e^{-\int \mu(x) dx} \tag{1-13}$$

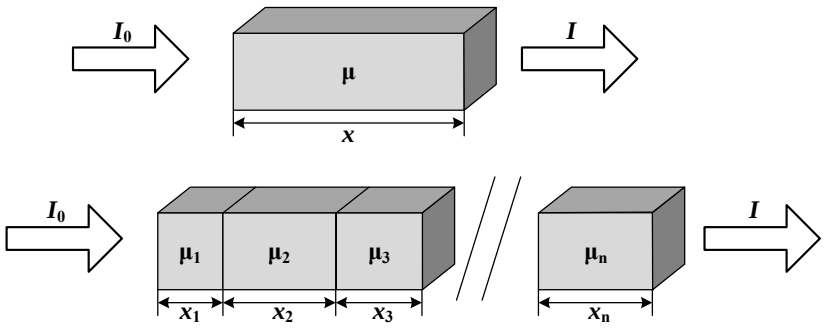

Figure 1-9, Top: attenuation of X-ray with one monochromatic block; Bottom: attenuation of X-ray with a series of monochromatic blocks.

X-rays used for clinical imaging are generated by an X-ray tube, typically a tungsten rotating anode tube. High energy electrons strike a target and lose energy as they interact with the atoms in the target. These interactions cause the electrons to slow down and the electrons radiate energy in the form of bremsstrahlung (braking radiation) X-rays. The X-ray profile has a continuous range of energies (polychromatic radiation) and is often characterized by the maximum or peak kilo-voltage (kVp).

Due to the aforementioned X-ray production process, the measured attenuation coefficient for a CT system depends strongly on the energy spectrum. To allow for

both quantification and comparison, Hounsfield units (HU) has been introduced [62][63]:

$$HU = 1000 \frac{\mu_t - \mu_{water}}{\mu_{water}} \tag{1-14}$$

where μ_t is the reconstructed effective linear attenuation coefficient of the object, and μ_{water} is the effective linear attenuation coefficient of water.

1.2.2. Detectors for X-ray Imaging System

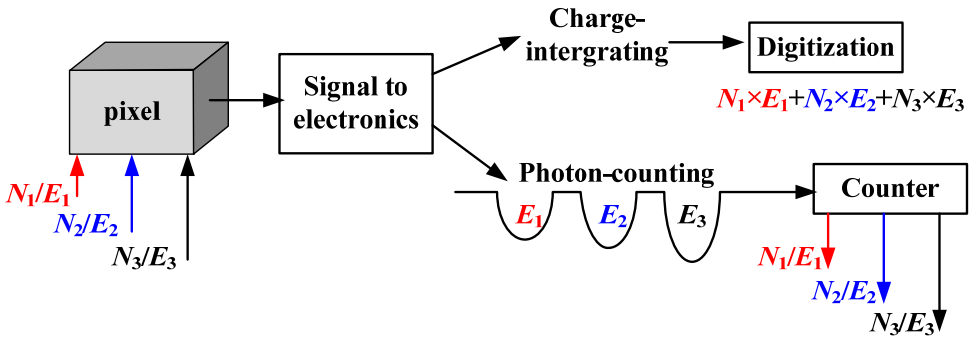

Figure 1-10, Energy integrating detectors record the total charge for all interactions. Photon counting detectors resolve individual interactions.

The first-generation detector used for X-ray imaging was photographic plates, which were later replaced by films. Recently, CT used digital detectors and software to reconstruct 3D images with software. Although the spatial resolution of a digital system is generally inferior to that of the films due to the finite pixel's size, there are several advantages offered by digital imaging [15]. Two main types of digital X-ray imaging are "charge-integrating" (or "energy-integrating") and "photon counting" (or "energy-resolving") [64]. The detection processes for each type are shown in Figure 1-10.

Conventional CT detection operates in the charge-integrating mode, where the signal is proportional to the amount of energy deposited in the detector over a finite period of time. This type of detectors is insensitive to the spectral information contained in the attenuated beam, and the attenuation coefficient obtained is the average result of whole spectrum [63]. In this way, those photons of higher energy are more likely to reach the detectors than photons of lower energies. However, the differences in attenuation coefficient at low energies contribute more to the image

contrast. To address this limitation, detectors that count individual photons in X-ray imaging were recently studied. Charge generated by each photon in a detector pixel is processed by the readout electronics. The transmitted X-ray spectrum can be now divided into a number of different energy bins by using pulse-height discrimination [65]–[67]. For the special case with only two energy windows, photon-counting detectors can be used for dual-energy CT imaging. Photon counting detectors have the capability to resolve photon energy and make the use of a technique known as "energy-weighting". This technique applies weighting factors to different energy bins in order to optimize the image's SNR [68]. A number of studies have already shown that energy-weighting can either improve image SNR/contrast, or be used to reduce the radiation dose levels when compared to conventional CT imaging [16], [66], [69]. Furthermore, photon-counting detectors such as CZT detectors can have a higher geometric efficiency by approximately 30% than energy-integrating detectors. In addition, good energy discrimination opens the possibility for K-edge imaging.

1.3. Motivations for the use of CZT Detectors

As mentioned in the previous sections, CZT detectors have several advantages for both PET and photon-counting CT imaging systems due to their physical properties that are summarized in Table 1-2.

Table 1-2, Physical properties of CZT

Material	**$Cd_{0.9}Zn_{0.1}Te$**
Atomic numbers (Z)	48, 30, 52 (ave.49.1)
Density (g/cm^3)	5.78
Mass attenuation coefficient @511keV (cm^{-1})	8.63×10^{-2}
Band gap E_g (eV)	1.572
Pair creation energy (eV)	4.64
Relative dielectric constant (ϵ)	10.9
Resistively (Ωcm)	3×10^{10}
Electron mobility μ_e (cm^2/Vs)	1000
Electron lifetime τ_e (s)	3×10^{-6}
Hole mobility μ_h (cm^2/Vs)	50-80
Hole lifetime τ_h (s)	2×10^{-6}
Price/crystal (*64 channel pixelated*)	~$500

CZT is able to achieve high quantum efficiency in the typical range between 10 and 500 keV. The relatively high atomic number results in a dominant photoelectric

absorption probability against Compton scattering interaction, up to 300 keV. High material density results in good stopping power. Furthermore, its wide band-gap (a bandgap energy about 1.6 keV) leads to very high resistivity and allows for operation at room temperature [70], [71].

Compared to scintillator-based detectors, the direct conversion CZT enables it to achieve superior energy resolution and good spatial resolution. For example, pixelated CZT can achieve ~1%-3% FWHM at 662 keV and ~2-4% FWHM at 511keV. On comparison, HPGe can achieve superior energy resolution, but it requires cooling and low-noise electronics. For other room temperature semiconductors such as HgI_2 or TlBr, neither of these materials could be easily made with the same physical volume to achieve comparable performances to CZT detectors [25].

In spite of unique advantages of CZT mentioned above, several limitations remain. These include hole trapping, charge sharing and count rate limitations. Poor hole transport of CZT materials is a critical issue in the development of X-ray and gamma ray detectors. For example, the trapping of holes will reduce charge collection efficiency, produce an asymmetric long tail to the left of the photopeak in the measured energy spectra and degrade energy resolution.

There are two major techniques to minimize this hole trapping effect. The first technique is detector orientation with respect to the incoming 511 keV gamma rays. For example, the planar parallel field (PPF) is a common configuration used in planar detectors. In this configuration, the detectors are irradiated through the cathode, thus minimizing the probability of hole trapping. In one alternative configuration, denoted as planar transverse field (PTF) [72], the irradiation direction is orthogonal (transverse) to the electric field and the main benefit is to enhance detection efficiency. The second technique is single polarity sensing. In this sensing, the detectors only acquire the induced signals by electrons, which have better electrical transport properties than holes. This technique can be implemented by using 1) either electronic methods including pulse rise time discrimination [73], bi-parametric analysis [74][75]; or 2) advanced electrode design such as Frisch-grid [76], [77], pixels [78], [79], coplanar grids [80], strips [81], [82] or multiple electrodes [83]–[86]. (See section 2.2.2).

Charge sharing is another limitation to be addressed, as it degrades both energy resolution and spatial resolution. Charge sharing in CZT detectors is largely linked to the two physical processes: characteristic X-ray escape and charge diffusion. Characteristic X-ray escape can be studied through simulation tools to correct for any distortion in the energy spectra. Charge diffusion can potentially be reduced by using coincidence circuits between neighboring pixels. The limit of count-rate also needs to be addressed through the use of improved CZT detectors with lower hole trapping and faster readout [1], [87].

1.4. Research Contributions

The research described in this thesis is aimed at investigating CZT detectors to achieve better performance of specific medical imaging systems that include PET and photon-counting CT. The major contributions of this work are summarized as follows.

- A comprehensive procedure based on Monte Carlo simulation and Shockley-Ramo theory was developed. It systematically modeled the photon interaction, charge generation, transportation and collection processes within CZT detectors. Small pixel effect, DoI effect, hole trapping effect, single polarity sensing and depth sensing were studied as the function of design parameters, including electrode geometry, bias voltage and detector SNR.
- A prototype of PET system was built based on the planar parallel field (PPF) configuration of CZT detector. The depth calibrations using cathode-to-anode ratio and electron drift time were applied to preliminary measured results. Using a ^{22}Na source, measurements of the performance of the prototype demonstrated promising energy resolution and coincidence time resolution.
- For the first time, the valid range of charge sharing effect was defined and calculated quantitatively. It was successfully used to more accurately calculate charge loss induced by charge sharing effect, which helped in evaluating the deterioration in the system's performance.
- Based on the investigations of charge sharing effect and transient signal analysis, a novel algorithm was proposed to improve spatial resolution using CZT detectors: A sub-pitch spatial resolution of ~250 μm was obtained for a SNR of ~17.

- In photon counting CT application, the impact of CZT detectors on energy performance was studied. We systematically investigated intrinc charge loss, charge sharing, and characteristic X-ray escaping with different incident beam locations and pixel configurations. These results can help us: 1) to optimize the design parameters and operation conditions of CZT detectors for photon counting CT application; and 2) to identify the relationship between the performances of CZT detectors (i.e., count loss and energy spectral) and quantitative derivation of HU from CT images.

Below, a list of the journal papers and conference presentations during the period of work conducted in this thesis is given.

Journal Papers

1. X. Zheng, Z. Cheng, M. J. Deen and H. Peng, "Effect of Charge Sharing and Characteristic X-ray Emission in CZT Detectors for Photon-Counting Computed Applications," *IEEE Transactions on Nuclear Science*, In Press, 9 journal pages (Accepted 4 September 2017).
2. X. Zheng, Z. Cheng, M. J. Deen and H. Peng, "Improving spatial resolution in CZT detector using charge sharing and transient signal analysis: simulation study," *Nuclear Instruments and Methods in Physics Research Section A: Accelerators, Spectrometers, Detectors and Associated Equipment*, vol. 808, pp. 60-70, Feb 2016.
3. X. Zheng, M. J. Deen and H. Peng, "Performance Characteristics of CZT Detectors for PET Imaging Applications", *The Electrochemical Society Transactions*, vol. 61, issue 35, pp. 7-13, May 2014.
4. Z. Cheng, X. Zheng, D. Palubiak, M. J. Deen and H. Peng, "A comprehensive and accurate analytical SPAD model for circuit simulation," *IEEE Transactions on Electron Devices*, vol. 63, no. 5, pp 1940-1948, 2016.
5. Z. Cheng, X. Zheng, M. J. Deen and H. Peng, "Recent Developments and Design Challenges of High-Performance Ring Oscillator CMOS Time-to-Digital Converters," *IEEE Transactions on Electron Devices*, vol. 63, no. 1, pp. 235-251, 2016

6. Z. Cheng, D. Palubiak, X. Zheng, M. J. Deen and H. Peng, "Impact of silicide layer on single photon avalanche diodes in a 130nm CMOS process," *Journal of Physics D: Applied Physics*, vol. 49, no. 34, pp. 345105-345114, 2016.

Conference Presentations

1. X. Zheng, Z. Cheng, M. J. Deen, H. Peng and L. Xing, "Impact of charge sharing effect on sub-pitch resolution for CZT-based photon counting CT systems," oral presentation in *American Association of Physicists in Medicine (AAPM) Annual Meeting*, Washington, DC, July 31- Aug.4, 2016.
2. X. Zheng, Z. Cheng, M. J. Deen and H. Peng, "Sub-pitch spatial resolution in CZT detectors: simulation study," oral presentation in *IEEE Nuclear Science Symposium & Medical Imaging Conference(NSS/MIC)*, San Diego, CA, Dec. 31-Nov.7, 2015.
3. X. Zheng, Z. Cheng, M. J. Deen and H. Peng, "Investigation of the sub-pixel spatial resolution and charge-sharing effect in CZT detectors for PET imaging," poster presentation in *Society of Nuclear Medicine and Molecular Imaging Annual Meeting (SNMMI)*, Baltimore, MD, Jun. 6-10, 2015.
4. Z. Cheng, X. Zheng, M. J. Deen, H. Peng, and L. Xing, "Noise modeling of SPAD for photon counting CT applications," oral presentation in *American Association of Physicists in Medicine (AAPM) Annual Meeting*, Washington, July 31- Aug.4 , 2016.
5. Z. Cheng, X. Zheng, M. J. Deen and H. Peng, "Development of a Time-to-Digital Converter and 8×8 Single Photon Avalanche Photodiode Array Towards the Digital SiPM Sensor," poster presentation in *IEEE Nuclear Science Symposium & Medical Imaging Conference (NSS/MIC)*, San Diego, CA, Dec. 31-Nov.7, 2015.
6. Z. Cheng, X. Zheng, M. J. Deen and H. Peng, "Development of a High Performance Digital Silicon Photomultiplier (dSiPM) for ToF PET Imaging," oral presentation in *Society of Nuclear Medicine and Molecular Imaging (SNMMI) Annual Meeting*, Baltimore, MD, Jun. 6-10, 2015.

1.5. Thesis Organization

This thesis is organized as follows. In chapter 1, a brief overview of PET and X-ray imaging systems are given. The physical principle, detector developments and system performance are provided. Then, the CZT detector is presented along with an explanation of why it is potentially superior to conventional detectors. The motivation of CZT characterization for these applications is discussed. Finally, a brief summary of the main contributions of this research and the structure of this thesis are given.

In chapter 2, an overview of various annihilation photon detection schemes, focusing in particular on CZT's material characteristics underpinning the many imaging advantages and limitations, is presented. Detailed modeling on the photon interaction, charge induction, transportation and collecting process is given. Their impacts on the collected signal, including hole trapping, DoI effect and small pixel effect are considered. Then, the pre-processing (hardware) and post-processing (software) of collected signal from radiation detector are introduced.

In chapter 3, a series of experiments to demonstrate and improve the imaging abilities of CZT detectors for PET application is described. Different algorithms are implemented to calibrate the non-ideal systematic factors, including the nonlinearity, the non-uniformity and depth dependency. Then, the system's energy resolution and coincidence time resolution are evaluated with PPF configuration.

Next, in chapter 4, a novel algorithm to achieve sub-pitch spatial resolution of the CZT-based PET system, instead of downsizing the anode pixel of detector is proposed and implemented. The algorithm is based on charge sharing effect and transient signal analysis. Then, the valid range of charge sharing is defined, quantitatively calculated and used. Also, the dependence of achievable sub-pitch spatial resolution on design parameters, including electrode geometry, photon interaction location, bias voltage and detector SNR, is investigated.

In chapter 5, the investigation of the feasibility of CZT photon counting detector in photon-counting CT application is described. The intrinsic charge loss, characteristic X-ray emission and charge sharing effect are considered to evaluate the effect of the detector on the system's performance. Several figures-of-merit effective

count rate, energy conversion factor, as well as energy spectra are defined, modeled and compared.

In chapter 6, a summary of the research with highlights the main research outcomes of CZT-based medical imaging systems is given. Finally, the potential for future improvements of CZT-based images is discussed.

Chapter 2

MODELING OF CZT-BASED DETECTOR'S PERFORMANCE[†]

In this chapter, the physical and electrical properties of CZT material will be introduced and investigated by comprehensive and accurate analytical modeling, which is important to understand how they will affect the performances of PET and photon-counting CT.

2.1. Photon Interactions in CZT Detectors

2.1.1. Interaction Mechanisms

Within CZT material, there are different types of photon interaction mechanisms. The dominant types of photon interaction of interest depend on the energy range of incident photons. At low energies, photoelectric absorption is dominant. At energies starting near 300 keV, Compton scattering is most likely. Pair production (electron-positron pair) is possible starting at 1.022 MeV. However, it dominates above 5 MeV. For example, in the energy range applicable for PET (i.e., at or below 511 keV), we focus on photoelectric absorption and Compton scattering interactions. Diagnostic X-ray imaging typically uses X-rays within the energy range of 20 to 120 keV, and three types of interactions may occur at these energies: photoelectric absorption, Compton

[†] Part of this work was published as: X. Zheng, M. J. Deen and H. Peng, "Performance Characteristics of CZT Detectors for PET Imaging Applications", The Electrochemical Society Transactions, vol. 61, issue 35, pp. 7-13, May 2014.

scattering, and Rayleigh scattering. The photon cross-section of CZT between 10keV and 10MeV is shown in Figure 2-1. The total cross-section (i.e. detection efficiency) rises with decreasing photon energy. The steps in the photoelectric cross-section are the K, L_1, L_2 and L_3 edges of the constituent elements [88].

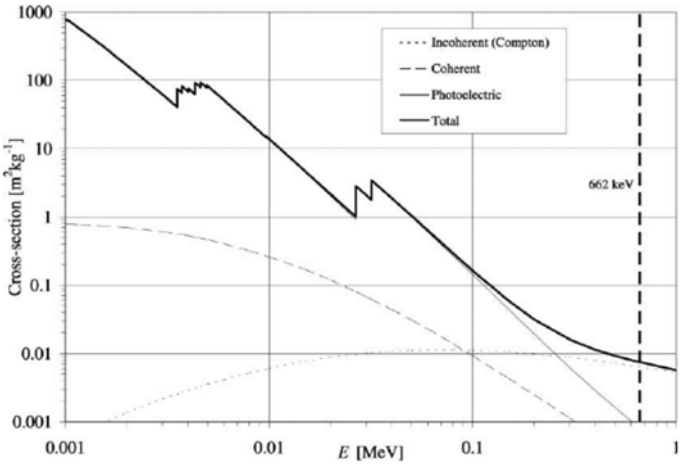

Figure 2-1, Interaction cross-section data for $Cd_{0.9}Zn_{0.1}Te$ detector material. (Reprinted from [88] with permission granted)

2.1.1.1. Photoelectric Absorption

It is noted that the measurements of photon energy are most accurate when they deposit all of their energy in a detector. Photoelectric absorption is the desired interaction for the detectors studied in this thesis because it is the only possible way of complete energy deposition.

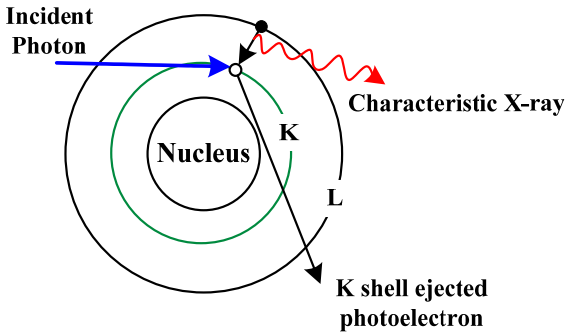

Figure 2-2, Schematic representation of photoelectric absorption.

Figure 2-2 shows the photoelectric absorption. It occurs when an incident photon interacts with an electron that is bound in an atom. About 80% of these interactions take place with electrons in the K-shell [89]. Following the absorption, an electron, i.e.

photoelectron, is ejected from the atom. The photoelectron's energy is equal to the difference between the initial photon energy (E_0) and the binding energy of the electron (E_b).

$$E_{photoelectron} = E_0 - E_b \tag{2-1}$$

The vacancy left by the photoelectron is quickly filled by a captured electron or an electron from a higher energy electron shell. Then, the binding energy is released in the form of a characteristic X-ray or Auger electron, both of which are typically reabsorbed in the near-by pixel. For low incident photon energies, the emission direction of the photoelectron is most likely normal to the incident/traveling direction of the photon. At high energies, the photoelectron is more likely to be released in the direction that the incident photon was traveling.

2.1.1.2. Compton Scattering

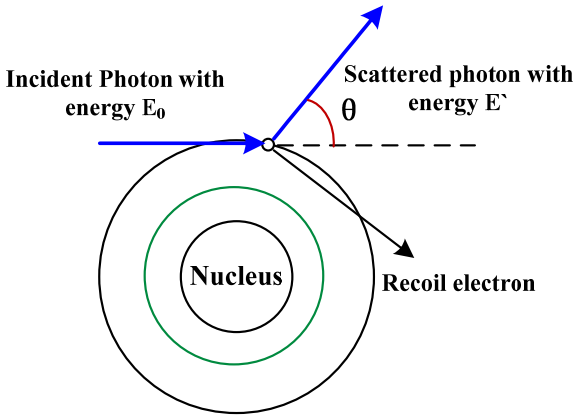

Figure 2-3, Schematic representation of Compton Scattering.

Unlike the photoelectric effect, Compton scattering would not eliminate the original incident photon. In a Compton scattering event shown in Figure 2-3, the incident photon collides with an outer shell electron, transfers part of its energy to a recoil electron and is scattered at angle θ with respect to its initial direction ($\theta \in (0, 180^o]$). The angular distribution of scattered photons is given by the Klein-Nishina formula, and it indicates a tendency for forward scattering in energies relevant to PET [25].

Assuming the initial electron is free and at rest, according to the conservation laws of energy and momentum, the relationship between the scattered photon energy *E'* and scattering angle θ can be derived as Compton's formula,

$$E' = \frac{E_0}{1 + \left(E_0 / m_e c^2\right)\left(1 - \cos\theta\right)} \tag{2-2}$$

$$E_{eCompton} = E_0 - E' \tag{2-3}$$

in which $m_e c^2$ is the rest mass energy of an electron (~0.511MeV). Equation (2-2) also reveals that the *E'* and θ are in one-to-one correspondence. The larger the scattering angle, the less is the energy of scattered photon. The highest energy of scattered photon, corresponding to full backscatter ($\theta = 180^o$), is called the Compton edge. For example, if an annihilation gamma-ray photon (E_0= 511 keV) is backscattered, the energy of recoil electron would have an additional $E_{eCompton}$ = 340.706 keV.

Therefore, if the incident photon energy is known, the scattering angle θ can be determined uniquely based on the energy loss in the first scattering. If the scattered photon interacts with the detector by photoelectric absorption or another Compton scattering event, then the positions of the two interactions can give the direction of the scattered photon.

2.1.1.3. Pair Production and Rayleigh scattering

Pair production occurs when an incident photon interacts with the electric field of a nucleus to form an electron-positron pair. The rest mass of the electron-positron pair, 1.02 MeV, is required in the incident photon for pair production to occur, and any excess energy is carried off by the electron-positron pair [25]. For energy ranges applicable to PET or photon-counting CT applications in this thesis, it is not relevant.

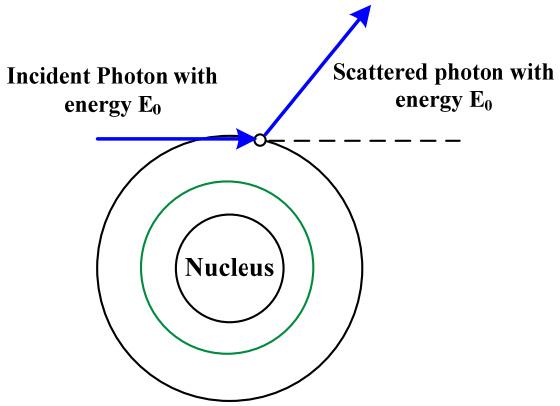

Figure 2-4, Schematic representation of Rayleigh scattering.

It should be pointed out that another photon interaction process, Rayleigh scattering, occurs at low energy levels (less than 50 keV) in those materials of high atomic number. In Rayleigh scattering, the incident photon interacts with the whole atom. The photon changes its direction without losing its energy (also known as "elastic scattering"), as shown in Figure 2-4. Therefore, if an incident photon scatters out of a pixel due to Rayleigh scattering and interacts with a neighboring pixel, the spatial resolution is affected, but not the energy resolution. This secondary interaction is often neglected in annihilation photons interaction for PET.

Together, the photoelectric effect and the Compton formula impart distinct features to the energy spectrum of photon interactions in a detector. An energy spectrum is a plot of the relative frequency of occurrence as a function of the energy deposited by photons. The example of energy spectrum is shown in Figure 1-6. It is noted that since all photoelectric interactions occur with equal energy, a spectral spike (photopeak) is found at E_0. With Compton scattering, the energy deposition is limited to between 0 keV (0^o deflection) and $2E_0/3$(180^o backscatter), which would give rise to a Compton edge. Similarly, a source emitting photons at n distinct E_0 values would result in n distinct photopeaks and Compton edges.

In a Compton scattering event, the incident photon may deposit some energy in one pixel, while the scattered photon can possibly interact in another pixel. Thus the spatial resolution is degraded. Compton scattering is very complicated to be simulated because of the range of energies and angles of the scattered photon. The photoelectric effect has the advantage of being the easiest interaction to simulate since the photon is

completely absorbed and does not interact multiple times. However, spatial and energy blurring would occur due to escape of characteristic X-rays emitted from photoelectric effect. Fortunately, these X-rays have discrete energies and are emitted isotropically from the atom. Therefore their behavior is relatively easy to predict (see chapter 5).

2.1.2. Monte Carlo Simulation

The Monte Carlo method is usually used for optimization, numerical integration, and particle probability distribution, and it has become an essential tool for use in nuclear medical imaging. Geant4 Application for Tomographic Emission (GATE) is one of the Monte Carlo simulation packages for PET/SPECT (Single-photon emission computed tomography) [90]. The simulation was performed to quantify the characteristic patterns of photon interactions of interest. For each interaction, the spatial coordinates (x, y and z), time, deposited energy and type of effect are saved in list-mode.

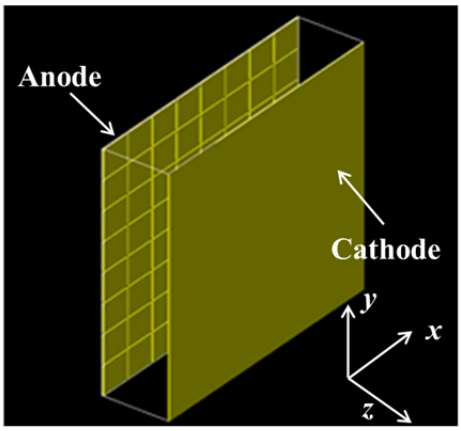

Figure 2-5, An example of the simulated geometry with L=5mm. This is consistent with real detector used in our research.

The simulated geometry is shown in Figure 2-5. A CZT detector of dimensions $20\times20\times L$ mm^3 (density=5.78 g/cm^3) was selected, where the variable L is the thickness of detector. A collimated beam (10μm diameter) and from a distance of 1000mm was configured to hit the center (x=0, y=0) of the cathode side. Then, 20,000 events (no energy threshold) are recorded. The results would give us the primary probabilities and sensitive range of each type interaction in space. If a photon is only

subject to a single Compton scattering interaction, it is classified as a 'CS' event. If a photon is only subject to a single photoelectric absorption, then it is classified as a 'PE' event. All other events that involve multiple interactions (including multiple Compton scattering, Compton scattering followed by photoelectric absorption and events involving Rayleigh scattering) are classified as 'M' events. The ratio of single interaction events (PE+CS) to multiple interaction events (M) is calculated because the majority of the resolution degradation was shown to come from the 'M' events [91].

An electron produced by a single interaction causes ionization (secondary electrons) along its trajectory and gradually slows down to deposit its energy until it reaches an endpoint (x and y). Then, the events can be processed into a 2D histogram. These histograms provide a visual representation of the spread of energy centroid away from the initial photon direction (defined by x=0, y=0) through the material. This spread leads to a degradation of the spatial resolution by introducing an error in the determination of the location of the initial photon interaction. The average value of this spread represents the size (diameter) of the initial charge cloud. To estimate that parameter, only those single interactions of 'PE' type were included.

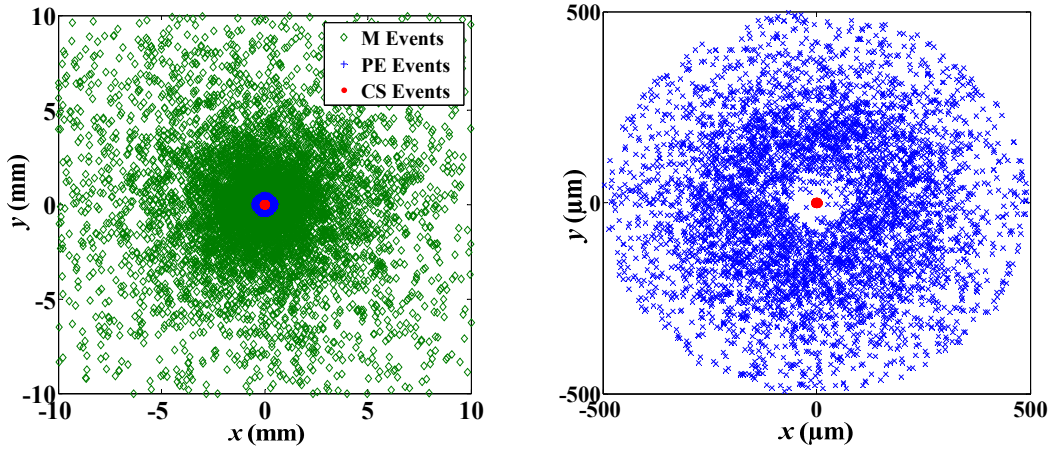

(a) (b)

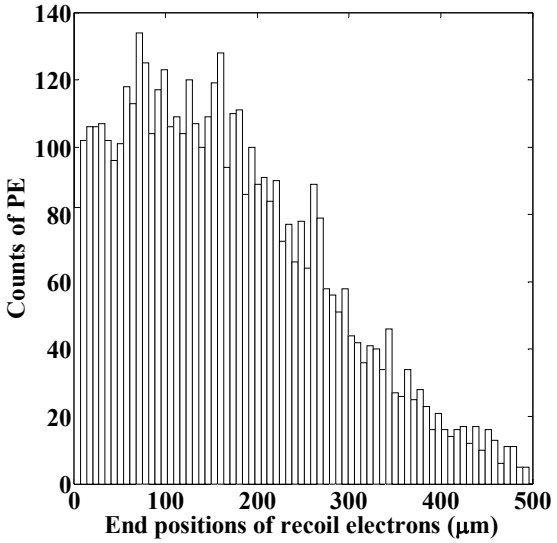

(c)

Figure 2-6, (a) Illustration of three categories of interactions between 511 keV gamma ray and the CZT detector (*L*=5mm). (b) 2D spatial distribution of PE interaction sites and the end positions of recoil electrons. (c) The histogram of the range of recoil electrons in PE interactions (average value: 167.5 μm).

Figure 2-6 shows the example of spatial distribution for all types of interactions. Green dots are 'M' events, red dots are 'CS' events and blue dots are 'PE' events in Figure 2-6 (a). The incident photon energy is set to 511keV. CS events show less blurring than photoelectric absorption. This is because that the recoil electron gets less energy from Compton scattering, resulting in a shorter travel distances. For PE events, the spatial distribution of the endpoints of photoelectrons is shown in Figure 2-6 (b). Figure 2-6 (c) demonstrates the histogram of the distance between the initial location where a PE event occurs and an endpoint where the electron eventually stops. The average distance is found to be ~167.5 μm and this value was selected as the initial size (diameter) of the electron cloud in the subsequent studies.

Table 2-1, The probabilities of each type interaction (511keV)

L	$\mathbf{R_{CS}}$	$\mathbf{R_{PE}}$	$\mathbf{R_M}$	**Single/Multiple interaction ratio**
1mm	56%	17%	27%	2.7
5mm	49%	17%	34%	1.9
10mm	39%	17%	44%	1.3

Table 2-1 shows the ratios of PE, CS and M events for three detector thicknesses (1 mm, 5 mm, and 10 mm). For a thickness of 5 mm, the ratio is 17% (R_{PE}), 49%

(R_{CS}) and 34% (R_M), respectively. The ratio between single and multiple interactions, (R_{CS}+R_{PE})/R_M, is ~1.9. R_{PE} remains constant (~17%) for three thicknesses since it is determined only by the photoelectric cross-section of the CZT material. For a CZT-based PET system, there are two trade-offs to be considered here in terms of detector's thickness. First, a thicker detector would yield higher intrinsic detection efficiency and improve the counting statistics. This is desired for high energy gamma rays, especially since single crystals up to 1 cm thick are now commercially available. Second, a thicker detector causes lower single to multiple interaction ratio as shown in Table 2-1. This is due to the increase in the number of events that undergo multiple interactions over single interactions. Multiple interactions suffer more from hole trapping effects, DoI effect and a longer drift time, which may subsequently degrade both energy and time resolution. As a result, it will produce more mispositioning and image resolution blurring, as illustrated in Figure 2-6 (a). For PE events, the mispositioning can be reduced for a thinner detector (~1-2 mm), since characteristic X-rays have a better chance to escape. In addition, applying a very high bias across a thin detector can help in collecting holes.

2.2. Induced Charge in a CZT Detector

2.2.1. The Shockley-Ramo Theory

From previous simulations, we know that a number of electron-hole pairs are generated when a photon hits the detector. An electric field is applied across the detector to drift the electrons toward the anode and holes toward the cathode. Then, the movement of the charge carriers induces an electrical signal on the electrodes.

The Shockley-Ramo theory was originally introduced for vacuum tubes where there was no space charge. Later, generalization of the Shockley-Ramo theory to cases with stationary space charge leads to wider application in predicting output signals from many types of charge sensing devices [92], [93]. It provides a way to calculate the induced signal due to the motion of moving charge carriers [6]. From the Shockley-Ramo theory, an analysis of induced charge depends on the weighting potential, geometry of the detector/electrode and material properties. The weighting potential is a unitless quantity and is solved using an electromagnetic field simulation

software package, for example Maxwell 3D from Ansoft was used in this thesis. In principle, setting the voltage of electrode of interest to 1, the others to 0 and assuming no space charge, the weighting potential Φ_ω can be solved through Laplace's equation in equation (2-4).

$$\nabla^2 \Phi_\varpi = 0 \tag{2-4}$$

The initial charges created by deposited energy $\underline{E_{deposited}}$ are given in equation (2-5),

$$q_0 = q_e \cdot N_e = q_e \cdot (E_{deposited} / E_{e\_h}) \tag{2-5}$$

where q_e is the elementary electron charge and N_e is the number of electron-hole pairs. E_{e_h} is the electron-hole pair generation energy (i.e. 4.64eV in CZT). For example, a 511 keV photoelectric interaction in CZT would produce ~110,000 electron-hole pairs. Then, the induced charge $Q(t)$ and current $i(t)$ build up as the electron-hole pairs move from position r_1 to r_2, as described in equations (2-6) and (2-7):

$$Q(t) = -q_0 \left(\Phi_\omega(r_2) - \Phi_\omega(r_1) \right) \tag{2-6}$$

$$i(t) = -Q_e \upsilon_e E(x) + Q_h \upsilon_h E(x) \tag{2-7}$$

where υ is the instantaneous velocity of the charge and E is the electric field. First, from equation (2-6), we note that the induced charge on the electrode is only determined by the starting and stopping positions of the charge carriers. It is independent of the actual electric field and the space charges. The actual electric field only determines the velocity and the trajectory of moving charge carriers. Second, it provides an easy way to calculate the induced charge on any specific electrode, even in a complicated electrode configuration. The drift times of an electron and a hole $t_{e/h}$ required to travel a distance of Δx are:

$$t_{e/h} = \Delta x / \mu_{e/h} E(x) \tag{2-8}$$

where $\mu_{e/h}$ is mobility of an electron and a hole, respectively. FEM is used to analyze the transport of charge carriers within the CZT detector as a function of several parameters such as pixel size (a), detector thickness (L), multiple lateral locations and DoI.

For compound semiconductors used in radiation detection, modern crystal growth practices lead to a much lower density of defects, which are trapping sites, and hence

shorter lifetimes. Thus, the current is reduced by a factor of exp(-t/τ) or exp(-x/λ), where τ and λ are the mean lifetime and mean drift lengths of the charge carriers, respectively, when charge trapping is involved. For CZT detector, typical lifetimes are $\tau_e = 3\times10^{-6}$ s and $\tau_h = 2\times10^{-6}$ s of electrons and holes, respectively [25]. Poor mobility-lifetime products, especially for holes, result in short λ, which limits the maximum thickness of the detectors and results in a significant reduction of the useful energy range. Further, the random distribution of the interaction locations increases the fluctuations on the induced charge and thus produces peak broadening in the energy spectra.

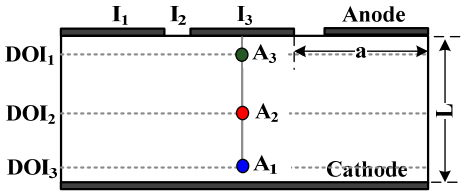

Figure 2-7, Illustration of analytical modeling as a function of detector parameters and multiple spatial positions.

In this chapter, simulations were performed to study the dependence of weighting potential on a/L and the dependence of induced charge on DoI. As illustrated in Figure 2-7, three interaction depths (10%, 50% and 90% of the detector thickness) are selected as A_1, A_2 and A_3.

Based on the equation (2-6), the calculated 2D weighting potential profile of four aspect ratios (a/L) is shown in Figure 2-8. The top is associated with the anode with a potential of 1 while the bottom is associated with the cathode with a zero potential. z direction refers to the direction perpendicular to the anode and cathode planes. L is constant at a value of 5 mm. In Figure 2-8 (a), it is observed that for a/L of 0.1, Φ_ω (x, z) is approximately zero everywhere except in the immediate vicinity of the anode, where the equipotential lines are dense. This means that an appreciable charge signal would be induced only if the space charge is very close to the anode, i.e. in the near field. At a/L of 1, Figure 2-8 (d) shows the equipotential lines distribute evenly along the whole detector depth, and Φ_ω (x, z) varies approximately linearly from 1 to 0 along the electrode axis strip (r=2.5mm). This suggests that wider electrodes are much more sensitive to space charge in the far field.

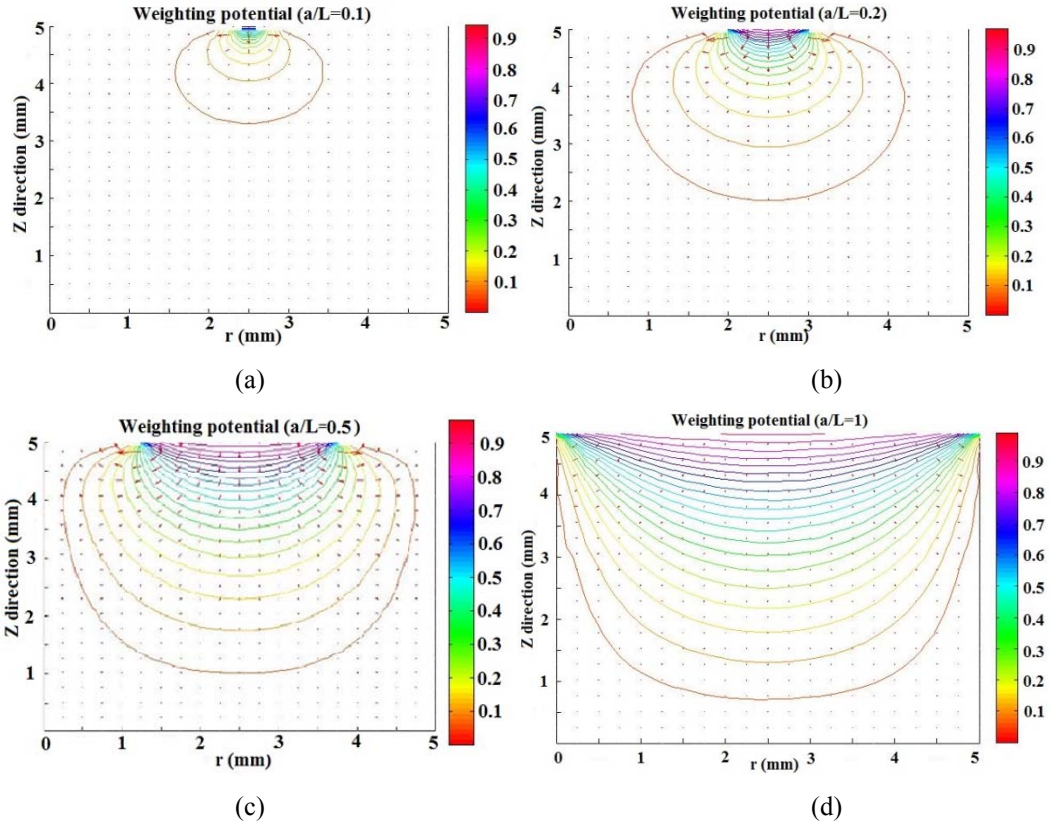

Figure 2-8, Illustration of the distribution of weighting potential.

Further, we extracted the profile of the weighting potential along the vertical line passing through the center of the anode (r=2.5mm) and plot the result in Figure 2-9. In general, the weighting potential results exhibit a similar trend for different a/L, a slow increase near the cathode (z=0) followed by a rapid increase towards the anode (z=5). Such a tendency is associated with the small pixel effect and single polarity sensing technique, which affects both charge collection and temporal response of CZT detectors. As the a/L ratio decreases, the weighting potential shows a more abrupt increase towards the anode region, which implies that the incomplete charge collection can be mitigated more effectively. According to the equation (2-6), this means that the charge induced on the anode is less dependent on the DoI and is primarily dependent on the total energy absorbed.

2.2.2. Induced Signal Analysis

The charge buildup of anode is calculated and shown in Figure 2-10. First, we know that the anode is sensitive only to space charge in the near field. Consequently,

the anode signal's rising edge appears relatively instantaneously after a near field photon interaction (< 40 ns, A_3: green curve). Comparing this signal rise with that of the same photon interaction at far field area (A_1 and A_2: blue and red curves), the finite transport time of electrons to the anode imposes a delay on the onset of the anode signal's main rising edge, which appears ~200 ns later than the near field counterpart.

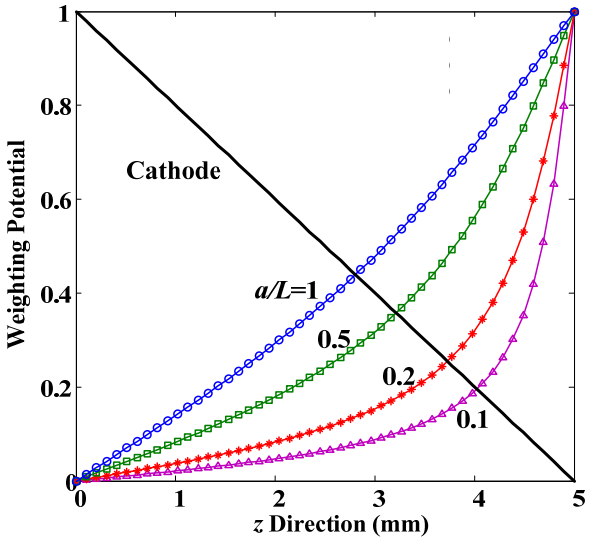

Figure 2-9, Profiles of the weighting potential along the central line (r=2.5 mm) for four different a/L ratios.

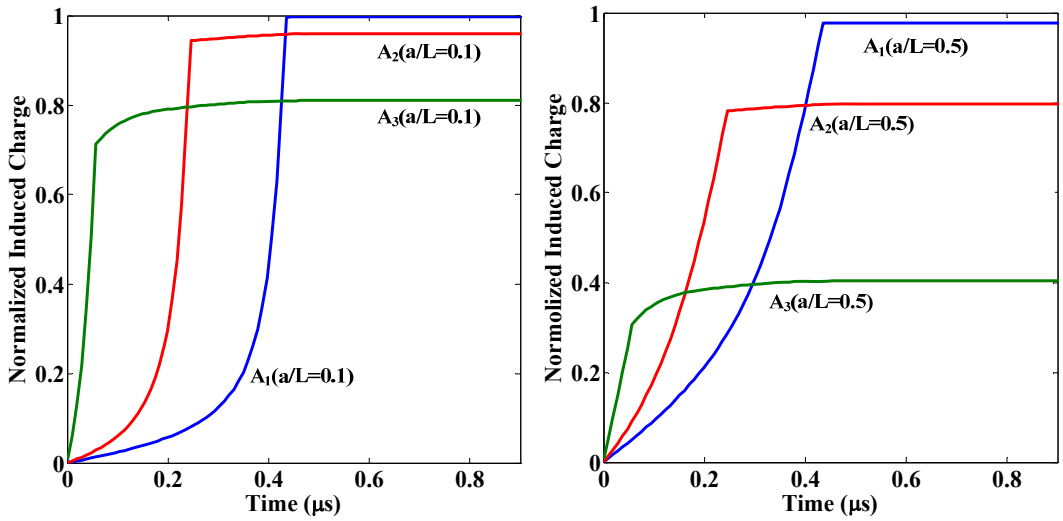

(a) (b)

Figure 2-10, (a) Induced signals for an anode a/L ratio of 0.1 for 511 keV photon interactions at three interaction (A_1, A_2 and A_3) positions. (b) shows the same information as (a) but for an anode a/L ratio of 0.5. The photon interaction occurs at t = 0 μs.

Second, the anode signal's temporal profile is composed of the fast rising and slow rising parts, which are distinct contributions of the electrons and holes, respectively. Because of the poor mobility of holes, the collection time of holes is much longer. In thick detectors, it is often impractical to measure the contribution to the total induced charge of the slowly moving holes. Therefore, there is charge loss during the finite collection time of the readout electronics.

Third, a monoenergetic particle interacting at different depths relative to an electrode would induce different amounts of charge on that electrode. The signal amplitude of the near field photon interaction (A_3) is visibly lower than that of the far field cases (A_1 and A_2). This degradation of total induced charge is worse when interaction depth is close to the anode.

If we compare the signal amplitude of the near field photon interaction at 200 ns and at 900 ns (red curves in Figure 2-10 (a) and (b)), we can conclude that the electron current contributes almost 100% of the anode signal. The anode signal is essentially insensitive to the hole current and the detector behaves as a single-carrier device. Comparing the results in Figure 2-10 (a) and Figure 2-10 (b), the insensitivity to space charge in the far field (A_2 and A_3) due to *a/L* ratio is commonly referred to as the "small pixel effect", which can be exploited to effectively turn the CZT photon detector into a single-carrier device. In addition, the difference between the amplitude of signals along whole thickness is smaller with smaller *a/L* ratio. By controlling (specifically limiting) the anode sensitivity to holes in CZT, the amplitude of the anode induced signal can be made maximally invariant to the photon's interaction position.

Therefore, single polarity charge sensing technique can be adopted with pixelated CZT detector to compensate for the limitations due to the hole's trapping effect. Besides this, a pixelated detector has additional advantage that the leakage current and the detector capacitance are shared by all pixels. Therefore, the electronic noise should be greatly reduced for each pixel.

2.2.3. Interaction Depth Sensing

As described above, single polarity charge sensing techniques can solve the severe hole trapping problem in wide bandgap semiconductor detectors. However, the

trapping loss of electrons can still broaden the photopeak due to different electron drift lengths when photons interact inside the detector at random depths. As an example, for a CZT detector of 1cm thickness and -2000V bias voltage, typically ~15% of those electrons generated near the cathode will not be collected at the anode due to electron trapping [94]. This means that the pulse height of the anode signal may still vary by 15% for the same energy deposition depending upon the interaction depth, which would cause a significant degradation of the energy resolution in the energy spectrum.

Several techniques to mitigate the impact of electron trapping on the energy resolution were developed. For coplanar grid anode designs, one method to compensate for electron trapping is to apply a relative gain when subtracting the non-collecting anode signal from the collected anode signal ($\varphi = \varphi_{CA} - G\,\varphi_{NA}$, $G < 1$). In this way, the signal of a gamma-ray interaction at the cathode side is higher due to the weighting potential, thus the electron trapping effect can be compensated [6]. For pixelated anode designs, although the shape of the weighting potential mitigates the effect of the electron trapping problem, the pixel size and the bias voltage need to be carefully chosen to optimally compensate for electron trapping. However, since the electron transport properties (mobility μ_e and lifetime τ_e) can vary from detector to detector, it is impractical to optimize the pixel size for every detector. Even if the pixel size is fixed, there is only one optimal bias voltage under which the electron trapping can be fully compensated, and that optimal bias voltage is usually different from the actual operating bias voltage.

In general, unlike the anode signal, the slope of the cathode signal is determined primarily by the energy of interactions, while the amplitude of the cathode signal is determined by the photon interaction's position, as illustrated in Figure 2-11. Since the amplitude of cathode's signal is proportional to the DoI, then it is possible to use it in extracting depth information. In addition, for photopeak events with same deposited energy, the results give the clue to perform depth calibration and optimally compensate for electron trapping with the cathode's signal.

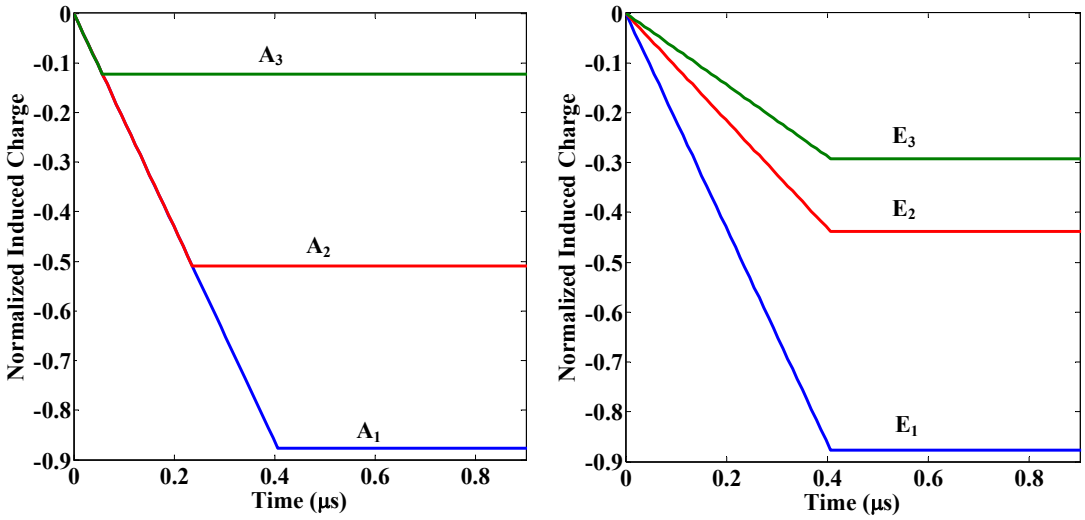

Figure 2-11, Cathode signals in CZT vary with (a) different depth (A_1, A_2 and A_3), and (b) different incident energy (E_1>E_2>E_3). The photon interaction occurs at t = 0 μs.

2.2.3.1. Depth sensing by cathode-to-anode ratio

Since electron trapping is a monotonic function of the interaction depth, if the interaction depth can be derived from the signals available from the detector, then the photopeak centroid as a function of the interaction depth can be calibrated and used to correct for electron trapping. As already shown in Figure 2-9, the weighting potential of the cathode has a linear relation with the interaction depth. Then a method to correct the signal by using the cathode to anode (C/A) ratio can be proposed [95], [96]. Based on single polarity charge sensing, holes can be considered as stationary during the collecting period of electrons. For an energy deposition at an arbitrary depth, the anode signal amplitude V_a is proportional to the number of electrons (n)

$$V_a = K_a n \tag{2-9}$$

The cathode signal amplitude V_c is proportional to the number of electrons (n) and the interaction depth (z is the distance from the interaction position to the anode), so V_c is

$$V_c = K_c n z \tag{2-10}$$

where K_a and K_c are constants, respectively. Thus the C/A ratio is

$$\frac{V_c}{V_a} \propto \frac{nz}{n} = z \tag{2-11}$$

In practice, the C/A ratio is not exactly linearly proportional to z because of electron trapping and non-ideal single polarity charge sensing. However, in most cases, the C/A ratio still has a monotonic relationship with the interaction depth and can be used for depth sensing and applied to pixelated detectors. Together with the 2D position sensing capability associated with the pixelated anode array, this technique can provide the 3D position information of gamma-ray interactions in the detector [97], which can also aid in minimizing the parallax error in PET imaging. In addition, by conceptually dividing the whole detector thickness into several tens of depth bins, the pulse amplitude in each bin can be corrected as a function of interaction depth. Therefore, the variation of the pulse amplitude due to charge trapping and material non-uniformity can be minimized to the extent of the position resolution [98], [99]. Then, sorting all events into sub-spectra according to depth bins, the photopeak centroid of each sub-spectrum is measured and aligned to the same position using a gain factor. As a result, a much narrower photopeak than the uncorrected one and better energy resolution can be obtained. Moreover, the depth resolution from C/A ratio can be derived as

$$FWHM_{dr} = \sqrt{\left(\frac{FWHM_c}{V_c}\right)^2 + \left(\frac{FWHM_a}{V_a}\right)^2} \times \frac{V_c}{V_a} \tag{2-12}$$

2.2.3.2. Depth sensing by electron drift time

The C/A ratio depth sensing can be used for single interaction events, since the cathode signal is linear with the interaction depth and the anode signal is only slightly depth dependent. However, for multiple-interaction events, the C/A ratio can no longer be used to get the individual interaction depth, since the cathode signal is now a sum of several interactions. It can only provide the energy weighted centroid depth of the multiple interactions [100].

Because of the weighting potential, the cathode will be triggered shortly after the electrons are created by the energy depositions, which means as soon as electrons begin to move, they induce a signal on the cathode. The anode signal is small, and when electrons drift within around one pitch away from the anode surface, the anode

signal will be triggered (as shown by the times to reach the trigger threshold in Figure 2-12). The electrons normally drift at a constant velocity under a fixed electric field. After applying the triggering threshold, the drift time of each anode pixel signal can be measured. As a result, the time difference between the cathode trigger and each anode pixel trigger can be used to estimate the interaction depth.

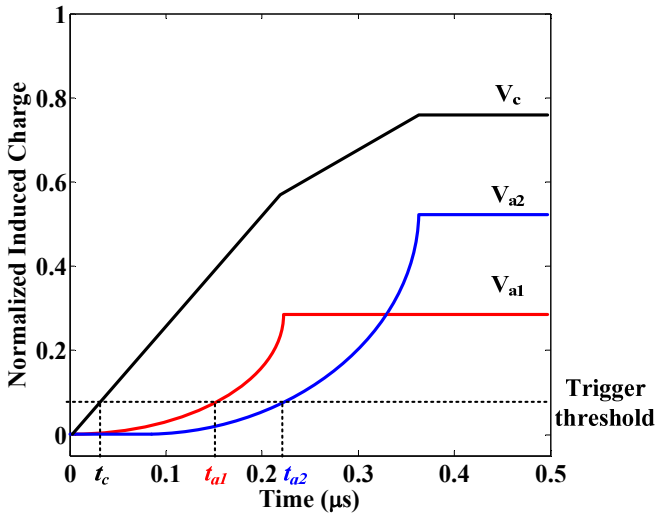

Figure 2-12, Depth sensing by measuring electron drift time for multiple-interaction events.

Figure 2-12 gives an example of a two-interaction event: a photon first interacts in one anode (V_{a1}) by Compton scattering, and then the scattered photon is captured in another anode pixel (V_{a2}) by the photoelectric effect. The leading edge timing of the cathode signal (V_c) t_c provides the time origin when the electrons start to drift towards the anode, and the leading edge timing of the anode pixel signals t_{a1}, t_{a2} give the electron's arrival time at each individual pixel. Therefore, the electron drift times for the two interactions t_{d1}, t_{d2} can be determined by $t_{d1}= t_{a1}- t_c$ and $t_{d2}= t_{a2}- t_c$, respectively. For interaction events in a CZT detector, the electron drift time and electron drift distance have a monotonic relationship which depends on the detector bias voltage. With calibration, the interaction depth z_1, z_2 can be determined from the measured t_{d1}, t_{d2} since z_1, z_2 can be considered as the electron drift distance corresponding to the two interactions. As an alternative method to reconstruct z_1 and z_2, only the timing information from the two pixels t_{a1}, t_{a2} need to be read out to

determine z_2 and z_1. The weighted centroid of z_1 and z_2 can be determined by the C/A ratio. Thus z_1 and z_2 can be obtained.

Because the electron drift time is determined by the time difference between the cathode trigger and the anode trigger, the depth resolution derived from the electron drift time can be expressed as:

$$FWHM_{dr} = \frac{\sqrt{FWHM_{cT}^2 + FWHM_{aT}^2}}{T} \times L \tag{2-13}$$

where $FWHM_{cT}$ and $FWHM_{aT}$ are the timing resolution for the cathode and anode trigger, respectively. T is the maximum electron drift time when the electron travels the whole detector thickness L. In particular, for the collection of mobile electrons, smaller anode pixels are preferable in order to achieve high fidelity photon interaction energy measurements, at the cost of delayed signal formation.

2.3. Radiation Detector Electronics

In this thesis, the detector crystal was grown by Redlen, Inc. using high-pressure Bridgman method. The bulk size is 20mm×20mm×5mm. On one 20mm×20mm surface, the electrode metal for 8×8 anode pixels is deposited. The cathode metal covers another entire surface. The leakage current, which is also known as the dark current, is the current flowing through the detector terminals when there are no photons being detected. The test from Redlen, Inc.[101] of the total leakage current for the 20×20×5mm^3 pixelated detector (measured over all 8×8=64 pixels) is less than 20 nA or less than 0.31 nA per pixel at 400 V bias, allowing the device to be operated at much higher bias as needed.

Due to the fabrication limitation (small pixel size, thin gold layer and high voltage operation), the sandwich structure (spring Loaded Pogo pins & ZEBRA® W Series Matrix Connectors (Fujipoly Company)) is adopted for pixelated CZT as shown in Figure 2-13. The ZEBRA is a silicone rubber sheet with anisotropic conductive properties, containing 300 to 2000 fine metal wires per 1cm^2, see right side in Figure 2-13. The fine metal conductors are gold-plated to ensure low resistance and the ability to withstand a relatively high current flow. Therefore, ZEBRA facilitates denser and less expensive packaging very well. After inserting the correctly sized

connector pad between the opposing groups of electrodes, all that is necessary is to apply the appropriate pressure to allow the electrodes to be properly connected [102].

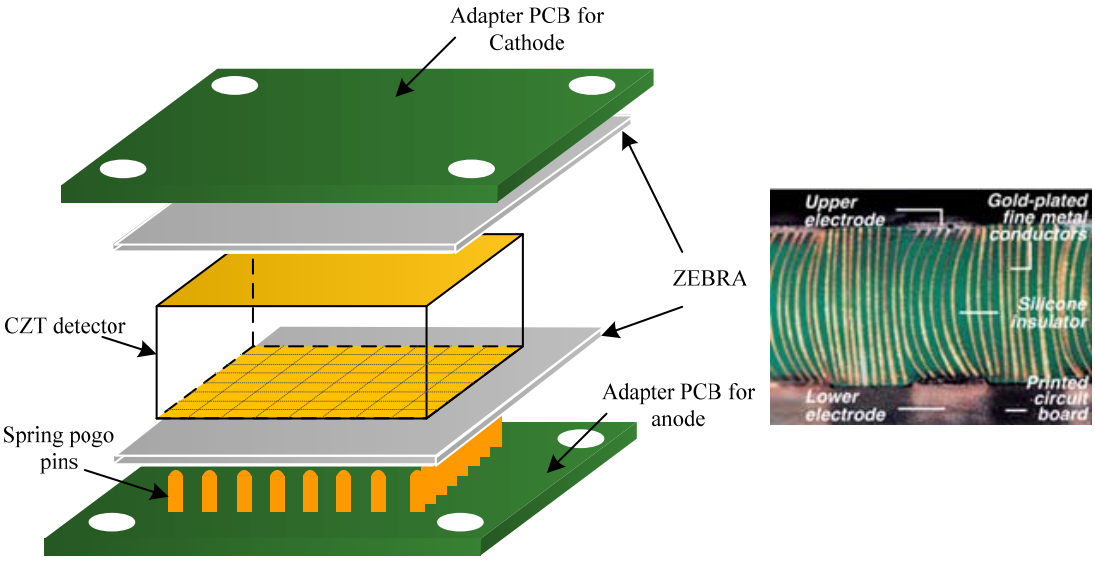

Figure 2-13, Left: Package Design for Pixelated CZT detector. Right: 35× magnification side view exhibits compression of fine ZEBRA metal conductors (reprinted from [102] with permission granted)

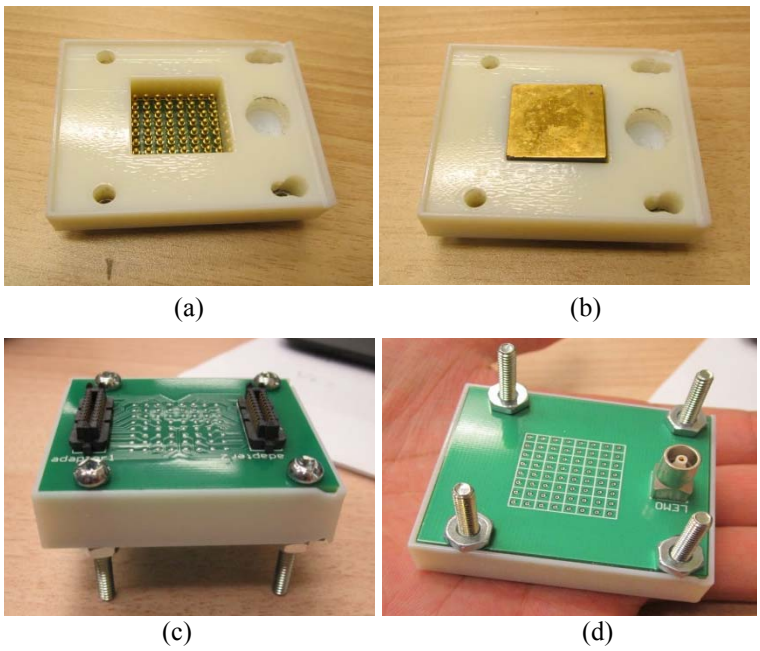

Figure 2-14, (a) 8×8 spring loaded pogo-pins and holder are used to contact with anodes of CZT. (b) CZT detector is constrained within the holder. (c) Adapter board for anode with two connectors. (d) Adapter board for cathode.

Based on this sandwich structure, a holder is designed to make it compact and easier to align, as shown in Figure 2-14. The CZT detector is constrained within the

holder. One adapter printed circuit board (PCB) is designed to couple to the readout anode signal using either application specific integrated circuit chips (ASIC) or customer-designed electronics. Another adapter PCB is designed to read out the cathode signal and apply a high bias voltage at the same time. For each anode pixel, an individual readout chain, working as AC-equivalent coupling is required.

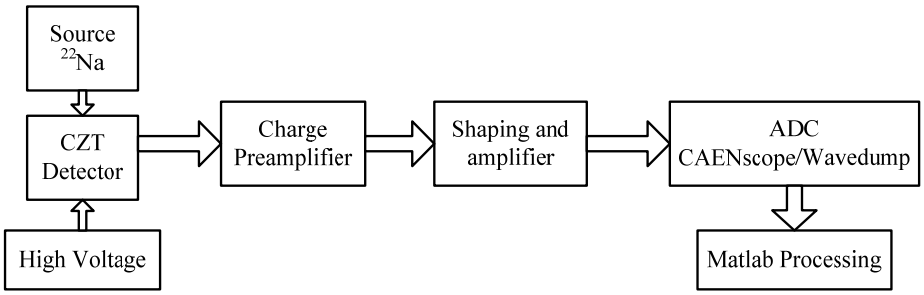

Figure 2-15, Front-end circuit configuration for the readout of a semiconductor photon detector.

In this section, we will describe the electronic elements of the detection system used in PET detector signal chain. The system block diagram is shown in Figure 2-15. In general, the most basic front-end electronics are composed of a charge-sensitive preamplifier, shaping amplifier and analog-to-digital converter (ADC).

2.3.1. Charge Sensitive Amplifier

In a pixelated device, each pixel should be connected to an independent preamplifier, the first stage of the signal chain. The purpose of the preamplifier is to, 1) integrate the current signal into a voltage signal, which is proportional to induced charge, and 2) act as a buffer for the detector by isolating the loading effects of the subsequent signal processing stages.

The preamplifier is usually located as close as possible to the detector. From signal-to-noise considerations, it is preferable to minimize capacitive loading on the preamplifier. Therefore, long interconnecting cables between the detector and preamplifier should be avoided whenever possible. Because of convenience or safety considerations, the components that follow in the pulse processing chain often are located at some distance from the detector and preamplifier. Thus, another requirement for the preamplifier output stage is to be capable of driving its signal into the large capacitance represented by the long interconnecting cable, or that it has a low output impedance. Typically, the preamplifier provides no pulse shaping, and its

output is a pulse, in which the decay time is usually quite large (typically 50 to 100 μs). Because of the long decay time, full collection of the charge from detectors with widely differing collection times can occur. Also, the rise time of the output pulse is kept as short as possible, so it is consistent with the charge collection time in the detector itself.

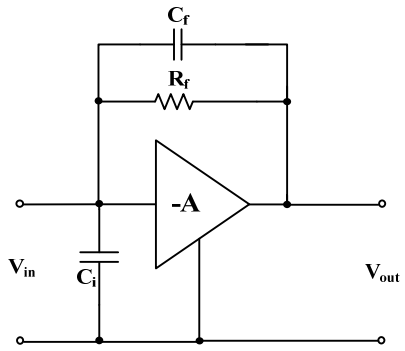

Figure 2-16, Diagram of the charge sensitive preamplifier.

Preamplifiers can be either voltage-sensitive or the charge-sensitive. In semiconductor detectors, the detector capacitance may change with operating parameters. In these situations, a voltage-sensitive preamplifier is undesirable because its response is also affected, so charge sensitive preamplifiers are preferred. The simplified diagram of a charge sensitive preamplifier is shown in Figure 2-16. The output voltage is obtained by following equations.

$$V_{out} = -AV_{in} \tag{2-14}$$

$$V_{out} = -A\frac{Q}{C_i + (A+1)C_f} \tag{2-15}$$

$$V_{out} \cong -\frac{Q}{C_f}(assume\ A >> (C_i + C_f)/C_f \tag{2-16}$$

Here, C_i is the equivalent input capacitance, and C_f and R_f are feedback capacitor and resistor, respectively. From equations (2-14) to (2-16), we can see that the output voltage V_{out} is proportional to the total integrated charge Q in the pulse provided to the input terminals. It is independent of the input capacitance C_i. The decay time of the tail of the V_{out} is determined by the time constant given by the product R_fC_f, which should be longer than the duration of the input pulse.

2.3.2. Signal Shaping

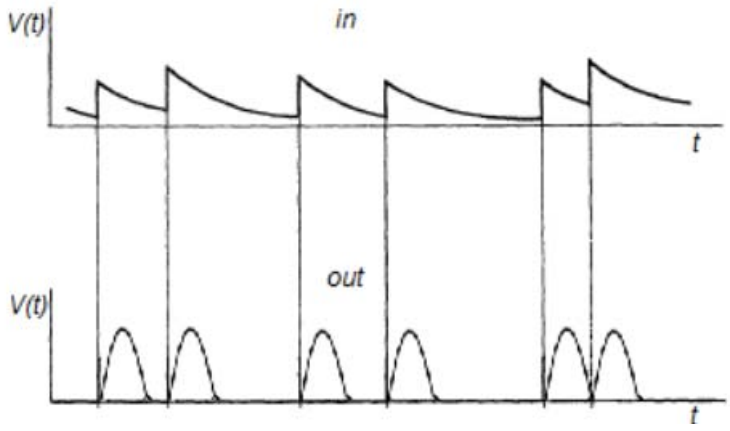

Figure 2-17, The effect of pulse shaping on long preamplifier signals to avoid pile-up (reprinted from [25] with permission granted).

Usually, the preamplifier signals with a narrow-peak and long tail are too fast for digital converters to accurately measure, and would cause pile-up [25] shown in Figure 2-17. Pile-up results from two or more events in close temporal proximity interfering with subsequent pulses which ride upon the tail of the preceding pulses, causing a change in pulse shape and height which can confuse measurements. Because of the random nature of nuclear events, there is the possibility that more than one event occur in rapid succession. The pulse shaping is then used to round the peak and shorten the signal tail to facilitate measurement and avoid pile-up.

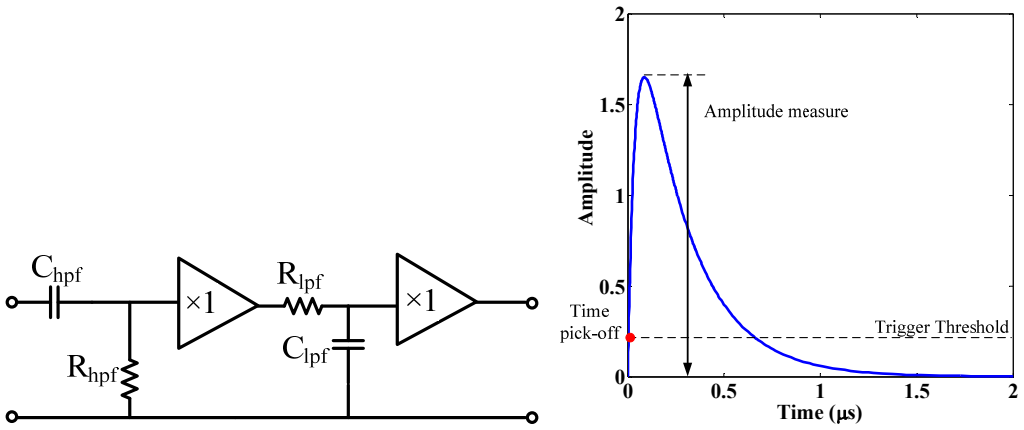

(a) (b)

Figure 2-18, (a) CR-RC shaping circuit. (b) Step response of CR-RC pulse shaper ($C_{hpf}R_{hpf} = R_{lpf}C_{lpf} = 1\mu s$).

One of the simplest shaping methods is accomplished using a CR-RC shaping circuit (differentiator-integrator). These two components of the shaping system are also known as high and low-pass filters in the frequency domain, respectively. One purpose of pulse shaping is to improve the SNR by limiting the response of the instrumentation to those frequency ranges in which the signal has useful components, while reducing as much as possible the transmission of various noise signal at other frequency components to V_{out}. The higher order integrators ($CR\text{-}RC^n$) are referred to as Gaussian shaping due to the resulting signal shape. Figure 2-18 shows an example of implementation and response of a *CR-RC* filter circuit for a step function input with an equal time constant $\tau_{shaping} = C_{hpf}R_{hpf} = R_{lpf}C_{lpf}$. There also exist many circuit topologies using active components that can be advantageous over passive implementations with higher gain and filter quality factor, and improved SNR [103].

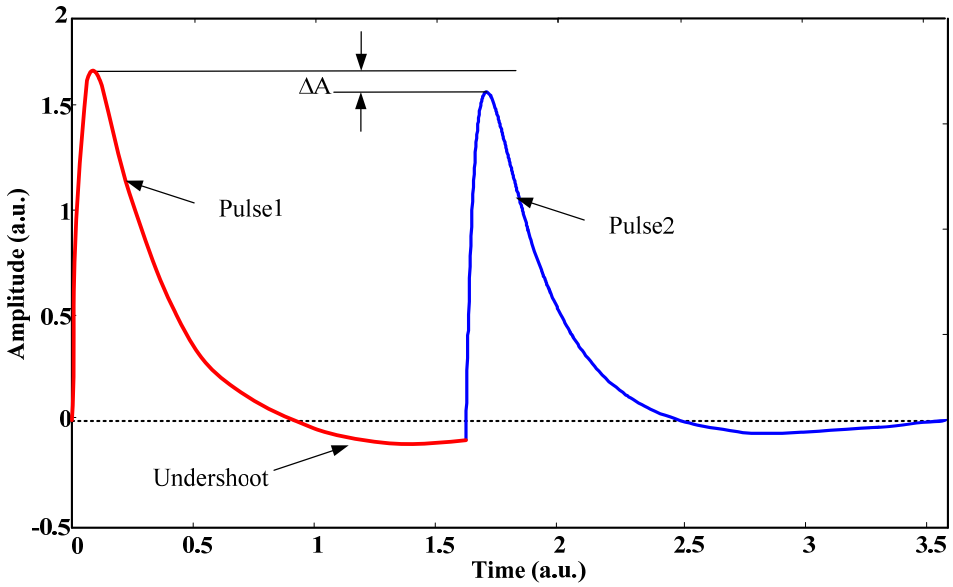

Figure 2-19, Shaper output with undershoot (Pulse1=Pulse2).

Although the decay of the preamplifier pulse is usually long, it is not infinite and the finite decay will have a measurable effect on the response of the networks discussed above. For example, a basic CR-RC differentiator-integrator will no longer produce a strictly unipolar response if the input pulse has the finite decay. Instead, there will be a slight zero crossover or undershoot of the pulse, which then recovers back to zero with a time characteristic of the preamplifier decay time. Because the undershoot of preamplifiers persists for a relatively long time (~tens of μs), then if

another pulse arrives during this decay time, it will be superimposed on undershoot and an error will be induced in its amplitude (ΔA in Figure 2-19). The problem is particularly severe for very large signal pulses and consequently leads to rather large following undershoot. Pole-zero cancellation modifies the shaper so that any overshoot would return quickly back to zero, thereby minimizing the amplitude reduction. Therefore, two other functions are often implemented in this stage: signal gain above unity, and pole-zero cancellation.

2.3.3. Energy and Time Measurement

The amplitude of shaper output signal corresponds to the interaction energy. In some systems, the sample/hold circuit followed by free-running ADC is used to acquire just a single sample of the shaper output's peak amplitude, which has the advantage of lower power consumption and data volume. However, in order to apply interaction depth sensing technique, typically all waveforms are stored, but this increases the data volume and processing time. In this case, the output from the shaper is directly fed to a free-running ADC. Then, extra post-processing in computer is required to extract the energy and time information. Eventually, the energy spectrum can be obtained, which is the histogram of the amplitude of recorded PE events.

According to the equation (1-2), the energy resolution of system is determined by both photopeak energy (E_0) and FWHM of photopeak (ΔE). First, in order to convert ADC values to their equivalent values in keV, we can relate the ADC value of specific spectral features to their keV values at known energies, e.g. radiation sources ^{137}Cs (photopeak: 662 keV) and ^{22}Na (photopeaks: 511 keV and 1274 keV), respectively. Then, this can be used to eliminate the nonlinearity of system. Second, the Gaussian fitting is used to extract E_0 and ΔE (Chapter 1, section 1.1.3). Third, because of electron trapping and other system non-ideal factors such as electronics' variation, usually the depth calibrations are adopted to achieve better performance (Chapter 2, section 2.2.3).

The most fundamental operation in time measurements is the generation of a logic pulse whose leading edge indicates the start time of photon absorption. There are fluctuations leading to some degree of uncertainty in deriving the time signal, and

which can be divided into two categories: time walk and time jitter that are shown in Figure 2-20.

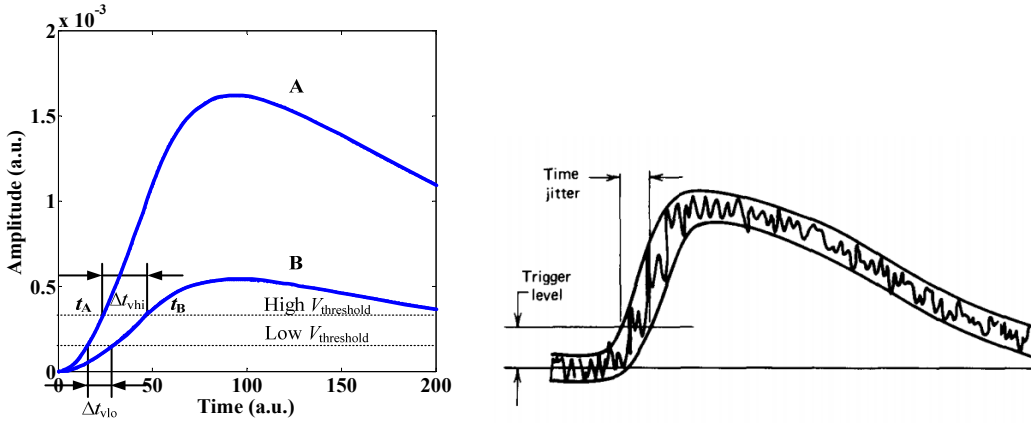

(a) (b)

Figure 2-20, (a) The effect of time walk. (b) The effect of time jitter (reprinted from [25] with permission granted)

Time walk is related to variations in the signal shape, particularly the rise time which is typically the highest frequency portions of the signal. It occurs when the amplitude of the signal changes and subsequently changes the slope of the rising edges. Time walk is a strong function of the triggering method used. It is an inherent drawback of the leading edge discriminator. In Figure 2-20 (a), we can see that for a fixed threshold, signal A and B will trigger the discriminator at different times t_A and t_B, although they are exactly coincident. It further shows that time walk is exacerbated by a higher V_{thresh}, i.e. $\Delta t_{vhi} > \Delta t_{vlo}$. In hardware, time walk can be reduced by setting the threshold V_{thresh} to the lowest practical level, which is lower bounded by the noise floor.

Time fluctuations are caused by 1) the electronic noise added by components that process the linear pulse prior to the time pick-off; 2) the discrete nature of the electronic signal as generated in the detector. Because of these random fluctuations in the shaper output pulse, there are differences in time measurements observed for a pulse at some fixed point in time, which is referred as time jitter in Figure 2-20 (b).

The equation giving the relationship between the signal noise σ_V and the time noise σ_t is

$$\sigma_t = \frac{\sigma_V}{dV/dt}. \tag{2-17}$$

This equation shows that time jitter can be minimized by both i) positioning V_{thresh} in the signal range of the steepest part of pulse signals, which generally is the earliest rising part of a pulse (i.e. low V_{thresh}), and ii) larger dV/dt, i.e. pulses with steeper rising edges. This can be achieved by increasing the detector bias, which increases charge drift velocity and causes a more rapid induced signal.

A commonly used method for time pick-off is the simple leading edge discriminator. The trigger signal is asserted when the shaper output's rising edge exceeds a user-defined trigger threshold V_{thresh}. Under extreme conditions, the time walk can amount to the full rise time of the input pulse and is often unacceptable in situations where accurate time information is needed over a wide range of amplitudes. In this case with a leading edge discriminator, V_{thresh} should be set as close to the noise floor as possible. The time errors due to time jitter will be approximately systematic, and will increase if the slope of the leading edge of the pulse is decreased.

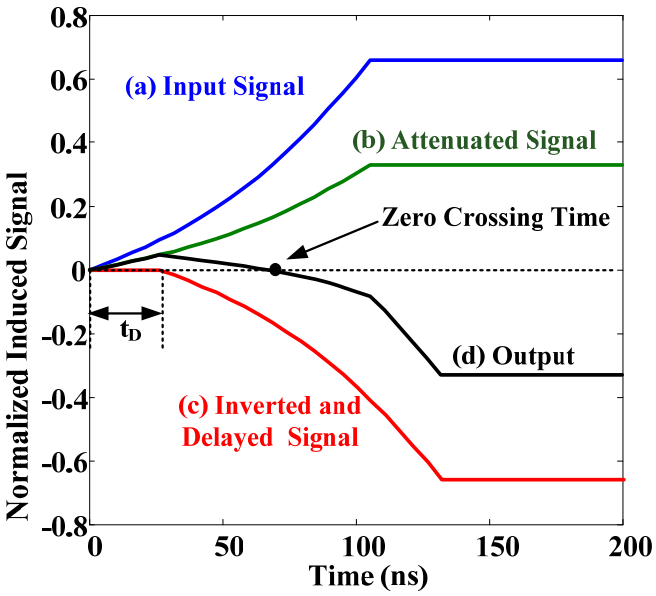

Figure 2-21, Waveforms in CFD time pick-off method (f = 0.5). For clarity, only the leading edge of pulse is shown.

The applicability, performance, and optimization of different methods depend on the signal properties and have been investigated by different groups [104]–[106]. Besides the leading edge discriminator, linear fitting and constant fraction

discrimination (CFD) method are used for timing pick-off. The CFD method [107], [108] was first used to extract timing information to avoid time walk and to minimize time jitter due to random noise. A digital constant fraction discriminator (dCFD) is similar to the analog CFD, which is easily implemented in a computer or programmed in FPGA logic. It does this by altering the input signal, such that the zero crossing of the output is independent of the slope of the rising edge in an ideal case. In reality, noise will still interfere with the measurement, but time walk is greatly alleviated.

The electronic shaping steps required to carry out digital CFD are illustrated in Figure 2-21. First, the original signal (a) is attenuated by a factor of f as waveform (b). At the same time, the input waveform is inverted and delayed for a time (t_D) shown in waveform (c). The sum of waveforms (b) and (c) is then taken to give the pulse that is sketched in waveform (d). The time that this pulse crosses the zero axis is independent of the pulse amplitude and corresponds to the time at which the pulse reaches the fraction f of its final amplitude. Equation (2-18) describes the digital CFD method:

$$V_{CFD} = \sum_{i=1}^{L} \left(f * V_{i-1} - V_{i-D} \right) \tag{2-18}$$

where i is the index of the digital signal, f is the attenuation factor, D is the delay applied to the inverted signal, L is the length of the signal and V_{CFD} is the output. Since the signal is discrete, the zero crossing is determined by linear interpolation of the two points of V_{CFD} straddling the zero axis. The result will be a bipolar signal. The accuracy of this algorithm depends on the optimization of two parameters, f and D.

Another two numerical models, the linear and exponential rising-edge fitting methods were implemented by equations (2-19) and (2-20)

$$V_{LF}(k) = Ak + B \tag{2-19}$$

$$V_{EXP}(k) = 1 - \exp^{-(k-k_0)/\tau} \tag{2-20}$$

For the linear model, two parameters (A and B) were fitted, and then substituted in the model to calculate the k value that gives V_{LF} a zero value. For the exponential model, V_{EXP} is the signal after normalization. Such simplifications enable us to reduce the unknown parameters to k_0 and τ. For both models, the first several points on the pulse rising edge are used to extract pulse arrival time information. A threshold (~1-5% of

maximum pulse height) was adjusted and optimized to find the starting position of the pulse prior to the fitting.

2.3.4. The RENA-3 ASIC

Traditionally, the individual preamplifier, shaping, triggering and digitization modules based on the Nuclear Instrumentation Module (NIM) standard are used in laboratories. Although they can offer much modularity and versatility, it is not readily scalable. For example, for the high-resolution PET system in our research, 64 anode channels are required. Therefore, a much more compact solution would be the use of ASICs with larger channel density, lower power consumption, lower cost and easy implementation in a commercial founding.

The Readout Electronics for Nuclear Applications (RENA) developed by NOVA R&D Inc. is a 36-channel ASIC specifically for instrumentation of semiconductor photon detector signals. Self-trigger output is designed so that random signals without an external trigger can be processed. It also has several readout and data acquisition modes for versatile implementation and detailed testing [109]–[113]. The polarity, signal range, peaking time, and threshold are adjustable on a channel-by-channel basis. The key design features of the RENA-3 ASIC are listed in Table 2-2.

Each RENA-3 channel contains a charge-sensitive input amplifier with resistive-multiplier feedback, a differentiator, gain circuit, and two shaping amplifiers (“slow” and “fast”) that operate in parallel. The “slow” shaping amplifier is optimized for accurate pulse height determination with 16 user-selectable shaping times (15 ranging from 0.29 to 4.5 μs, plus 38 μs). It is followed by a peak detector and a trigger comparator. The “fast” shaping amplifier is optimized for triggering time measurement using a leading edge discriminator. It has a shaping time between 100 and 200 ns. The RENA-3 chip provides user-configurable threshold for triggering of both the fast and slow paths.

Table 2-2, The key design features of the RENA-3 ASIC

Features	RENA-3 IC Specifications
Signal Range	Two ranges; externally selectable for each channel (9fC/256keV & 54fC/1.5Mev for CZT)
Input Polarity	Positive or negative, selectable channel-by-channel
Peaking/shaping	User configurable shaping time from 0:29 μs to 38 μs.
Gain	User configurable from 1.6 to 5
Pole-zero cancellation	User configurable On or Off
Noise	150 e rms & 280 e rms for low & high ranges
DC leakage current	Tolerant to 5nA per channel
Power consumption	<6mW per channel

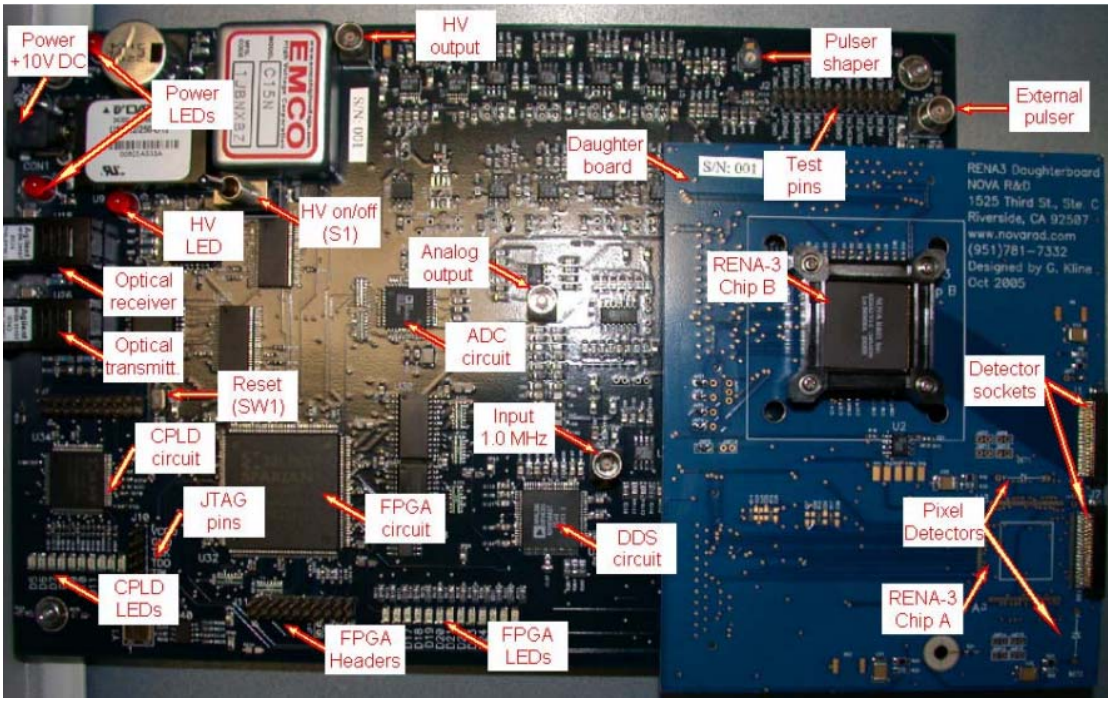

Figure 2-22, The RENA-3 main board top view with the daughter board plugged in. One RENA-3 chip (chip B) is installed in 144-pin CQFP socket.

The evaluation system for RENA-3 ASIC consists of a main board and a daughter card as shown in Figure 2-22. The main board supplies control signals to the ASIC, high voltage bias for detector, timing references and clocks, and digital communication with a PC over a fiber optic cable. The daughter card can carry two RENA-3 ASIC chips. It has minimal number of active electronic components and is designed for low noise operation. Two connectors on the edge of the daughter card allow a detector to be connected to it.

Through the configuration setting window in Figure 2-23, all parameters can be modified and saved. The RENA evaluation system has three different readout patterns. In the "SPARSE" pattern, only channels enabled and triggered (have a signal above the threshold of the low level comparator) are read out. In the "GLOBAL" pattern, all channels are externally enabled and read out. In the "NEAREST NEIGHBOR" pattern, the nearest (adjacent) channels immediately above and below the channel that has valid data are also read out. This mode is important if charge sharing between detector channels is expected to happen with significant probabilities.

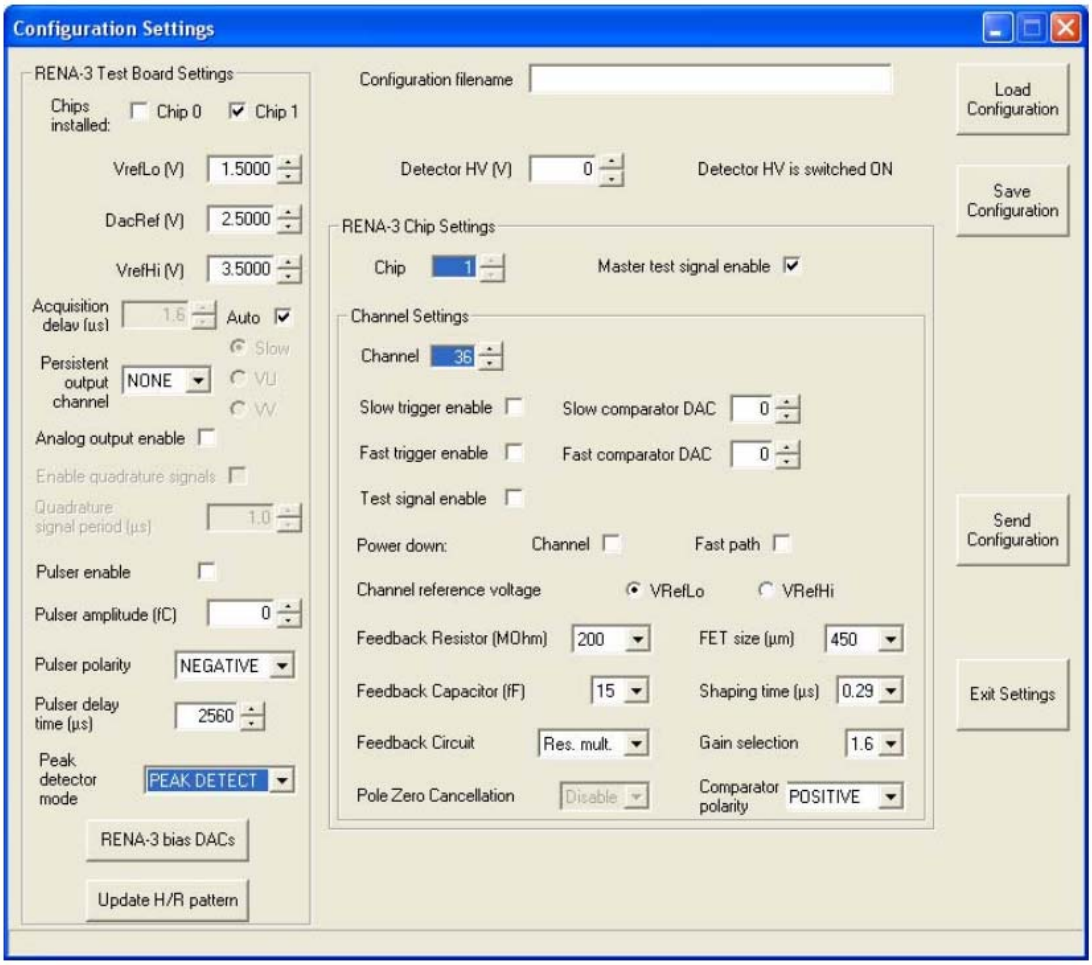

Figure 2-23, The configuration setting window.

For easy troubleshooting, RENA allows persistent monitoring of the analog output from one of the channels, which is referred to as "follower mode". The differential output pins to be directly connected to the shaper output of a particular channel internally, so that the shaper output can be analyzed using an oscilloscope. In

normal operation, the peak-and-hold circuitry is set to the "Peak Detect mode", and then the analog output shows the ADC signal (energy information) during the read out cycle.

Figure 2-24 shows a block diagram of detector instrumentation based on the RENA-3 ASIC. A detailed presentation of the hardware realization of the setup is given in Chapter 3.

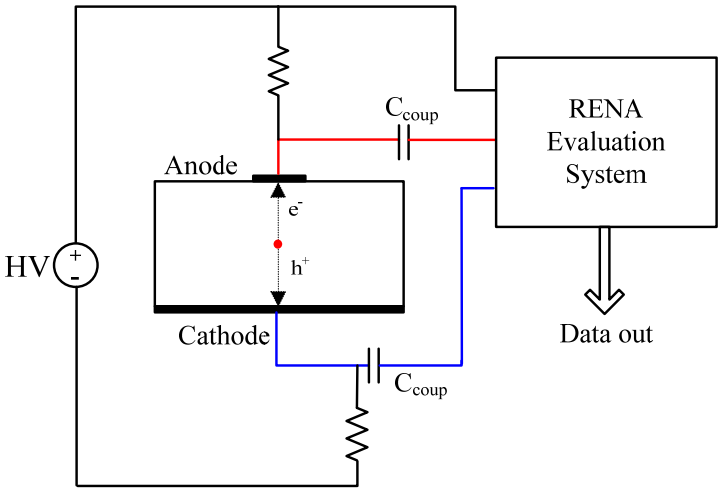

Figure 2-24, Detector instrumentation using the RENA-3 ASIC.

Chapter 3

CZT DETECTOR IN PET IMAGING

In this chapter, we describe our CZT-based PET prototype. Several experimental setups were designed to evaluate the prototype's performance, including energy resolution and coincidence time resolution. The detector configurations will be described in section 3.1. In sections 3.2 and 3.3, the experimental setup and measurement, and calibrations are described respectively.

3.1. Detector Configuration

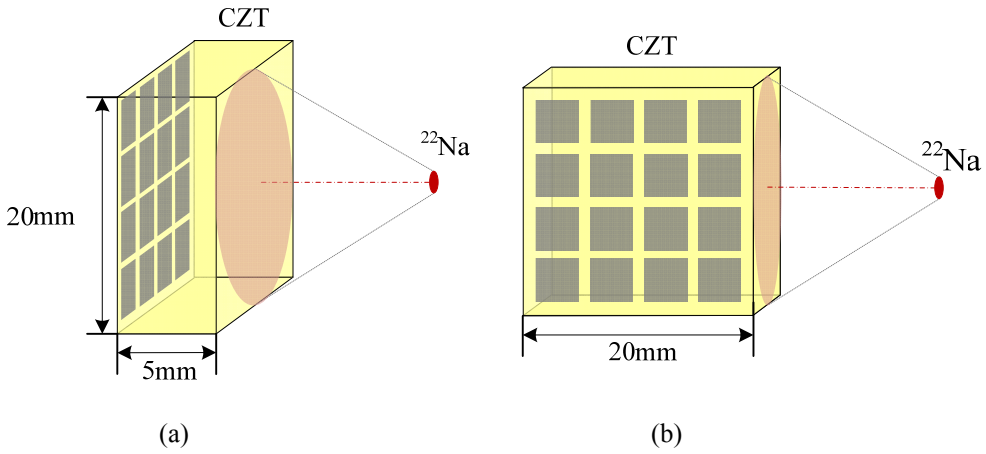

Figure 3-1, PET system is built with different detector configuration. (a) PPF and (b) PTF

As described in Chapter 1, in this study, a PET system is realized by stacking CZT detector arrays in two different geometries. One geometry is planar parallel field (PPF), in what the bias electric field is parallel to the direction of irradiation. Another geometry is planar transverse field (PTF), where the bias electric field is perpendicular to the direction of irradiation. Figure 3-1 illustrates two types of CZT

detectors operating in different configurations [114]. The optimum configuration type depends on the specific application and on which characteristic is most important: detection efficiency, spatial resolution, energy resolution or time resolution. In practice, the larger detector thickness results in a higher DoI parallax error. However, due to the deep penetration of 511 keV photons, the detectors must be sufficiently thick to maintain a high effective photon detection efficiency. Based on such a trade-off, the detector thickness was selected to be 5mm in our experiments.

From Figure 3-1, we can see that for same CZT detector (20 mm × 20mm × 5 mm), it demonstrates high absorption efficiency due to a large effective thickness of 20 mm in PTF compared to 5 mm in PPF structure. In order to meet the required detection efficiency, different thickness can be chosen without modifying the interelectrode distance and thus the charge collection properties of the detectors. Therefore, sufficient detection efficiency can be obtained by PTF, which is suitable for measurements of high energy gamma rays. However, the full absorption percentage is decreasing with the penetration depth [115]–[117].

In contrast to PTF, the PPF structure has a more uniform response and detected counts for all pixel anodes. In addition, it can minimize hole-trapping probability by irradiating from the cathode side. At the same time, thanks to the unchanged small drift length for the electrons and single polarity charge sensing, there is no significant degradation of energy resolution between PPF and PTF structure.

For time resolution evaluation, the center pixel is chosen rather than edge pixels because of the better energy resolution performance from the preliminary results due to the imperfect material (section 3.2). Therefore, PPF structure is chosen rather PTF structure due to the larger effective counts and therefore the shorter sampling time.

3.2. Anode Energy Resolution Characterization

3.2.1. Experiment Setup

CZT's superior energy resolution was verified for the specific combination of 1) large volume CZT, 2) pixelated electrode pattern, and 3) peak-detecting amplitude readout by the RENA-3 ASIC.

First, the linearity and uniformity of the RENA-3 evaluation system are tested before the detector is connected by using internal test pulse generator. The test pulses have fast rising edges and relatively long widths. That simulates the anode charge signals of typical solid-state detectors when applied to the coupling capacitors at the RENA-3 test inputs. The nominal amplitude range is equivalent to the charge range of 0 to 37.5 fC.

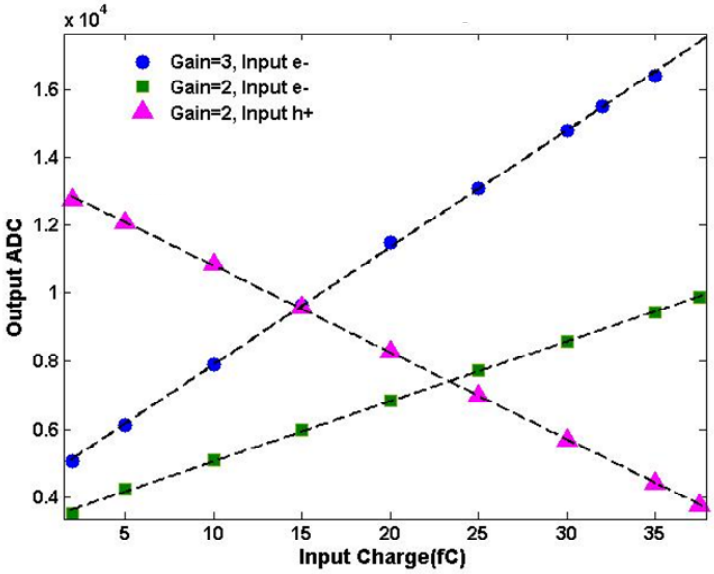

Figure 3-2, Linearity test of the RENA evaluation system.

The outputs of test pulses with negative polarity (electron) and positive polarity (holes) are shown in Figure 3-2. We observed that, 1) the RENA evaluation system has excellent linearity over whole test charge range (0~37.5 fC); 2) according to the binary data file format of RENA-3 evaluation system, bits [29-16] are ADC values, therefore the maximum value of ordinate is 16384 (2^{14}).

^{22}Na source embedded in an acrylic disk is used in our research as the gamma ray emitter, which decays to ^{22}Ne via positron emission with a branching ratio of 90.2%, followed by the emission of a 1.27 MeV gamma photon. The induced charge generated by a 511 keV incident photon without any loss is estimated by equation (3-1)

$$Q_e = qN \approx 1.6\times10^{-19} \times \frac{511keV}{5eV} \approx 16\,fC \qquad (3\text{-}1)$$

In order to avoid saturating, the ADC output for input photons with higher energy (~40fC due to 1274 keV photopeak of ^{22}Na estimated by equation (3-1)), the gain of preamplifier should be set to 2.

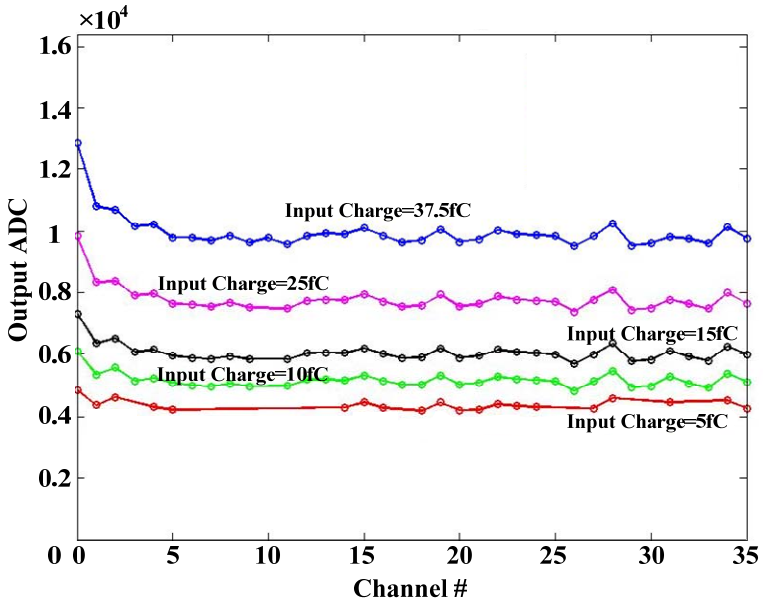

Figure 3-3, The uniformity of RENA evaluation system (Gain=2, Input: negative polarity)

One RENA ASIC chip can process 36 channels simultaneously. The uniformity of the channels' responses under test pulses with different amplitude is given in Figure 3-3. The response of each channel is consistent over the whole input charge range (0~37.5 fC). The maximum difference between all channels for the same amount of input charge is ~7.5%, which can be eliminated by converting the ADC value to deposited energy.

The pixelated CZT detector contained 64 (8×8 array) anode pixels and one planar cathode which are to be read out. Figure 3-4 shows the connection between RENA evaluation system and CZT detector through the intermediary PCBs. Therefore, the functions of the intermediary PCBs are: 1) providing connections for HV bias and AC coupling, and 2) facilitating multiplexing between the CZT module array and the RENA evaluation system. Biasing is done as shown in Figure 2-24, where the anodes and cathode are biased at ground and negative HV through R_b= 10 MΩ resistors, respectively. AC coupling is necessary because each RENA-3 ASIC input can tolerate only up to 5 nA of DC leakage current. However, for our photon detector

design, we have large leakage currents on the cathode channels due to large size, and on the anode channels due to contributions from cathode.

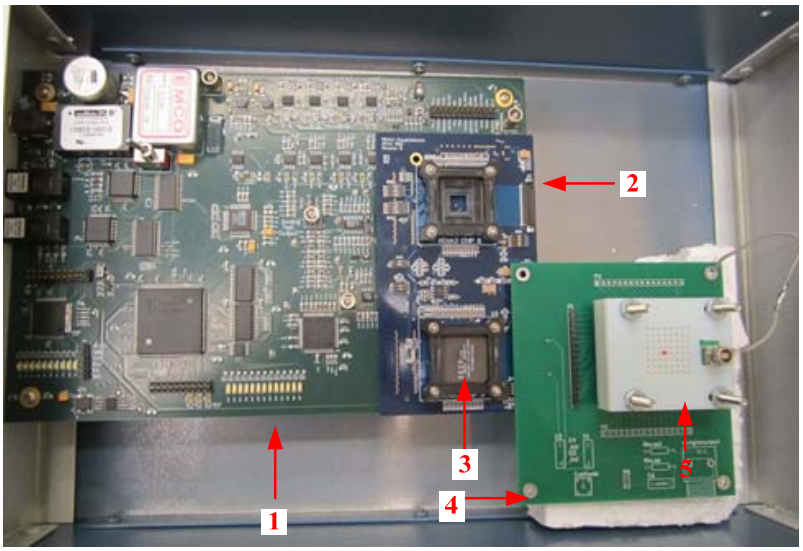

Figure 3-4, The connection between RENA evaluation system and CZT detector. (1) Main board. (2) Daughter board. (3) RENA-3 ASIC chip. (4) custom-designed intermediate PCB. (5) Packaged CZT detector.

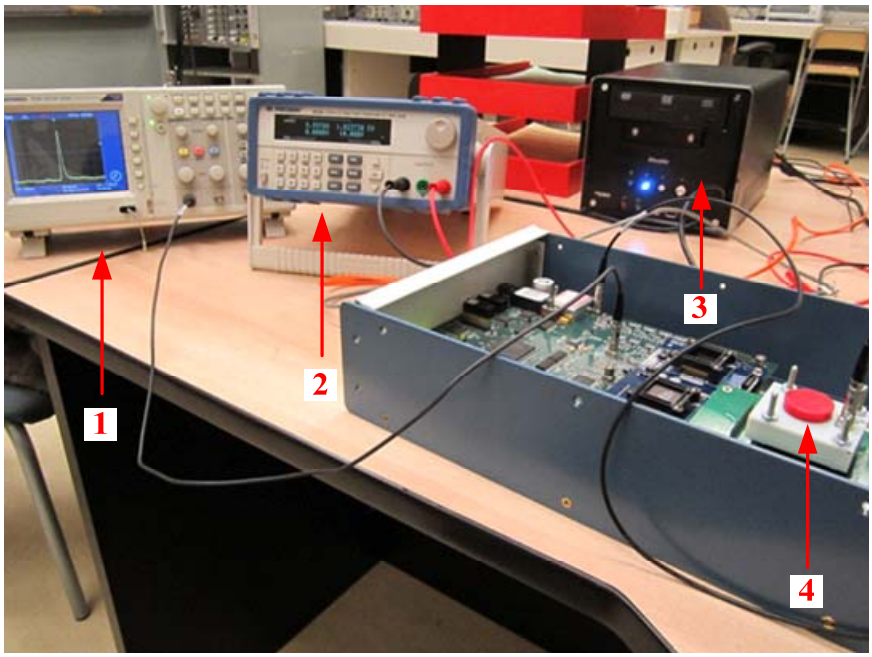

Figure 3-5, The experiment setup for energy resolution and detector uniformity investigations. (1) Oscilloscope. (2) DC voltage supply (10V/2A). (3) Controlling PC connected through optical fiber. (4) Face-irradiated ^{22}Na sealed source.

The whole experiment setup for energy resolution and detector uniformity investigations is illustrated in Figure 3-5. An oscilloscope is used to monitor the analog output from the shaping circuit. The control PC is connected with the RENA evaluation system by an optical fiber, and all parameters can be modified through the graphical user interface (GUI). The detector's cathode face is irradiated by a point source as shown in Figure 3-1. When testing the energy resolution of a single channel, each anode channel is enabled and triggered in turn by setting to "SPARSE" pattern. The bias voltage of 400V was chosen as a trade-off between the detector leakage current and the signals rise times. The optimal shaping time is chosen as 1.9 μs.

3.2.2. Experimental Results

First, the conversion of the digitized signal amplitude in ADC units to the corresponding keV value was performed as described in section 2.3.4 of Chapter 2. ^{22}Na and ^{137}Cs (photopeak at 662 keV) radiation sources are used here. Two sources are needed because the 0 value in ADC units does not correspond to 0 keV. Then, the FWHM energy resolutions were measured by fitting the Gaussian curve of equation (1-3) to the photopeak in energy spectrum, with the coefficient σ being the fitted parameter. As stated in section 1.1.3 of Chapter 1, the FWHM of the photopeak is simply 2.355σ.

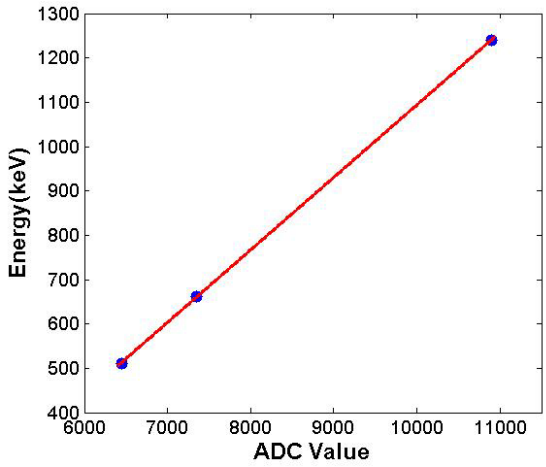

Figure 3-6, ADC output to energy input of tested anode channel.

A linear mapping in Figure 3-6 was obtained by identifying the spectral features of both ^{22}Na and ^{137}Cs. The linear polynomial in equation (3-2) is used to fit it.

$$y_E = a_1 \times x_{ADC} + a_2 \tag{3-2}$$

The two parameters a_1 and a_2 are obtained as ~0.15 and ~500, which vary slightly from anode to anode. Then the relationship between the energy resolutions in ADC value and actual deposited energy is

$$\begin{aligned} Energy\ resolution &= 2.355 \times \frac{\sigma}{E_{photopeak}} \\ &= 2.355 \times \frac{a_1 \times \sigma_{ADC}}{a_1 \times E_{ADC} + a_2} = 2.355 \times \frac{\sigma_{ADC}}{E_{ADC} + a_2 / a_1} \end{aligned} \tag{3-3}$$

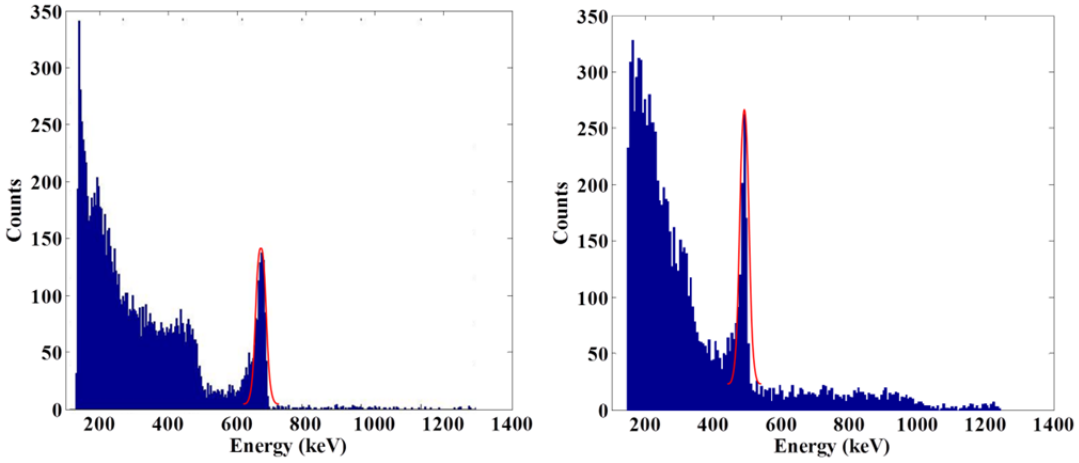

(a) (b)

Figure 3-7, Raw energy spectrum of single anode near the detector center for uncollimated (a) ^{137}Cs (b) ^{22}Na photon sources irradiating the cathode side.

An example energy spectrum for a single anode-single cathode photon interactions obtained from the built system is shown in Figure 3-7. Before any calibrations, the raw energy resolutions at 511 keV and 662 keV are calculated as 3.71±0.35% and 3.5±0.94%, respectively. The error bar corresponds to the 95% confidence interval of the fitted parameters. The photopeak and the Compton edge are easily recognizable. Below the peak, there is a significant low energy tail. And the photopeak broadening as described in section 1.1.3 is visible.

The same setup and measurements are repeated with the 64 anode pixels for this specific detector, and the results are shown in Figure 3-8. Comparing with the center anode pixels, the edge anode pixels, especially corner anode pixels have worse performance, which may be caused by the non-uniform material, connection or electronics variations. The average energy resolution is 6.8%.

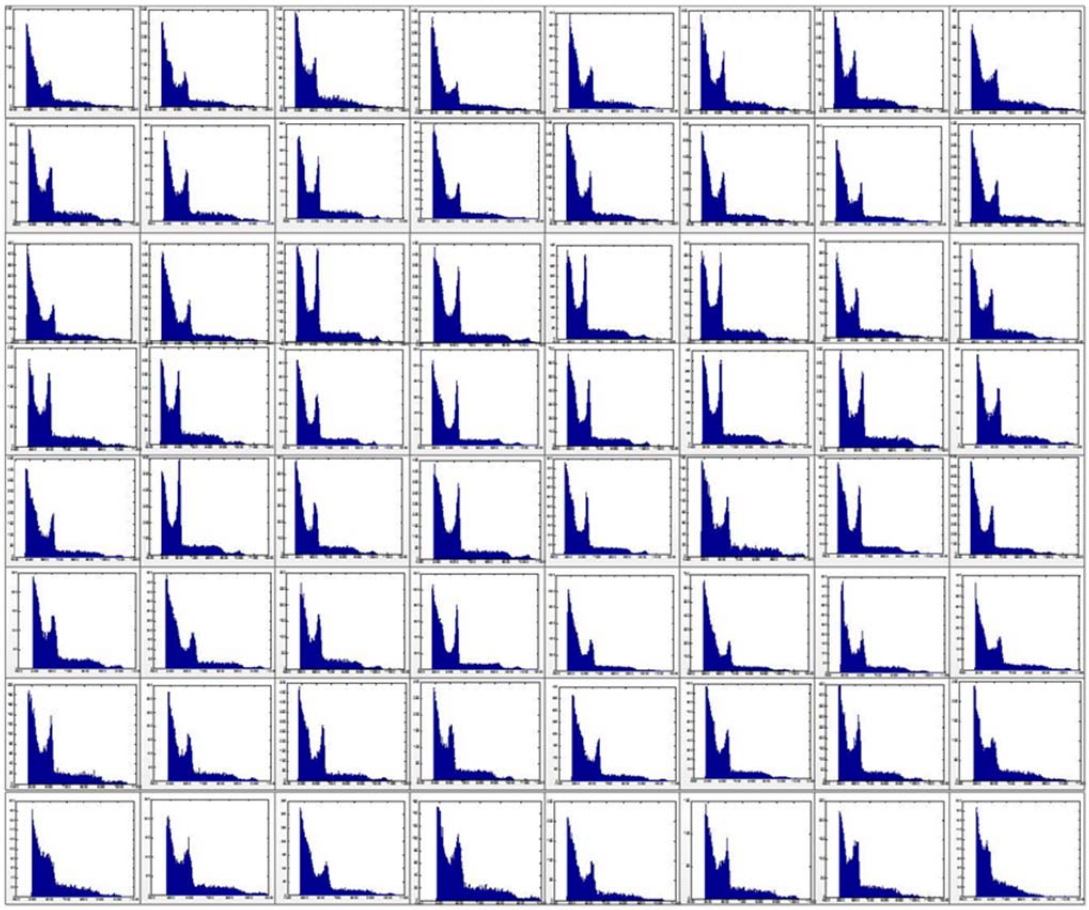

Figure 3-8, The spectra map of all anodes (8×8 pixel array) obtained from built system for an uncollimated ^{22}Na photon source irradiating the cathode side.

3.2.3. Improving Energy Resolution by Depth Sensing

For a given energy source, a typical energy spectrum recorded by a detector has a large low-energy tail. Anode versus C/A ratio and cathode versus C/A ratio of single-pixel events are shown in the scatter plots of Figure 3-9 (a) and (b), respectively. ^{137}Cs source is used in this section because of the single photopeak, which would not be corrupted by scattered events from the higher energy photopeak. First, at the 662keV energy level, the anode signal amplitude (Figure 3-9 (a)) shows slight dependence on the C/A ratio rather than a constant for events at different DoIs across the 5mm thick CZT detector. Second, in contrast to the anode signal amplitude, cathode signal amplitude (Figure 3-9 (b)) is a strong function of C/A ratio with good linearity, except at the regions very close to the anode or cathode surfaces. Third, high energy photons have greater penetration and can interact with the CZT detector

substrate at a greater depth. These events are subject to more hole trapping effect, and hence smaller C/A ratio. Therefore, most of photopeak events are with the C/A ratio less than 1.

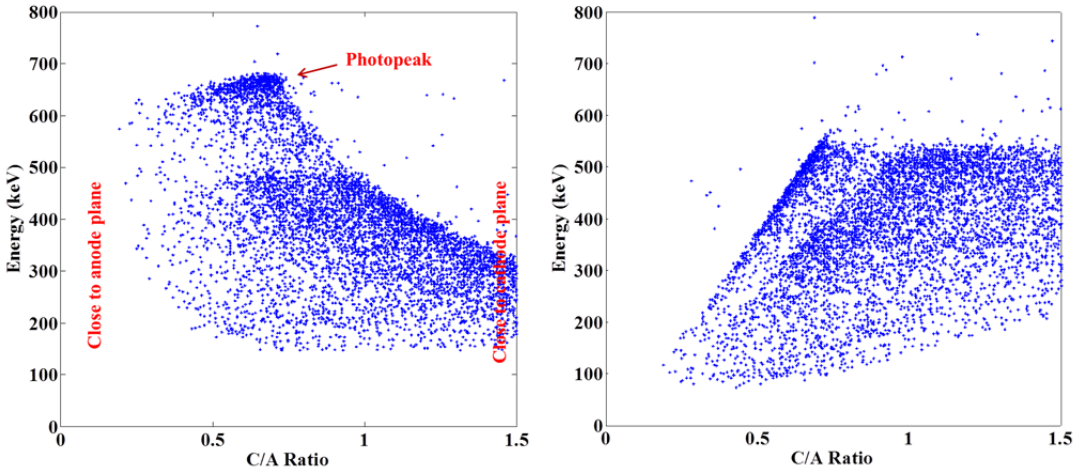

(a) (b)

Figure 3-9, Single-pixel signal of (a) anode versus C/A ratio and (b) cathode versus C/A ratio (^{137}Cs source).

In Figure 3-9, the pulse height deficit of anode across the detector thickness is caused by two factors. The first factor is the weighting potential variation of the collecting pixel. The second factor is electron trapping. An event near the cathode experiences the minimum deficit due to weighting potential, but experiences the maximum effect of electron trapping because the electron cloud has to travel the entire thickness of the detector. Events closer to the anode experience less electron trapping. However, the weighting potential changes rapidly in this region.

A high energy signal corresponds to interactions near the cathode, whereas a low energy signal corresponds to interactions near the anode. This suggests that our pixelated detector is subject to charge trapping and weighting potential variation. The low energy tail in the energy spectrum decreases as a/L ratio decreases, because small pixel effect helps mitigate the weighting potential variation. But this implies that many more pixels are to be read out electronically. Furthermore, charge sharing due to charge carrier diffusion and escaping characteristic X-rays become significant. Therefore, the depth information is used to correct the pulse height to reduce the low energy tail.

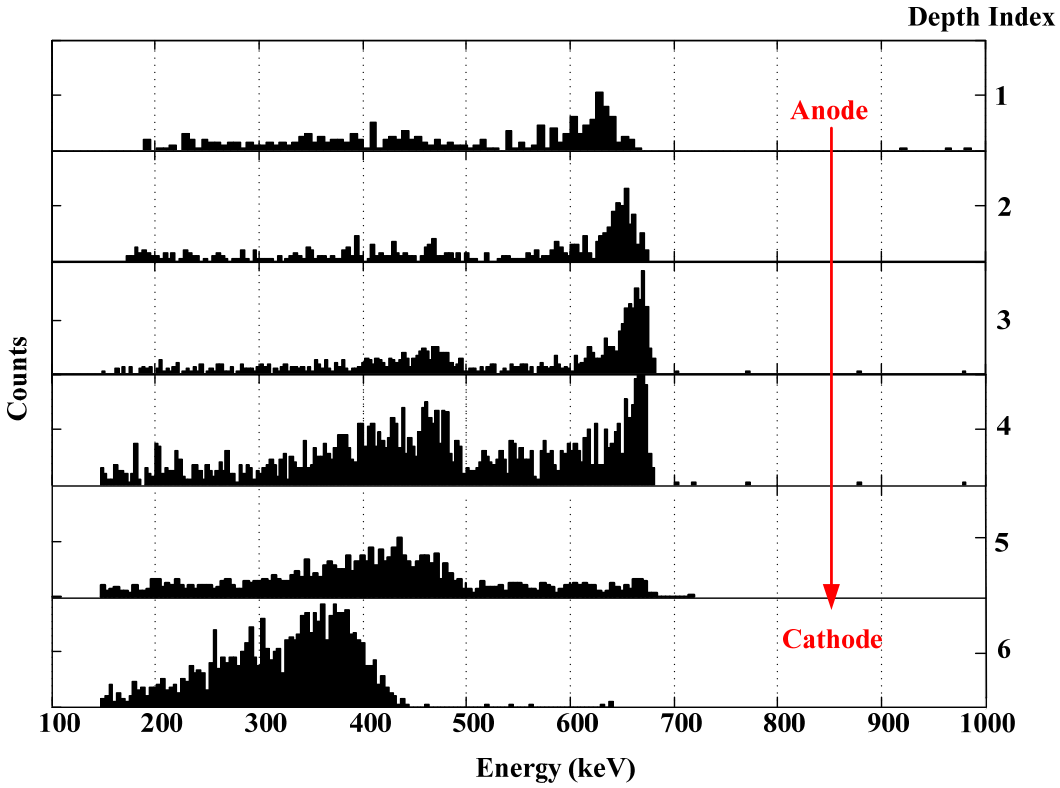

Figure 3-10, Single-pixel events spectra sorted into different C/A ratio depth indexes

Calibration of the photopeak position as a function of depth of interaction for each pixel is the most critical step in achieving excellent energy resolution in a large volume pixelated semiconductor. Based on results above, the correction is required because CZT detectors have a depth dependent response due to the weighting potential and trapping as well as position sensitive response due to material non-uniformity. The basic principle is to divide a detector into a large number of voxels for independent calibration. First, the detector is conceptually divided into slices of depth layers. Second, single-pixel events collected from a ^{137}Cs source are recorded into the corresponding sub-spectrum in each layer. The example depth-separated spectra for one anode pixel are shown in Figure 3-10. The whole detector thickness is divided to 6 depth layers. Third, the photopeak's centroid is determined for each depth layer and used as the depth calibration coefficient $C(n)$ in equation (3-4). We know that these photopeaks are from single gamma ray energy (662 keV). Thus, the relative position of these photopeaks is used as the calibration data to correct for the effects described above and align to the same position.

$$E(n) = \frac{S_a(n)}{C(n)} \times E_0 \tag{3-4}$$

In equation (3-4), $C(n)$ is the depth calibration coefficient of pixel n, E_0 is the calibration source energy, i.e. 662keV here and E is the calculated energy for the corresponding anode signal S_a.

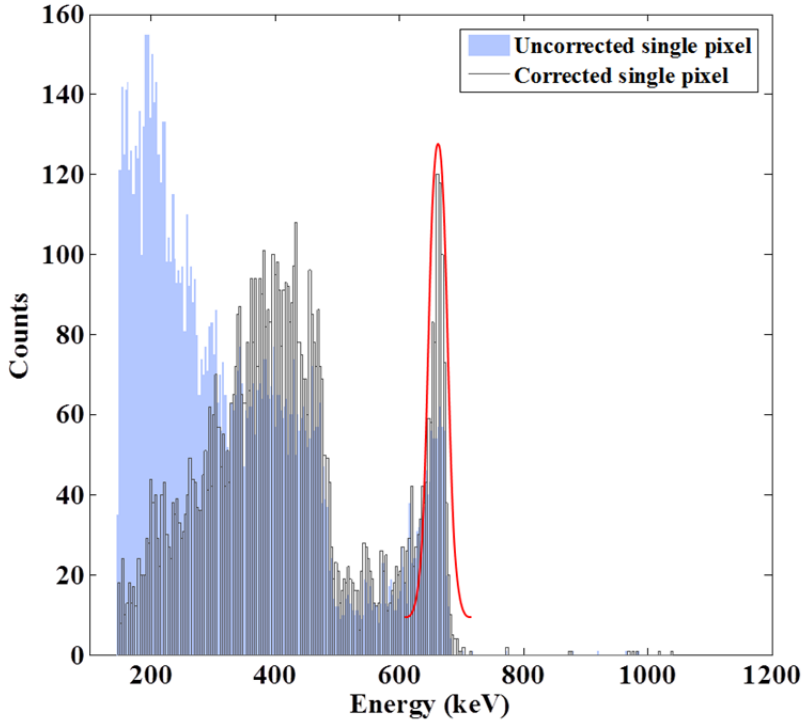

Figure 3-11, The energy spectrum before and after depth calibration with the help of the C/A ratio.

In Figure 3-11, the energy spectra before and after calibration of the anode signal with the help of the C/A ratio, are shown. The energy resolutions are 3.5±0.94% and 2.26±0.84% before and after DoI correction, respectively. This verifies that good energy resolution can be achieved by our prototype. However, the measured energy resolution is still about an order of magnitude below the theoretical limit. The possible reasons are pulse peak sampling (instead of a free running ADC) and the presence of a large input capacitance (~100pF) due to the long traces and PCBs.

From the discussion in Chapter 2, we know that either the C/A ratio or the electron drift time can be used to derive the depth calibration coefficients for single-pixel events. However, due to the limited timing resolution, the depth calibration coefficients derived from the electron drift time are worse than those derived from the

C/A ratio and consequently result in poorer energy resolution. So, the C/A ratio and the depth calibration coefficients derived from the C/A ratio are used here for single-pixel events.

3.3. Coincidence Timing Performance

Good coincidence time resolution is another critical requirement for the CZT detector if they are used in PET applications. This permits a narrow time window to be set and, therefore, true coincidence events could be well distinguished from the random coincidence events which cause degradation in image quality. Several groups have been involved in research on semiconductor-based PET imaging systems for many years. Experiments were conducted with custom detectors, and ten to a few tens of nanoseconds FWHM time resolution were obtained [118]–[123].

The timing performance of CZT is limited by variations in the shape of the signals and also the electronic noise [124]. The "small pixel effect" delays the rising edge of the anode signals from where the gamma-ray interaction occurred. Besides these factors, the starting points also vary with the DoI, causing uncertainty in coincidence time measurement, particularly for thick detectors. Therefore, the time resolution may be improved by analysis of the pulse shape, which can be done efficiently with digital waveform sampling.

Both anode signal and cathode signal are used to extract timing information in [118]–[123]. In principle, the time estimated from the cathode signal can provide a more accurate gamma interaction time [121]. As shown in Figure 2-11, the cathode signal rises slowly with a relatively long time. Its signal amplitude depends not only on the energy deposited, but also on the DoI. A linear fitting method is used for single-interaction cathode signals. The start and stop time of the cathode rising signal are found by extrapolating the fit line back to the baseline and tail estimates. This method can be done only for the relatively large cathode signals to obtain the correct detection time, because a relatively smaller slope and amplitude would cause a lower fitting accuracy.

In contrast, the amplitude of the anode signal is almost independent of the DoI (except in the small region near the anode plane), and it depends only on the energy deposited. The anode signal also rises steeply with a short rise time that provides high

precision in estimating the timing of the signal. For these reasons, the anode signal is preferable for detecting the event timing if the electron drift time (or DoI) can be corrected.

3.3.1. Experiment Setup

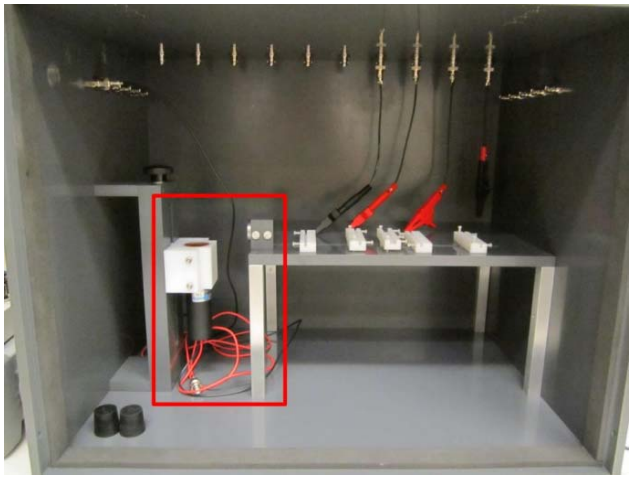

Figure 3-12, Light tight enclosure for scintillation detector experiments. BNC connectors are used to transmit signal and power across the box. The white stages are made of Delrin and aligned along the track in the platform, as is the adjustable PMT holder (red box).

All the experiments described in this section were performed inside a custom built light-tight enclosure. Since the timing performance of the LYSO-PMT detector is significantly better than that of the CZT detector, a fast PMT (R10560, Hamamatsu Photonics K.K) is used as the reference detector. A 3×3×20 mm^3 LYSO crystal is wrapped in Teflon tape and coupled to the PMT using BC-630 optical grease (Saint-Gobain Ceramics & Plastics, Inc.), which has a refractive index of 1.465. This treatment reduces the amount of refraction and reflection that would occur at the crystal-air interface. In Figure 3-12, the PMT holder, which is adjustable in vertical position to facilitate better alignment of coincidence detection experiments, is shown.

A schematic of the coincidence timing experiment schematic is shown in Figure 3-13. The signals from the CZT detector directly after pre-amplification and the PMT outputs were digitized simultaneously using a fast Tektronix oscilloscope (MSO3034 mixed signal oscilloscope). This method was chosen instead of the time-amplitude converter (TAC) NIM-based setup due to the low coincidence rate results from the small anode pixel size of the CZT detector. In addition, digital signal processing

offers the advantage of a very fine control over the analysis parameters to obtain better time resolution. The oscilloscope is capable of sampling at 2.5 GHz with 8-bit precision, and it is triggered by the CZT signals. Following the Nyquist sampling theory, the sampling interval and record length are respectively set to 0.4ns and 1000 due to the fast rising edge of the signal from the LYSO-PMT detector. For each individual radiation interaction that occurs in the detector, there is a set of discrete digital pulse waveforms to be collected including from the single anode and cathode of the CZT detector, and the PMT. More than 150000 sets of pulses are accumulated in the storage memory of the oscilloscope. Then, the digitized pulses are transferred to a PC for offline analysis using a MATLAB program.

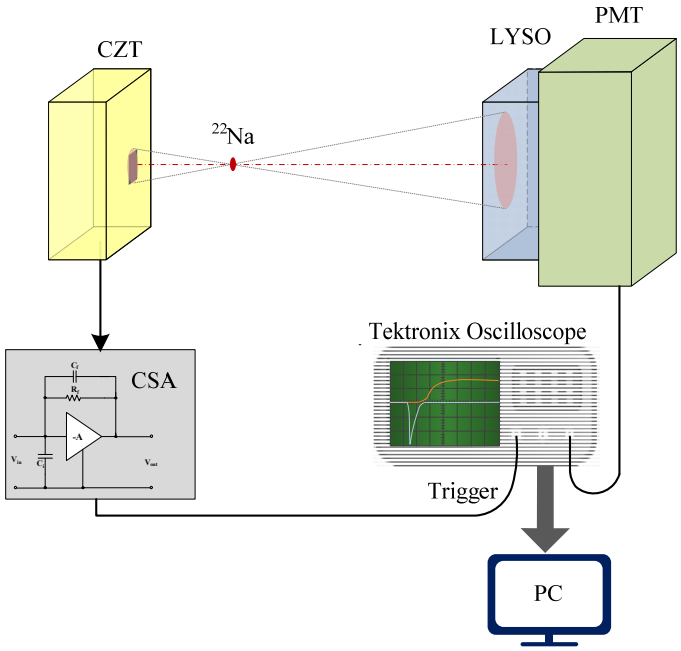

Figure 3-13, The schematic of coincidence timing experiment.

Because the anode pixel of the CZT detector is smaller than scintillator crystal, a ^{22}Na source is placed between the two detectors at distances that are 5 cm from CZT detector and 50 cm from the LYSO crystal to increase the detection efficiency of coincidence events. The CZT detector is operated at a bias voltage of 400 V at first. The measurements are performed at room temperature.

For the central anode pixel and cathode readout, two fast discrete charge sensitive amplifier models (Ortec 142A) are connected to detector by BNC cables. They are

placed as close as possible to each CZT detector to reduce noise. These charge amplifiers can provide the high charge sensitivity of 20mV/MeV with a fast rise-time of 5~12 ns. Therefore, the signal amplitudes are in the range of 0~20mV with a ^{22}Na source. The CZT detector and amplifiers are placed in an aluminum box to minimize electromagnetic interference.

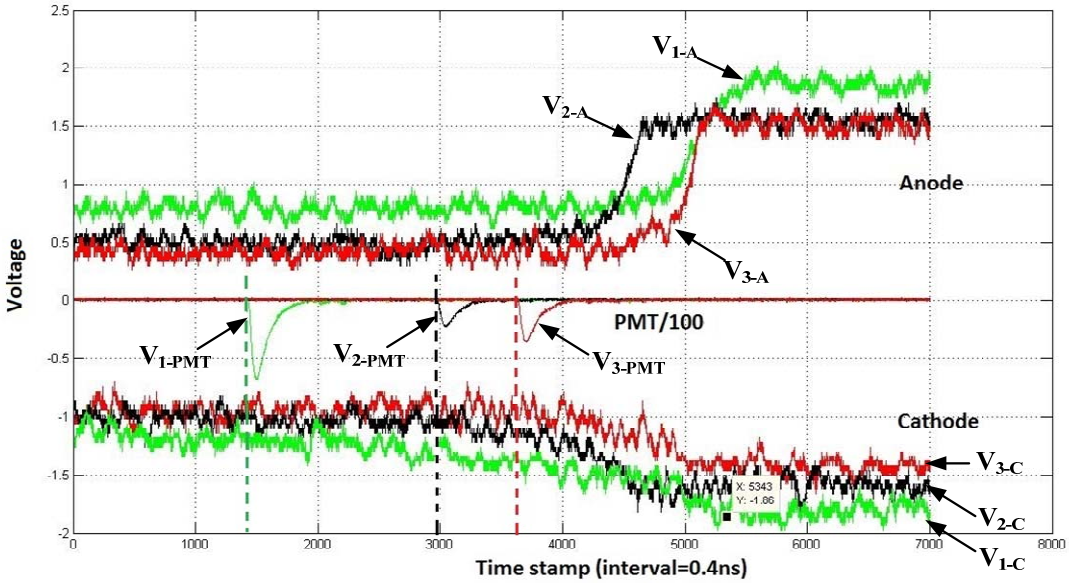

Figure 3-14, Pulse outputs from PMT and CZT detector.

The examples of three as-acquired (raw) pulse sets are shown in Figure 3-14. The amplitude of PMT signals is reduced 100 times to clearly demonstrate the comparisons with arrival times of recorded events sampled by CZT. Comparing with V_2- and V_3- signal sets, there is a longer delay between the interaction time of recorded PMT and CZT signals in V_1-set. Because fixed distances are set between the PMT, source and CZT detector in the experiment, this set was preliminarily excluded of true coincidence events pair. In addition, cathode signals tend to trigger more instantaneously than anode after a photon interaction, as shown previously in Figure 2-12. The interaction timing is determined by finding the tuning point of signals. Thus, the following work include 1) correcting raw pulses for drifting baseline and electronic (white) noise; 2) applying proper energy window and timing window to reject scatter and random events; and 3) extracting amplitude and interaction time as accurately as possible.

3.3.2. Digital Pulse Processing

Because of the different expected signal shapes of the three categories of signals: pixel that collect charge, the cathode and PMT waveform, customized waveform processing algorithms are used for each category. There are currently several steps in the pre-shaping processing for signals of CZT: baseline restoration and noise filtering. These processing must be applied to all signals in a waveform set on an event-by-event basis to obtain the correct energy information. In this context the baseline value of a preamplifier will be defined as the average recorded amplitude when no charge is collected. In an ideal system, each preamplifier will have a constant baseline value regardless of time, temperature, or other operating conditions.

To obtain the energy and time information accurately, the raw signals are processed by several steps. First, the waveform is checked for the presence of a non-noise event by calculating the difference of maximum and minimum values of the signal. If it is greater than 5 mV (photopeak events having amplitude of order ~10 mV), only then it was stored for subsequent processing. Second, we filter these stored pulses by a low pass filter. A simple moving average filter (MAF) is adopted for this task due to its simplicity and fast computational speed. The MAF smoothens the signals by replacing each data point with the average of a specified number of neighboring data points. The degree of smoothening is determined by the number of points involved in the averaging process. Here, a 20-point moving average filter is applied to the anode and cathode signals to remove the high frequency noise. Third, the baseline of each signal is corrected by subtracting the average of ~100 points prior to the trigger level from the entire signal. Fourth, the amplitude of the signal, which reflects the energy deposition of the gamma ray, is determined by taking the average of points around maximum value (~100 points) of the signal stream. Finally, the histogram of the signal amplitudes is obtained for energy gating.

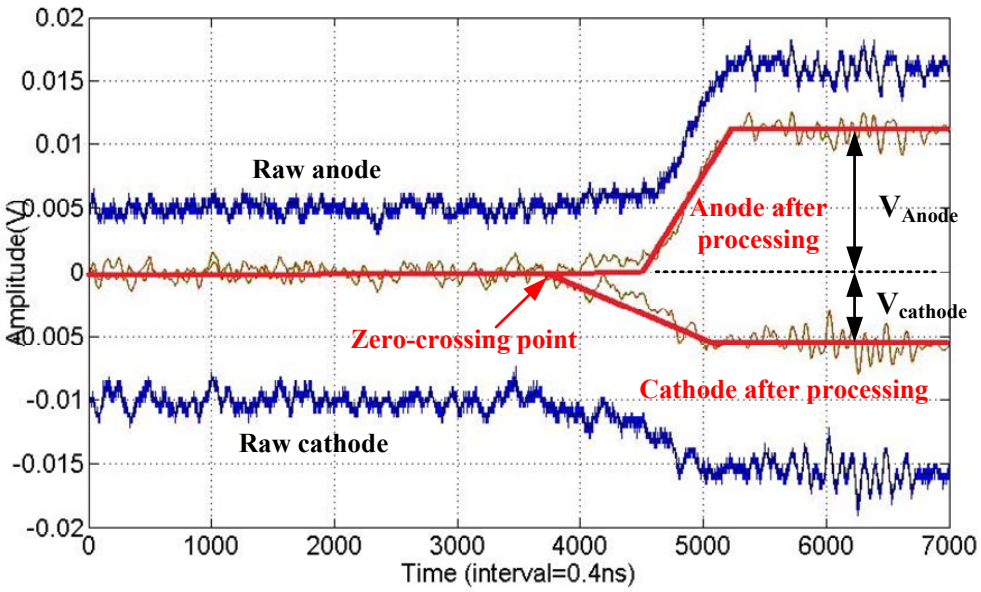

Figure 3-15, The waveforms measured before and after the digital pulse processing.

Figure 3-15 displays the waveforms measured for a typical event, as well as the results after digital pulse processing. The blue lines are raw signals, and the red lines are processed signals. A linear fit is applied to the cathode waveform in the region between 20% and 80% of the cathode signal maximum. The zero-crossing point of the line fitted to the cathode signal was considered as the detection time of the event.

If the original signal has a fast rise time, a slight smoothening would be sufficient to obtain a sharp timing signal. If the signal is inherently slow, larger smoothening should be applied to obtain a timing signal with amplitude well above the noise level. Otherwise, the time pickoff would be corrupted by the electronic noise which degrades the timing performance. It should be noticed that a large smoothening of the fast signal can also degrade the rise time of the signal. Therefore, bearing in mind that signals from CZT detectors have different levels of contribution from electron and holes, the proper selection of the MAF would be time consuming. In order to select the proper value of this filter, the filtering process is repeated multiple times to reach the best time resolution.

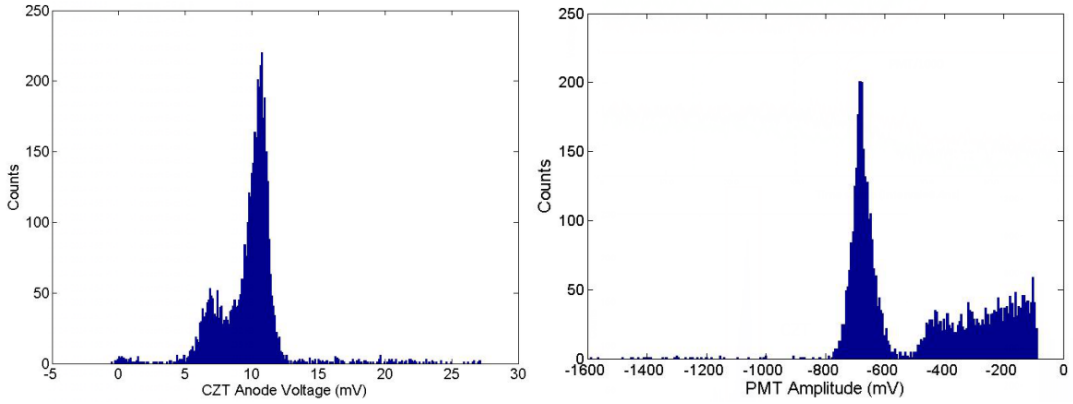

(a) (b)

Figure 3-16, The energy spectra of (a) CZT detector and (b) PMT.

The energy spectra of a ^{22}Na source, measured with the CZT detector and the PMT, are shown in Figure 3-16 (a) and (b), respectively. The 511 keV energy line is clearly visible. Due to the oscilloscope limited resolution, the 1274 keV energy line of ^{22}Na is not displayed in oscilloscope screen and thus not stored for later processing.

Typically, energy spectra are presented by energy values on the *x*-axis. First, a quite linear detector response is obtained between the bins of the histogram and measured energy value from the previous chapter. Second, in this section the obtained energy spectra are only used to set the energy gating to reject the scatter events. Therefore, the calibration was deemed unnecessary here. Based on these energy spectra, the photon interactions analyzed are energy-gated around the photopeak ± 4% energy window.

3.3.3. Electron Drift Time Calibration

The differences of the arrival times of pulses from both detectors are plotted as a histogram in equation (3-5)

$$\Delta t = t_{PMT} - t_{CZT\_anode}. \tag{3-5}$$

Due to the negligible contribution of the scintillator detector to the time spectrum (~1 ns FWHM), the FWHM of the time spectrum is considered to be the time resolution of the CZT detector. The constant fraction discrimination (CFD) method is used with the CZT detector, and was set with 23 ns CFD delay and 0.24 attenuation factor, according to the minimum time difference. With regard to the scintillator, the arrival time is determined by direct application of a simple leading edge discrimination

method to the PMT signals. There are no undesirable characteristics of variation in PMT's pulse shape and therefore no shaping is done.

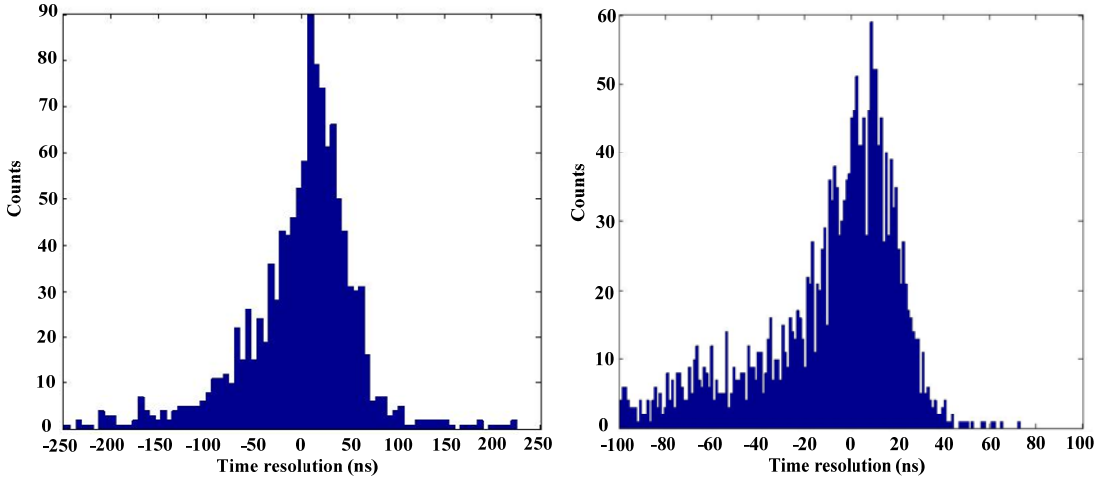

(a) (b)

Figure 3-17, CZT anode-PMT time difference histogram at bias is of (a) 400V (b) 500V.

The low mobility μ of charge carriers results in long rising edge of anode signal and more trapping effects. The noise due to trapping effects, in turn, limits the achievable SNR of the preamplifier signal. Therefore, it is difficult to achieve a good time resolution by triggering on such signals. One of ways to improve the time resolution is to increase bias voltage, i.e. higher electrical field intensity and faster rising edge. In addition, the enhanced small pixel effect also causes the rising edge of the anode signal to be steeper. Both of them would cause reduced sensitivity to time walk and time jitter. Figure 3-17 shows the CZT anode-PMT time difference histograms at bias voltages of 400 V and 500V. The spectra represent the time resolution of 60±4 ns and 36±6 ns FWHM. The spectrum has an asymmetric shape, which is attributed to the slow rise-time events.

Another reason for poor time resolution is that interactions at different depths would cause different electron drift time to the anode, as shown in Figure 2-10. For detector with thickness of 5mm, the largest electron drift time estimated under 500V bias voltage as shown in equation (3-6) to be

$$T_e = \frac{L}{\mu_e E} = \frac{5mm}{1350\times10^{-3}\left(m^2/Vs\right)\left(500V/5mm\right)} \approx 368ns. \qquad (3\text{-}6)$$

This effect results in significant time walk, which must be compensated. The electron drift time can be estimated from the cathode pulse ($t_{CZT\_cathode}$) and should be subtracted from the timing estimated by anode signal (t_{CZT_anode}) to give the calibrated time of the detection Δt, as shown in equation (3-7)

$$\Delta t = t_{PMT} - (t_{CZT\_anode} - t_{CZT\_cathode}) \tag{3-7}$$

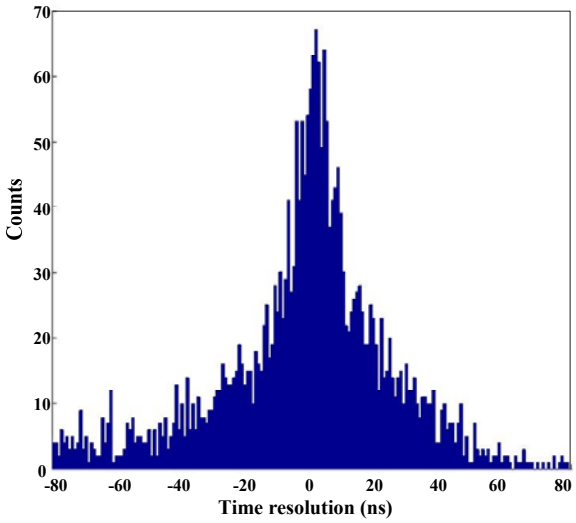

Figure 3-18, Calibrated CZT anode-PMT time difference histogram at a bias of 500V.

The result is shown in Figure 3-18. The spectrum represents a time resolution of 19±3 ns FWHM. We can see that the time resolution values are about an order of magnitude worse than scintillation crystal-based photon detectors. First, in semiconductor photon detectors, the electrode sensitivity to charge carriers is spatially varying. Second, given that CZT detector signals depend on charge transport, they are produced with higher temporal variance compared to the propagation and collection of scintillation light [125], which results in more timing jitter and time walk. Third, the ^{22}Na source is not a pure positron emitter, so the photopeak may include the possible confounding scattered events result from 1274 keV gamma rays. Furthermore, the low SNR of the CZT signal output from the preamplifier affects the accuracy of timing pickup. Summing over a few pixels overcomes the problem that a different slope will be obtained (in the pulse shape) due to different charges collected. Unfortunately, adding more pixels will introduce more noise to the total signal. According to the equations (2-13) and (3-6), the depth resolution under 500V bias voltage for a 5mm thick CZT detector is calculated to be ~0.89mm.

3.4. Summary

In this chapter, we have successfully designed, built and tested a prototype of a PET imaging system based on a CZT detector. For research purposes, the raw pulse signals are stored and processed offline to implement depth sensing and optimization of post-processing algorithms, although it will result in larger volume of data and longer processing times. The prototype achieved a depth calibrated energy resolution of 2.26±0.84% for single anode events, and a time resolution of 19±3 ns after electron drift time calibration. Based on these results, a depth resolution of ~0.89mm was achieved. Together with the 2D position sensing capability associated with the pixelated anode array, this prototype demonstrates the capability to provide the 3D position information of gamma-ray interactions in the detector, which can also aid in minimizing the parallax error in PET imaging.

Chapter 4

IMPROVING THE SPATIAL RESOLUTION IN CZT DETECTORS[‡]

There are two common configurations of CZT detector designs: pixelated configuration and cross-strip configuration shown in Figure 4-1. For the pixelated configuration, only the anode comprises of an array of small electrodes. For the cross-strip configuration, two sets of strip electrodes are formed on the anode and cathode orthogonally to help reduce the number of readout channels (i.e., from N^2 down to 2N). As we know, the spatial resolution is currently limited by the electrode pitch in a CZT detector. It has great potential to achieve high spatial resolution through the use of closely spaced electrodes on the anode/cathode sides, a relatively straightforward process as compared to cutting and assembling scintillation crystal elements. However, this leads to higher fabrication cost and a larger number of readout channels. In addition, inter-electrode charge spreading can negate any improvement in spatial resolution.

In this chapter, we will investigate how to achieve sub-pitch spatial resolution in CZT detectors using two methods: charge sharing effect and transient signal analysis. Then, effects of design parameters on achievable sub-pitch spatial resolution will be studied, including electrode geometry, DoI, lateral position, bias voltage and detector SNR. In addition, the valid range of two methods will be defined and calculated.

[‡] Part of this work was published as: X. Zheng, Z. Cheng, M. J. Deen and H. Peng, "Improving the spatial resolution in CZT detectors using charge sharing effect and transient signal analysis: simulation study," Nuclear Instruments and Methods in Physics Research Section A. vol. 808, no. 1, pp 60-70, February 2016.

Finally, the implementation of these two methods in both pixelated and cross-strip configuration of CZT detectors will be discussed.

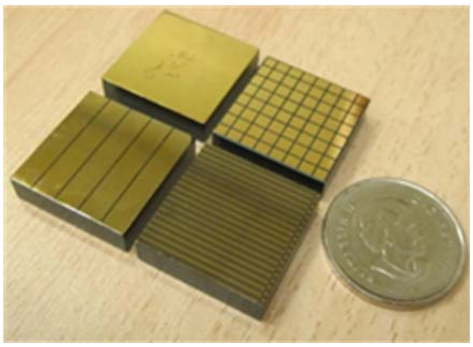

Figure 4-1, Two common configurations of electrodes in CZT detectors (detector dimension: $20\times20\times5mm^3$). Top two figures are pixelated detector, and bottom two figures are cross-strip detector.

4.1. Background of Spatial Resolution Improvements

As shown in Figure 4-2(a), the charge sharing effect arises when a 511 keV gamma ray hits the detector near the edges of the electrodes or within the gap in-between two electrodes. The dashed vertical lines represent the electric field, while the contour lines represent the weighting potential of a single electrode. Charge sharing effect becomes more noticeable when the size of electrodes/gaps decreases. If not accounted for properly, charge sharing would degrade a number of performance parameters including detection efficiency, energy resolution, as well as spatial resolution [126]. On the other hand, charge sharing effect can be utilized to help achieve sub-pitch spatial resolution as the electrode pitch is comparable to the size of an electron cloud [127].

One recent study [128] reports that for a CZT detector of 250 μm pitch and 1 mm thickness, the percentage of incoming events involving charge sharing amounts up to 36.4% under ^{241}Am gamma ray (59.5 keV) irradiation. With a charge sharing addition (CSA) algorithm applied (i.e., the energy deposited in each electrode is summed and the event is assigned to the single pixel of the largest signal), the detection efficiency increases from 63% up to 93%. For spatial resolution, the feasibility of achieving sub-pitch resolution based upon the ratio of output signals of two adjacent electrodes was studied in [129]. For a CZT detector (250 μm pitch) and incoming X-rays (40 keV), an effective range, where the charge sharing effect can be observed, is found to be 80-

180 μm. Furthermore, charge sharing effect has been investigated when the electrode pitch is much larger than the size of the electron cloud. For example, with cross-strip electrodes of 3-5 mm pitch, sub-pitch resolution of good linearity can be achieved over a region which extends ~1 mm from the edge of an electrode into the gap [130]. This study also suggests that positioning uncertainty depends on three factors: electrode pitch, gap and detector SNR.

Besides the charge sharing effect, transient signal analysis has been studied for CZT detectors [131], [132], especially when a relatively large electrode pitch (compared to the electron cloud) is present. Under this condition, the induced transient signal of a neighboring non-collecting electrode changes as a function of the cloud's lateral position, which can subsequently be utilized to achieve sub-pitch resolution [133]. Essentially, the positioning is linked to the crosstalk of the weighting potential distributions of two different electrodes (see more details in section 2.3). As shown in Figure 4-2(b), even when the electron cloud is eventually collected by only a single electrode, the neighboring electrodes still produce transient signals. For example, for incoming gamma rays of 662 keV energy (with a collimator of 100 μm opening) and a 2.0×2.0×1.5 cm^3 pixelated CZT detector (pitch: 1.72 mm) [134], [135], the spatial resolution can be improved down to 230 μm. However, for the transient signal analysis method, one serious challenge is that the transient signals suffer from poor SNR as a result of weak coupling between the electron cloud and the weighting potential of non-collecting electrodes. This would consequently limit the positioning accuracy of CZT detectors [136].

In spite of potential benefits discussed above, both the charge sharing and the transient signal analysis methods face two limitations. First, both methods can be used when there is only a single interaction within the detector. It should be pointed out that for other applications such as a Compton camera, if multiple interactions are separated by several (more than 2) pixels, sub-pitch resolution could still be obtained for each individual interaction based on either transient signal analysis or charge sharing. However, such scenario was not included in the study described in this chapter. Second, the transient signal analysis relies on the assumption that the induced signal on each pixel depends primarily on the distribution of the weighting potential.

When an interaction occurs either very close to the edge of electrodes, or within the gap between two electrodes, charge loss and charge sharing would become dominant. As a result, the transient signal analysis cannot be applied.

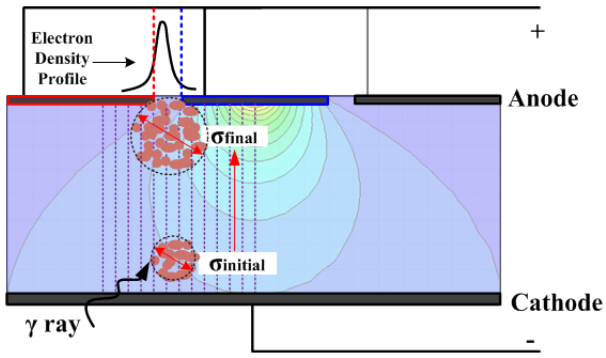

(a)

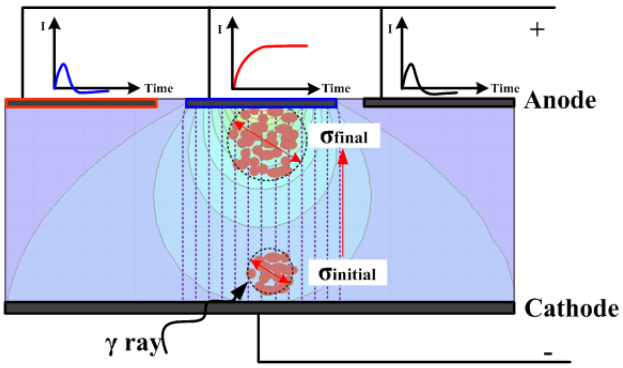

(b)

Figure 4-2, Illustration of (a) charge sharing effect and (b) transient signal analysis.

To our knowledge, there is no previous work aiming to investigate how one can achieve sub-pitch resolution in CZT detectors using both methods, particularly for PET imaging applications. The valid ranges for both methods also need to be investigated. In addition, it is important to understand how the ranges are affected by different detector design parameters, such as the geometry (electrode and gap), applied bias voltage and SNR. In this chapter these issues are studied.

4.2. Charge Sharing Effect

4.2.1. Valid Range of Charge Sharing Effect

Here, we describe the study of the transport of an electron cloud in an internal electric field. We also derivate the valid range of the charge sharing effect (VR_{CSE}),

over which sub-pitch spatial resolution can be achieved. Once electron-hole pairs are created to form a cloud, they will travel along the internal electric field until they finally reach the anode/cathode terminals. The spatial distribution of the electron cloud is approximated by a convolution of its initial distribution (from simulation in Chapter 2) and a diffusion process governed by Fick's law [137]. Only the lateral diffusion (i.e., planes parallel to the cathode/anode) was modeled. For an initial electron cloud of a delta-function distribution (zero width), its broadening characterized by a standard deviation σ (assuming a Gaussian shape) after time *t* is [137]:

$$\sigma^2 = 2Dt; \quad D = (kT/q)\mu \tag{4-1}$$

where *D* is the diffusion coefficient of electrons for CZT detectors, *k* is Boltzmann's constant, *T* is absolute temperature and *q* is the elementary charge. At room temperature, *D* is 34 cm^2/s with the electron mobility μ of 1350 $cm^2/(Vs)$. When a uniform internal electric field is present, equation (4-1) can be rewritten as:

$$t = d/v = dL/\mu V; \quad \sigma^2 = \frac{2kTdL}{qV} = \left(\frac{2kTL}{qV}\right)d \tag{4-2}$$

where *L* is the thickness of the detector, *V* is the bias voltage, *d* is the distance from the initial location after diffusion for time *t*, and *v* is the instantaneous velocity of the electrons/holes. The broadening increases with *d*, which is related to DoI.

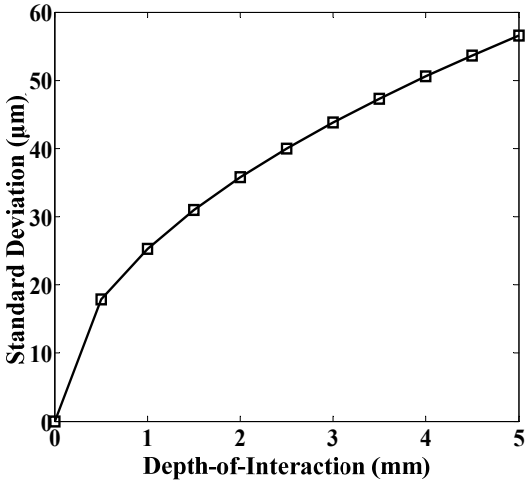

Figure 4-3, The broadening of the electron cloud as a function of interaction depth.

The broadening of an electron cloud as a function of DoI is illustrated in Figure 4-6. This broadening is due to the diffusion within the internal electric field. The bias voltage is set to 400V. For a cloud starting with a delta-function distribution, its size (standard deviation σ in equation (4-1)) increases linearly with DoI. The maximum value of σ is ~56.6 μm, and this was obtained when the electron cloud was generated very close to the cathode (DoI = 5 mm). As implied by equation (4-2), either a longer travel distance or a longer travel time yields more noticeable broadening.

Between the cathode and anode, the concentration of electron clouds is not uniform. For the initial concentration $M_0\delta(x_0,0)$, which is a delta function distribution at x_0, the one dimensional solution for concentration $M(x,t)$ at the position x and the time t is given by

$$M(x,t) = \frac{M_0}{2(\pi Dt)^{1/2}} \exp\left(\frac{-(x-x_0)^2}{4Dt} \right) \tag{4-3}$$

where x is the location along the direction parallel to the anode/cathode planes, and x_0 is the location of initial interaction. The total amount of induced charge on a single electrode can be analytically derived using equation (4-4) below by integrating over space:

$$\frac{M(t_{Drift})}{M_0} = \frac{1}{2(\pi Dt)^{1/2}} \int_{x_0-\sigma/2}^{x_0+\sigma/2} \exp\left(\frac{-(x-x_0)^2}{4Dt} \right) dx > Noise_{th} \tag{4-4}$$

Here, the signals over three regions were studied: the left electrode (I_1), gap area (I_2) and right electrode (I_3). I_2 characterizes the charge loss within the gap (i.e., charge collection efficiency less than 100%). VR_{CSE} represents the range over which both I_1 and I_3 are above the selected noise threshold $Noise_{th}$, which is the triggering level in the readout electronics. In practice, when $Noise_{th}$ is set too low, a PET system will process a large number of low energy events and suffer from the dead time effect. For the opposite condition, when $Noise_{th}$ is set too high, VR_{CSE} will be reduced and the collection efficiency will be degraded. Based on such a trade-off, $Noise_{th}$ was selected to be 10% of the amplitude of the 511 keV photopeak in our simulation.

For illustration purposes, two electron cloud profiles with charge sharing involved are illustrated in Figure 4-4 (a), for two DoIs (1 mm and 5 mm, bias voltage: 400 V).

The centroid of the electron cloud is located at 50 μm on the horizontal axis. The behavior of signal intensities (I_1, I_2 and I_3) after normalization in three regions (the left electrode, gap and right electrode) is shown in Figure 4-4 (b), with a collimated 511 keV beam shifting from the left to the right side (gap width: 100 μm) and no electronic noise included. A number of important trends are summarized below. First, I_1 gradually decreases from 1 to 0 while I_3 gradually increases from 0 to 1 at the same time. Second, (I_1+I_3) demonstrates an initial decrease from unity down to 58% followed by a recovery back to unity, due to charge loss within the gap. The lowest amplitude is observed at the very center of the gap (x=0). It should be pointed out that for a cross-strip configuration, such charge loss will be effectively eliminated due to the inclusion of steering electrodes.

The dependence of VR_{CSE} on gap width and DoI is illustrated in Figure 4-4 (c), with a bias voltage of 400 V. First, a linear relationship exists between VR_{CSE} and DoI for all gap widths. With a gap width of 100 μm, VR_{CSE} increases from ~73.6 μm (DoI=0 mm) up to ~112.3 μm (DoI=5 mm). This is due to the diffusion process that is described in equation (4-2). If the interaction occurs near the cathode (a larger DoI), a longer travel distance would produce more noticeable broadening, which is more likely to benefit from charge sharing to achieve sub-pitch resolution. Second, it is also observed that VR_{CSE} depends on gap width. As the gap width gets smaller, the effect of charge sharing becomes more significant. For example, at a DoI of 5 mm, the range is ~ 72.3 μm and ~210.4 μm for the gap width of 150 μm and 10 μm, respectively. With a gap width of 10 μm, VR_{CSE} increases from ~150 μm at DoI=0 mm up to ~200 μm at DoI=5 mm.

The dependence of VR_{CSE} on voltage bias and DoI (constant gap width: 100 μm) is presented in Figure 4-4 (d). At a DoI of 1 mm, VR_{CSE} is ~81.2 μm and ~63.6 μm, for a bias of 200 V and 800 V, respectively. While at a DoI of 5 mm, VR_{CSE} increases up to ~153.3 μm and ~82.9 μm, for a bias of 200 V and 800 V, respectively. This indicates that increasing the bias voltage would negate the benefits of charge sharing. Furthermore, as the DoI increases from 1 mm to 5 mm, the difference among the four biases becomes much more significant. In other words, VR_{CSE} exhibits a stronger dependence on bias voltage compared to that on gap width.

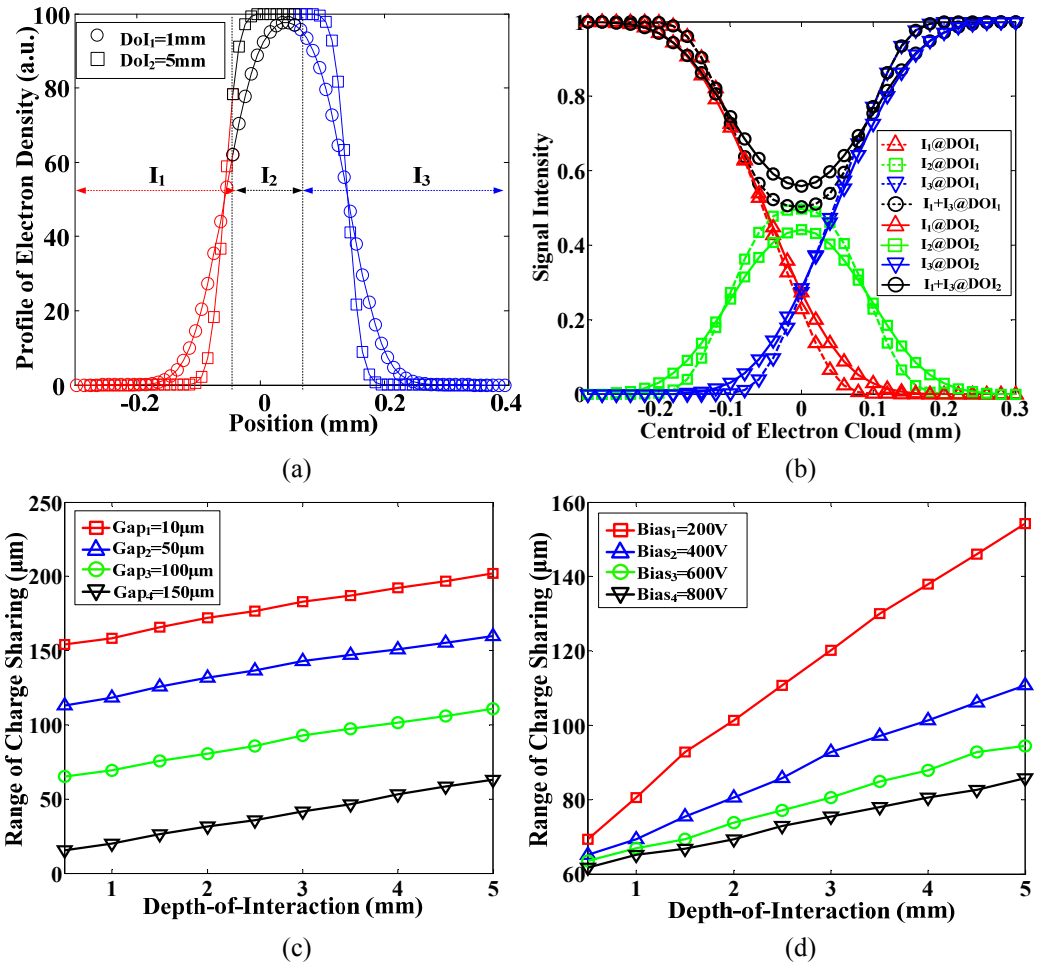

Figure 4-4, (a) Illustration of the profiles of the electron clouds at two different depths (the centroid of the cloud: 50 μm) (b). Signal intensity $I_1/I_2/I_3$ for two DoIs. (c) VR_{CSE} as a function of gap size and DoI (Bias voltage is kept constant at 400V). (d) VR_{CSE} as a function of detector bias and DoI (Gap width is kept constant at 100 μm). A DoI of 1 mm corresponds to a depth of 1 mm distance from the anode. The triggering threshold was set to be 10% of the amplitude of the full 511 keV energy peak.

4.2.2. Probability of Charge Sharing Event

The proportion of charge sharing events for a given electrode configuration was estimated using equation (4-5). Under uniform irradiation of 511 keV gamma rays, the proportion of charge sharing events, also known as the ratio of the inter pixel area to the total area (dotted line in Figure 4-5), is given by [138]:

$$Area\_Ratio = 1 - \left(\frac{a - g + 2c - S_{final}}{a} \right)^2 = 1 - \left(\frac{1.1(a-g) - \sqrt{S_{ini}^2 + (2.3\sigma)^2}}{a} \right)^2 \quad (4\text{-}5)$$

$$S_{final} = \sqrt{S_{ini}^2 + S_{diff}^2} = \sqrt{S_{ini}^2 + (2.3\sigma)^2}$$

where g is the gap between electrodes, a is the electrode pitch and c is the collection width. S_{diff} is the size of the electron cloud after the diffusion process (i.e., 2.3σ). S_{ini} is the initial could size obtained from Monte-Carlo simulations. S_{final} represents the overall distribution by adding the S_{ini} and S_{diff} in quadrature. It should be emphasized that the estimation here is valid only for single interactions within the detector. Moreover, for the cross-strip configuration shown in Figure 4-1(a), the anode electrodes are interleaved with the steering electrodes to enhance charge collection. In that case, the charge sharing effect can be applied on the cathode side and the estimation of the probability for charging sharing is similar to equation (4-5), except that the calculation needs to be made along one dimension only.

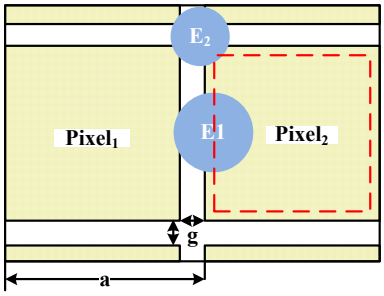

Figure 4-5, Probability calculation of charge sharing events in a pixelated detector. E_1 and E_2 are example events with different energy, which could cause the charge sharing effect.

4.2.3. Sub-pitch Spatial Resolution Achievement

When a 511 keV gamma ray hits the detector at different lateral positions, the relative amplitude of the output signals of two adjacent electrodes will vary. This can be exploited to achieve sub-pitch resolution and more precise positioning over VR_{CSE}, as illustrated in Figure 4-2. Based upon equation (4-4), the distribution of the charge cloud depends on a number of parameters: bias voltage, DoI, noise threshold and electrode geometry (pitches and gap width). All these parameters were included in our modeling. The quantitative relationship between lateral positions was studied using two figures-of-merit (FoMs) as defined in equation (4-6):

$$Sr_1 = I_3 - I_1; \quad Sr_2 = \frac{I_3 - I_1}{I_3 + I_1} \tag{4-6}$$

Both Sr_1 and Sr_2 exhibit a linear relationship with the lateral position as shown in Figure 4-6 (the center of the gap: 0 mm). Such linear relationship between the beam

position and two FoMs can be utilized to achieve sub-pitch spatial resolution. VR_{CSE} for Sr_1 is approximately between -0.15 mm and 0.15 mm. The transition for Sr_2 is slightly steeper than that for Sr_1, and extends over a smaller VR_{CSE} (from -0.1 mm to 0.1 mm).

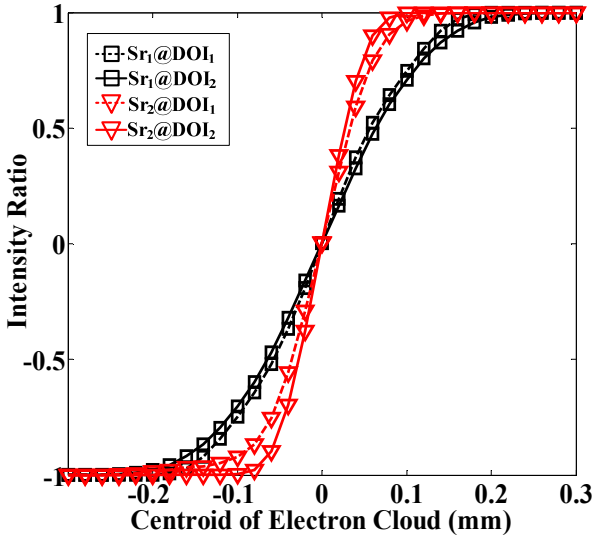

Figure 4-6, Two intensity ratios Sr_1 and Sr_2 as a function of lateral position

4.3. Transient Signal Analysis

4.3.1. Transient Signal of Neighboring Electrodes

When an electron cloud is collected by an anode electrode, transient signals will also be produced on two neighboring electrodes (left-side and right-side). These transient signals result from crosstalk of the weighting potential. However, the amplitude of transient signal on a non-collecting electrode is much less (i.e., by a factor of ~10 or more) than that of the collecting electrode, due to weak coupling between the cloud and the non-collecting electrodes. One important assumption when using the transient signal analysis method is that the electron cloud must be fully collected by the collecting electrode. In other words, it cannot be applied to those interactions that occur either near the edges of electrodes or occur within gap, the regions where the charge sharing effect would dominate.

A number of parameters were studied, including the lateral position of interactions, DoI, and gap width. For simplification, the electron cloud was modeled using a "single point model" rather than an extended one of Gaussian shape in

equation (4-3). A collimated 511 keV source was shifted from the left edge to the center of the collecting electrode, represented by three points (P_1, P_2 and P_3) in Figure 4-7 (a). Two DoIs (2 mm and 4 mm) and three gap widths (150 μm, 100 μm, and 50 μm) were studied. For illustration purpose, an example of transient signals (waveforms after normalization) of two neighboring anodes and the cathode is included in Figure 4-7 (b). The 511 keV gamma rays hit the CZT detector close to the centerline of a single anode (DoI=4 mm) and therefore there was no charge sharing involved. It is observed that the induced charge on the collecting anode reaches unity, while the induced charge on the cathode reaches ~0.8. With respect to the transient signal on $anode_2$, it has a maximum amplitude of ~0.2, much lower compared to that of the collecting anode ($anode_1$). With regard to waveform shape for $anode_2$, the transient signal first rises as the electron cloud travels towards the anode, but subsequently drops back towards zero or even negative when the cloud gets very close to the collecting anode. The transient signal reaches a maximum value when the weighting potential line becomes tangential to the trajectory of electrons. Once the interaction is very close to the anode, a negative tail would occur and the amplitude of such a tail depends on the DoI.

The transient signals of the left non-collecting anode are shown in Figure 4-7 (c), for three lateral positions (P_1, P_2 and P_3) and two DoIs (2 mm and 4 mm). Two important features are observed. First, for a given DoI, the peak amplitude is sensitive to lateral positions and it decreases as the interaction moves from P_1 to P_3. The opposite trend is observed for the right non-collecting electrode (not shown). Taking DoI_1 (2 mm) for example, the normalized peak amplitude (i.e., maximum value) is ~0.182, ~0.096 and ~0.067 for P_1, P_2 and P_3, respectively. Second, for a given lateral position, the peak-tail amplitude (i.e., difference between maximum and minimum amplitudes) is found to be independent of DoI. For both DoIs, the peak-tail amplitude is ~0.40, ~0.30 and ~0.24 for P_1, P_2 and P_3, respectively. Moreover, the amplitude of the negative baseline is found to be lower at DoI_1 than that at DoI_2, because DoI_1 is closer to the anode side.

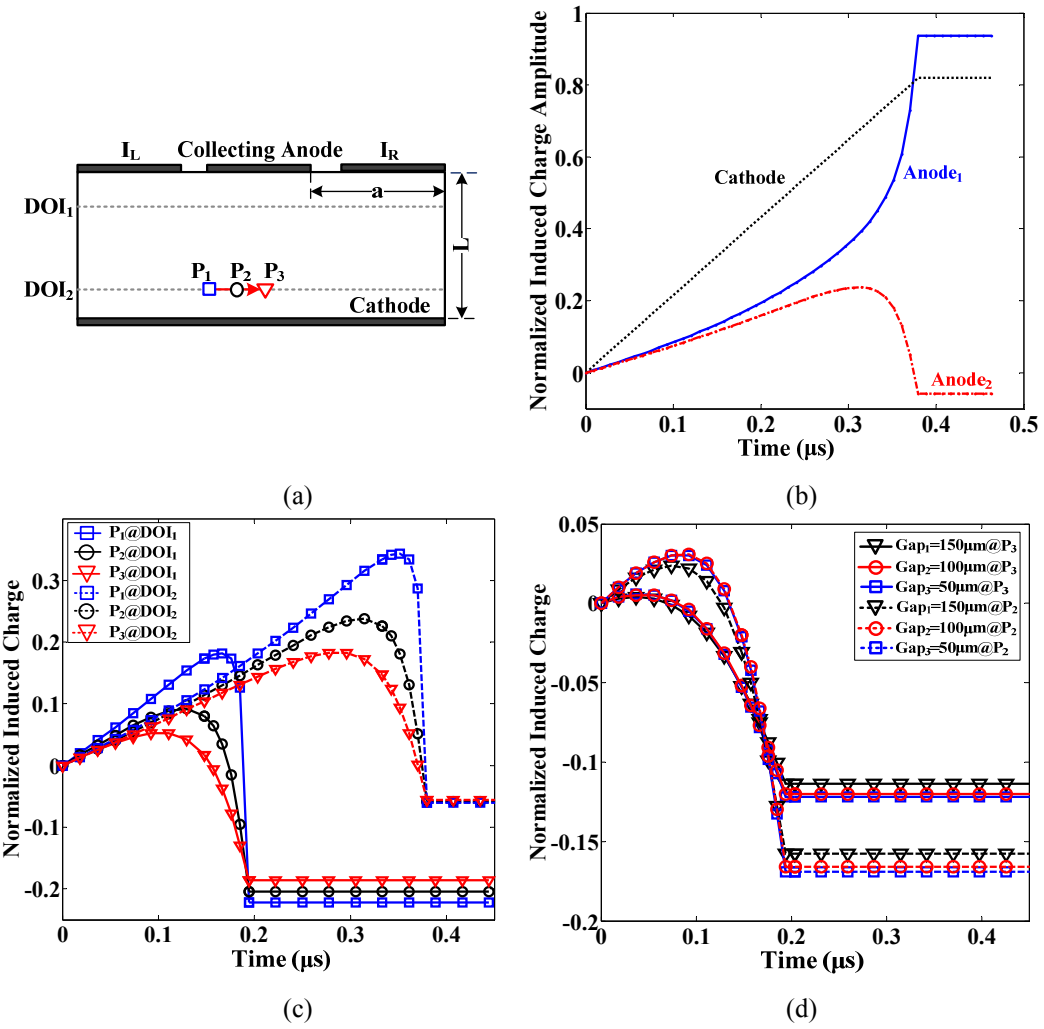

Figure 4-7, (a) Analytical modeling of induced charge as a function of detector parameters and multiple DoIs. (b) The waveforms of the cathode, the collecting anode and one neighboring non-collecting anode. (c) Transient signals at three positions (P_1, P_2 and P_3) for two DoIs (2 mm and 4 mm). (d) Transient signals as a function of gap width (Electrode size is kept constant at 2.4mm).

The transient signals of the left non-collecting anode for three gap widths (150 μm, 100 μm and 50 μm) are shown in Figure 4-7 (d). The size of electrodes on the anode side was kept constant at 2.4 mm. To avoid cluttering the graph, only the results of two lateral positions P_2 and P_3 (DoI_1 = 2 mm) are presented. First, for a given gap width of 50 μm, the peak-tail amplitude of P_3 (~0.115) is found to be smaller than P_2 (~0.185), due to a weaker coupling between the electron cloud with the weighting potential. Second, no significant difference in transient signals is found among three gap widths. This is due to the fact that the difference among three gap widths is 50-100 μm along the lateral direction, much smaller than the size of the electrode (2.4

mm). As a result, the distribution of the weighting potential and the amplitude of transient signals would not change significantly as gap width varies.

4.3.2. Sub-pitch Spatial Resolution Achievement

The relative amplitudes of the transient signals on the two non-collecting electrodes can be used to achieve sub-pitch spatial resolution, as shown in equation. (4-7):

$$Sr_1 = I_R - I_L; \quad Sr_2 = \frac{I_R - I_L}{I_R + I_L} \tag{4-7}$$

where I_R and I_L are signals of the left-side and right-side electrodes. The valid range of transient signal analysis (VR_{TSA}) represents the range over which the following two conditions are met: 1) the signal of the collecting electrode is within the selected energy window; and 2) a linear relationship exists between the two FoMs in equation (4-7) and the lateral position.

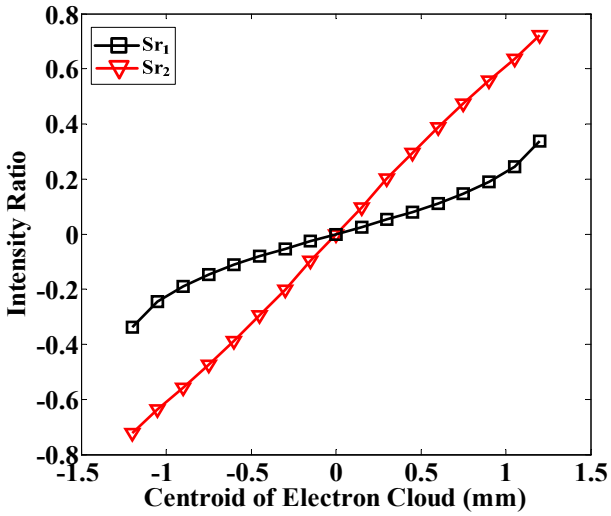

Figure 4-8, Two intensity ratios Sr_1 and Sr_2 as a function of lateral position.

Two FoMs, Sr_1 and Sr_2 defined in equation (4-7), are plotted in Figure 4-8 as a function of the centroid of the electron cloud. Both FoMs demonstrate a linear dependence on the lateral position over the range between -1.2 mm and 1.2 mm (electrode size: 2.4 mm, center of the electrode: 0 mm). Sr_2 has a slightly steeper transition compared to Sr_1. Two clarifications should be made here in comparison with the charge sharing method. First, VR_{TSA} is defined at the middle of the collecting electrode, instead of at the middle of the gap for the charge sharing method. Second

(not shown here), the results of both Sr_1 and Sr_2 are found to be the same between 2 mm and 4 mm cases, implying that no DoI correction is required in the use of the transient signal analysis method.

4.4. SNR modeling

To study the quantitative relationship between sub-pitch resolution and detector SNR, a simplified noise model was used in our work. The detector SNR is defined as the ratio between the amplitude of the 511 keV photopeak and the standard deviation of the noise floor. For a given SNR, the noise (following a Gaussian distribution) was randomly generated for each trial. Such noise was then added to I_1 and I_3 in equation (4-6), and to I_L and I_R in equation (4-7), respectively. Based upon the preliminary experimental results, a SNR of 17 was selected. For a single lateral position, 50 trials in total were performed to estimate the uncertainty in positioning.

The two FoMs with noise taken into account are shown in Figure 4-9, for a CZT detector of 2.5 mm electrode pitch and 100 μm gap width. The sub-pitch resolution obtainable would be limited by the minimum distance between two lateral positions with no overlapping of their error bars. For the transient signal method, the sub-pitch spatial resolution is estimated to be ~250 μm shown in Figure 4-9 (a). For the charge sharing method, the sub-pitch spatial resolution is estimated to be ~30 μm shown in Figure 4-9 (b).

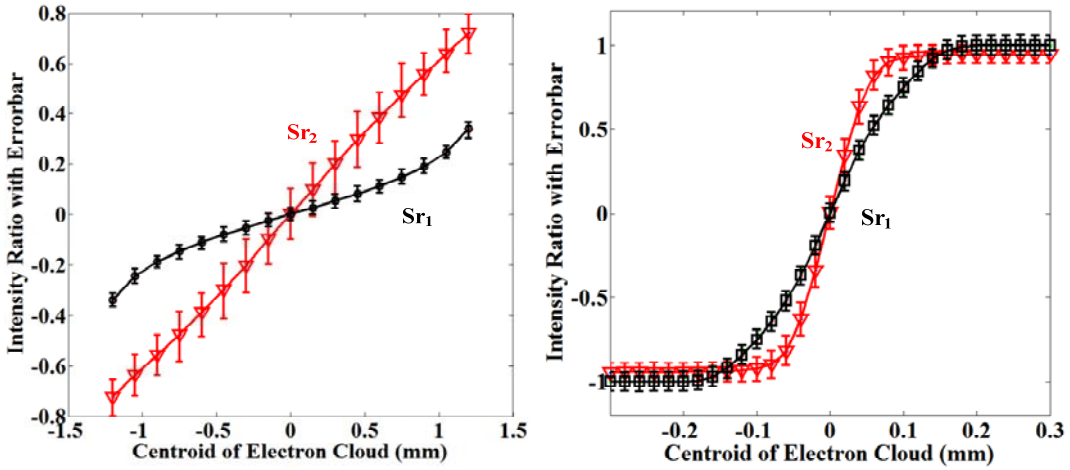

Figure 4-9, Intensity ratios Sr_1 and Sr_2 as a function of lateral position for (a) transient signal analysis (b) charge sharing effect. The error bar at a given lateral position corresponds to a SNR of ~17.

4.5. Discussion and Challenges

4.5.1. Electrode Design for CZT Detectors

The framework developed in this chapter can be used to guide electrode design in the use of the charge sharing method. For example, VR_{CSE} is found to be about 150 μm, with a bias of 400 V and a gap width of 50 μm for the detector shown in Figure 4-1. One consideration would be that the electrode pitch should be kept larger than the difference between VR_{CSE} and the gap (150 μm – 50 μm =100 μm). Otherwise, charge sharing is likely to involve three electrodes, which then limits its use. On the other hand, if the electrode pitch is too large relative to VR_{CSE}, the benefits resulting from the charge sharing method will be diminished, as implied by equation (4-5). For example, with a gap width of 50 μm, an electrode pitch of ~670 μm would yield a probability of ~50% for charge sharing while an electrode pitch of ~1730 μm reduces the probability to ~10%. Regarding the transient signal method, it shows no strong dependence on three gap widths selected. Nevertheless, one limitation in our current work is that only a constant electrode size (2.4 mm) was studied. Our future work will investigate the dependence of VR_{TSA} and sub-pitch resolution on electrode pitch, a parameter which would impact the crosstalk of the weighting potential between two electrodes as well as electronic noise.

Another consideration in electrode design is related to sub-pitch resolution. As shown in Figure 4-9 (bias: 400 V, pitch: 2.5 mm, gap width: 100 μm), a sub-pitch spatial resolution of ~30 μm is obtained within VR_{CSE} for the charge sharing method; while a sub-pitch spatial resolution of ~250 μm is obtained within VR_{TSA} for the transient signal method. If both methods are to be used simultaneously, the results provide a lower bound for the electrode pitch.

In addition, there are a number of practical challenges in the use of the transient signal method. First, due to the small amplitude of transient signals on the non-collecting electrodes, it is very sensitive to noise in detectors/electronics and thus requires low-noise front-end circuits. Second, in order to capture the waveforms of transient signals, either a free-running ADC or a specialized ASIC is required. Third,

to extract the amplitude information of transient signals, advanced digital shaping techniques are needed to improve the SNR.

4.5.2. Multiple Interactions of Gamma Ray Photons

One limitation for the two methods (VR_{CSE} and VR_{TSA}) studied in our work is that they are only applicable to single interactions of PE type, which amounts to 17% of all incoming 511 keV events. It should be pointed out that an event involving multiple interactions (M) would also produce signals on more than one electrode. For example, a CS interaction followed by a PE interaction (CS+PE) accounts for ~12% of all incoming 511 keV events within a 5 mm thick CZT detector. However, these M events will not benefit from the two methods discussed in this chapter.

To address this challenge, one may be able to distinguish a (CS+PE) event from a single PE event, based upon transient signals and advanced signal processing techniques. To illustrate this, four possible scenarios found in our preliminary experiments are presented in Figure 4-10. For a single PE interaction, the waveforms for the transient signal and charge sharing methods are shown in Figure 4-10 (a) and Figure 4-10 (b), respectively. Two features are observed for a single interaction (either PE or CS): 1) an abrupt change of the transient signal for the non-collecting electrode as shown in Figure 4-10 (a) for the transient signal method; and 2) two signals of the same rise time but different amplitudes as shown in Figure 4-10 (b) for the charge sharing method.

For a (CS+PE) event, two possible scenarios are shown in Figure 4-10 (c) and Figure 4-10 (d). In Figure 4-10 (c), the CS and PE interactions occur under two different electrodes and no charge sharing occurs. There is a noticeable time difference in terms of the rising edge between the CS and PE interactions, which is approximately 300 ns and depends on the energy and scattering angle of the CS interaction (i.e., Klein-Nishina formula). In Figure 4-10 (d), the charge sharing is caused only by the CS interaction and the PE interaction occurs under a single electrode. That's why the waveforms of the two electrodes show no difference in the rising edge between time zero and 1000 ns. Utilizing these features may allow us to distinguish single-interaction events from multiple-interaction events, as well as to identify the first interaction in a multiple-interaction event.

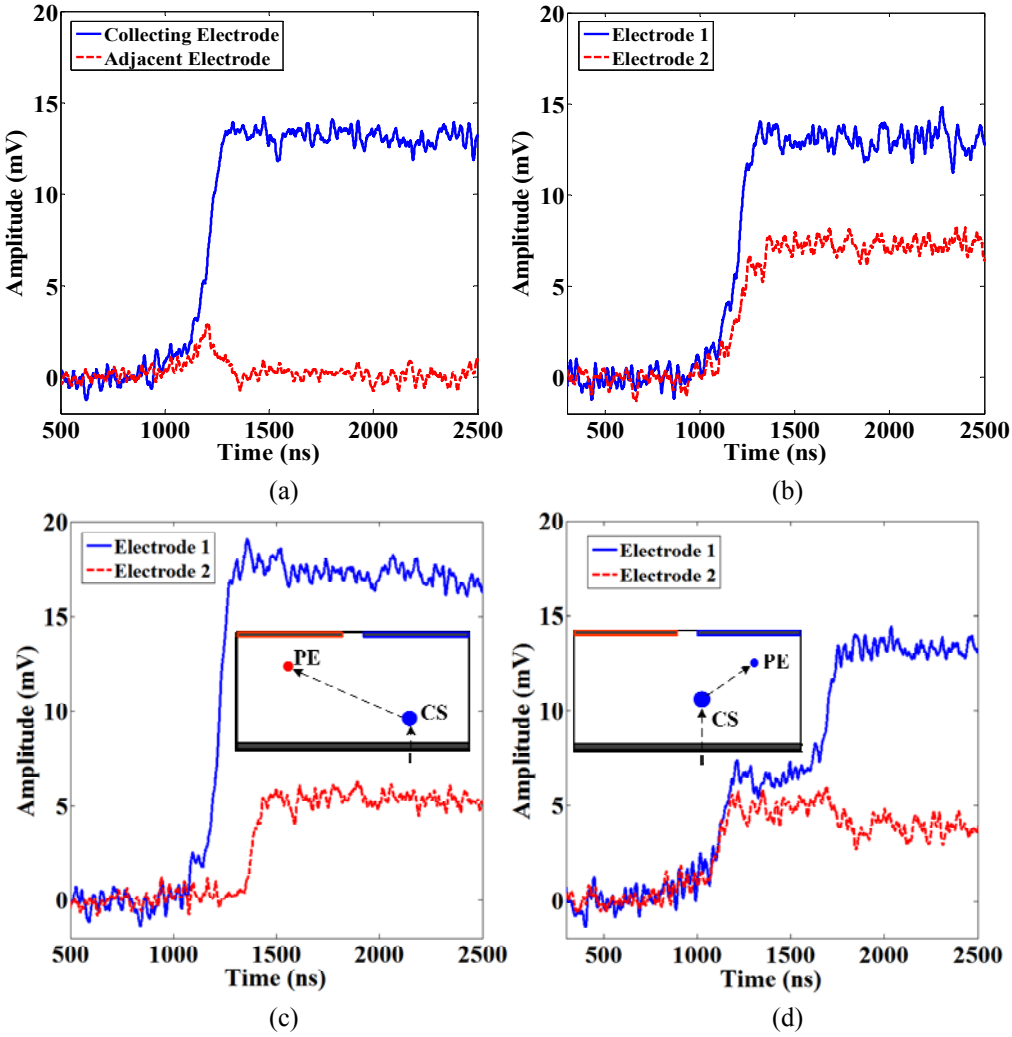

Figure 4-10, Illustration of the waveforms of four scenarios based upon preliminary measurements. (a) Transient signal scenario (a large signal on the collecting electrode and a small signal on the adjacent non-collecting electrode). (b) Charge sharing scenario (two adjacent electrodes divide the total number of induced charge). (c) Multiple-interaction scenario (PE and CS occur under two adjacent electrodes). (d) Multiple-interaction scenario (with only CS resulting in charge sharing between two adjacent electrodes).

4.5.3. Pixelated vs. Cross-Strip Electrode Configurations

The modeling of the weighting potential and electric field was primarily performed based on the pixelated configuration. Nevertheless, it can be applied to the cross-strip configuration with a number of minor modifications. For the pixelated configuration, the anode side consists of an array of small electrodes and the cathode side consists of a single layer. As a result, the electric field lines remain perpendicular between the anode and cathode planes, except the regions very close to the fine electrodes on the anode side. For the cross-strip configuration, both anode and

cathode electrodes are segmented into fine strips that are orthogonal to each other (Figure 4-1). In addition, steering electrodes are added in an interleaved mode with the anode electrodes in order to enhance charge collection or to utilize the small-pixel effect. Therefore, the electric field lines are directed towards the collecting anode electrodes with a larger curvature relative to the pixelated configuration. In this case, the charge sharing method can be used not on the anode side, but only on the cathode side to achieve sub-pitch resolution. On the other hand, the transient signal analysis method can be used on either anode or cathode electrodes, similar to the pixelated configuration.

4.6. Summary

In this chapter, we studied the feasibility of achieving sub-pitch spatial resolution in CZT detectors using two methods: charge sharing effect and transient signal analysis. We proved that their valid ranges of usage were complementary. The dependence of their corresponding valid ranges on electrode design, DoI, voltage bias and signal triggering threshold was investigated. Our results show that the valid range of charge sharing effect increases as a function of DoI, but decreases with increasing gap width and bias voltage. For a CZT detector of 5 mm thickness, 100 μm gap and biased at 400 V, the valid range of charge sharing effect was found to be about 112.3 μm around the gap center. This result complements the valid range of the transient signal analysis within one electrode pitch. For a SNR of ~17 and preliminary measurements, the sub-pitch spatial resolution is expected to be ~30 μm and ~250 μm for the charge sharing and transient signal analysis methods, respectively. Human full-body PET scanners (FoV~66cm) typically have a spatial resolution of ~7 mm. A typical breast or brain on the other hand measures less than 20 mm in diameter. Thus, a dedicated breast or brain PET systems with 2 mm spatial resolution, or better, are needed to provide the higher spatial sampling frequency required to resolve the fine details of organs accumulating tracers within a scan subject. Therefore, these results are expected to help optimize the design of electrodes as well as advanced signal processing for CZT-based PET systems, especially high resolution PET.

Chapter 5

CZT DETECTOR IN PHOTON-COUNTING CT IMAGING[§]

As a promising photon-counting detector, several physical effects of pixelated CZT lead to detected events with reduced energies, including characteristic X-ray emission, charge diffusion and trapping of charge carriers. In this chapter, we characterize CZT detector properties and address some limiting factors by optimizing detector design to make the detector viable for clinically applications. First, mechanisms resulting in charge loss in photon counting CT will be discussed. Second, the effects of electrode parameters will be investigated, including incident beam position and pixel configuration. Finally, the optimized design will be concluded based on calculated effective count rate, energy conversion factor and energy spectra.

5.1. X-ray Interaction in CZT Detectors

Currently, CT is one of the most commonly used imaging modalities for medical diagnostics. Conventional charge-integrating CT records the total charge generated by many X-ray photons, so all energy-dependent information is lost. Dual-energy CT imaging was developed to provide tissue-specific information with various techniques, such as dual-kVp, dual-source, dual-layer and rapid switching kVp [139]–[145]. However, the number of resolvable energy windows (i.e., basis functions) is limited

[§] Part of this work was submitted as: X. Zheng, Z. Cheng, M. J. Deen and H. Peng, "Effect of Charge Sharing and Characteristic X-ray Emission in CZT Detectors for Photon-Counting Computed Tomography Applications," to IEEE Transactions on Nuclear Science.

to two. Therefore, objects with similar attenuation curves cannot be distinguished. To remedy this, photon-counting (or spectral) CT was introduced to reveal additional quantitative information by employing energy-sensitive photon counting devices. Photon-counting CT can be used to extract the energy information of individual X-ray photons, thus increasing the contrast-to-noise ratio (CNR) of images, while reducing radiation dose given to patients [16], [17], [146].

One fundamental task in photon-counting CT is to obtain the correct energy information of each incoming photon. Cadmium Zinc Telluride (CZT) has emerged as a promising candidate for the photon counting detector due to its wide band-gap, high atomic number, high density, and excellent energy resolution compared to scintillator-based detectors [145], [146]. Nevertheless, several challenges exist in their practical applications, including hole trapping [39], [149], charge sharing, characteristic X-ray emission and non-local reabsorption. The resulting incomplete charge collection (also known as charge loss) would distort the energy spectrum and cause artifacts and inaccuracies of CT numbers [150], which could be mitigated through either single polarity charge sensing technique or "small pixel effect" [150]. However, when the pixel size is reduced to achieve higher spatial resolution, charge sharing and charge loss become more serious [151].

Charge loss in CZT detectors arises from two processes: characteristic X-ray emission and charge diffusion. First, only photoelectric effect (PE) type interactions are relevant, since the probability of Compton scattering in a CZT detector is very low (e.g. ~2% for a 60keV photon), [152]. It is possible that the resulting characteristic X-ray photons are reabsorbed by adjacent pixels, which results in charge cross-talk [153]. Second, the charge clouds are originally produced by either photoelectrons or reabsorbed characteristic X-rays photons. Charge diffusion results in the broadening of these charge clouds during charge collection. Then, charge sharing occurs if these charge clouds are collected by more than one pixel.

The performance of CZT in X-ray imaging was previously studied by several groups using both simulation models and experimental measurements [129], [154]–[157]. For example, the effects of the characteristic X-rays as a function of pixel size (ranging from 0.1 mm to 1.0 mm) was investigated in [152], but hole trapping and

charge diffusion were not considered. In [158], charge loss was obtained by modeling the initial charge cloud and the behavior of characteristic X-rays. An experiment was conducted [129] with a CZT detector (250 μm pitch) to measure a monochromatic X-ray beam of energies below 26 keV and above 40 keV. The results suggested that when the beam struck the center of a pixel, no charge sharing was found for 26 keV photons, while nearly 10% of events suffered from charge sharing for 40 keV photons. Moreover, the region associated with charge sharing was found to be larger for 40 keV photons relative to the 26 keV photons. This region decreased as the bias voltage of the CZT detector was increased.

Efforts were made to correct the effect of charge sharing, and improve energy resolution and photon counting efficiency. One recent study [128] reported that for a CZT detector of 250 μm pitch and 1 mm thickness, the percentage of events involving charge sharing amounted up to 36.4% at 59.5 keV. The charge sharing addition (CSA) algorithm (i.e., the deposited energy of each electrode was summed up) resulted in a small increase in the energy resolution, but the detection sensitivity increased significantly from 63% to 93%.

The primary goal of this work is to quantitatively investigate the effects of charge sharing and characteristic X-ray emission in CZT detectors, particularly for photon counting CT applications. First, the valid range of charge sharing is studied to evaluate the charge loss in the CZT detector. To our best knowledge, this has not been done in previous works. Second, we investigated the effects of the incident beam location and pixel configuration on the performance of CZT detectors. These are required when optimizing the CZT detector's design parameters and operating condition for photon counting CT applications.

5.1.1. Modeling of Photon Interaction and Distribution of Photoelectrons

As introduced in Chapter 2, the Monte-Carlo simulation was used to model the interaction of incoming X-ray photons with the CZT detector. In the simulation, a CZT detector of 20mm ×20mm ×3mm dimensions (density=5.68 g/cm^3) was built. The physical processes, which are interest in CT, were categorized into three types: photoelectric effect (PE), Compton scattering (CS) and Rayleigh scattering (RS). For

every event, its spatial coordinates (x, y, and z), deposited energy, and interaction information were saved in list-mode for post-processing.

To simplify the simulations, a 60keV mono-energetic X-ray beam was used. The probability of the PE event is ~ 94% at this energy, dominating the other two physical processes (~2% for CS and ~4% for RS). Therefore, only PE events were included in this study. The collimated 60keV beam was configured to strike the center (x=0, y=0) of the detector slab. For each PE event, the ejected photoelectron moves within the detector and gradually slows down by losing energy through ionization, and releasing secondary electrons until it finally stops. The distance between the initial interaction location and the endpoint gives the primary size of the charge cloud.

The 2D spatial profile of the photoelectrons is shown in Figure 5-1 (a), which reflects the spread of the endpoints from the initial generation site (x=0, y=0) within the detector. The maximum distance is found to be ~10 μm and this value is used to estimate the initial electron cloud size. The primary depth where PE interactions occurred is shown in Figure 5-1 (b), which demonstrates an exponential distribution due to the Beer Lambert's law.

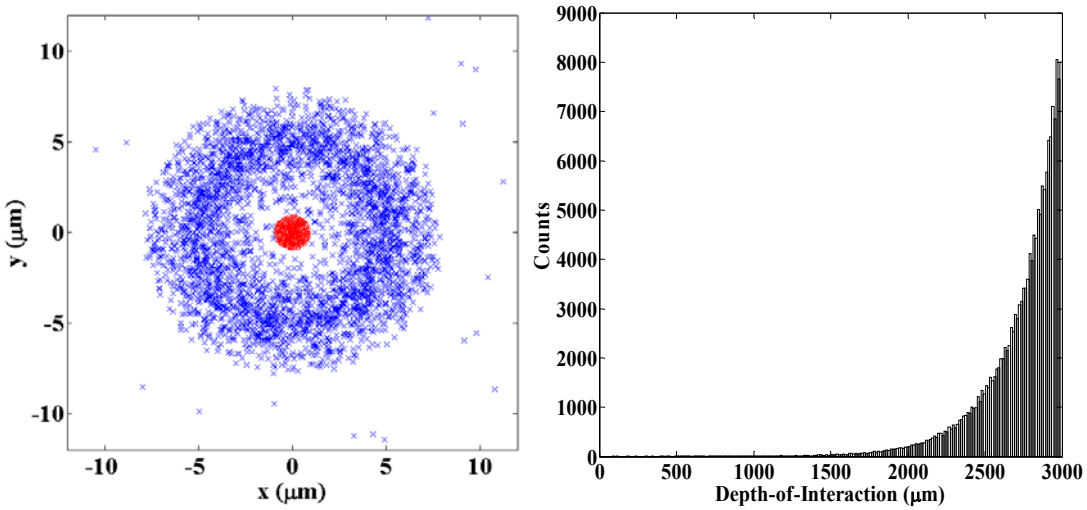

(a) (b)

Figure 5-1, (a) 2D spatial distribution of primary interaction sites (red dots) and the end positions of recoil electrons (blue dots). (b) The depth distribution of primary PE interactions. (Cathode: 3mm, Anode: 0)

5.1.2. Characteristic X-rays Emission and Reabsorption

It is known that PE events occur when the energy of an incident photon is greater than the K-shell absorption energy of an atom. In this situation, a characteristic X-ray

photon is created through the atomic de-excitation process, and it exhibits discrete energies. In our simulations, the energy of characteristic X-ray photons is set to the average value of K-L and K-M transitions (i.e. 23.4 keV for Cd and of 27.5 keV for Te, respectively) [152], [153]. The characteristic X-ray is simply referred to as K X-ray in next sections. The K X-ray photons from Zn are ignored because of its smaller atomic number and lower weight fraction.

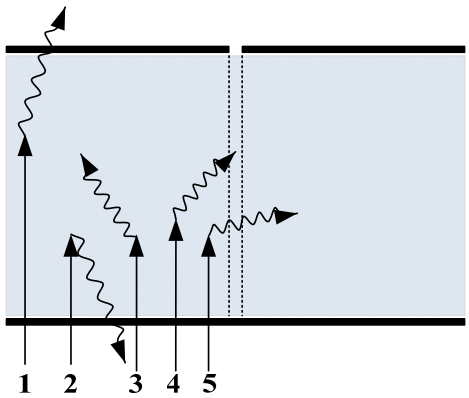

Figure 5-2. The possible scenarios of escaped K X-rays: 1-Forward-escape; 2-Backward-escape; 3-Full absorption; 4-Side-escape with charge sharing; 5-Side-escape with cross-talk.

An important challenge is how to estimate the likelihood of escaping K X-rays entering adjacent pixels, which causes charge cross-talk and spatial resolution blurring. Three possible scenarios are illustrated in Figure 5-2, forward-escape, backward-escape and reabsorption. The event classified as forward-escape is when the calculated absorption depth is larger than the detector thickness (event 1). If the calculated absorption depth is smaller than 0, then the event is classified as backward-escape (event 2). Others are considered as reabsorption. The forward-escape and backward-escape would result in count loss, i.e. lower detection efficiency. The pixel where PE interaction occurred is defined as the primary pixel. Thus, when the reabsorption process is in the primary pixel, it can be classified as a full absorption (event 3). Other reabsorptions are side-escapes and can be divided into the following two cases:

1) If an escaped photon is absorbed over a region near the boundary between adjacent pixels, charge sharing is to be included (event 4).

2) If an escaped photon is completely absorbed by adjacent pixels (i.e. cross-talk),

the energy collected by main pixel will be lower than that of the incoming photon (event 5).

The fraction of side-escape K X-rays are estimated by modeling shown in Figure 5-3. The traveling distance in lateral and depth directions is Δx, Δy, and Δz, respectively.

$$\Delta x = r \times \sin(\varphi); \Delta y = r \times \cos(\varphi) \tag{5-1}$$

$$r = d \times \sin(\theta); \Delta z = d \times \cos(\theta) \tag{5-2}$$

where r, θ, and φ are indicated in Figure 5-3. The actual attenuation length of K X-rays before reabsorption is d. The distance d is determined based on exponential attenuation $d = -\lambda \times \ln(R)$, where R represents a uniformly distributed random number between 0 and 1. Here, the emission of K X-rays is assumed to be isotropic. The attenuation length λ of the K X-rays are 116μm and 64μm for the Cd and Te, respectively.

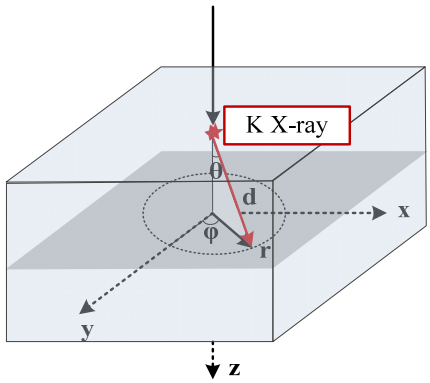

Figure 5-3, Modeling of K X-rays reabsorption.

In this work, all the calculations were based on the PE events obtained from Monte-Carlo simulations. The absorbed depth of the Cd-atom K X-rays is shown in Figure 5-4 (a), as an example. It is noted that the cathode surface is located at a DoI of 3 mm. So an absorption depth larger than 3 mm implies that the K X-ray photon leaves the detector volume from the cathode side, which is defined as "backward-escape".

The fractions of forward-escape, backward-escape and reabsorption of K X-rays are calculated and summarized in Table 5-1. The fraction of forward-escape is zero

because the detector is thick enough to prevent all K X-rays escaping from anode side. It is noted that the results in Table 5-1 are independent of the pixel configuration. The fraction of side-escape of reabsorbed K X-rays is illustrated in Figure 5-4 (b), which depends on both pixel size and gap width. For example, if we keep the pixel size fixed at 100μm and decrease gap from 100μm to 10μm, the corresponding fraction of side-escapes increases from ~8% to ~50%. This is because less K X-rays are absorbed within the smaller gap area between the primary pixel and its adjacent pixel.

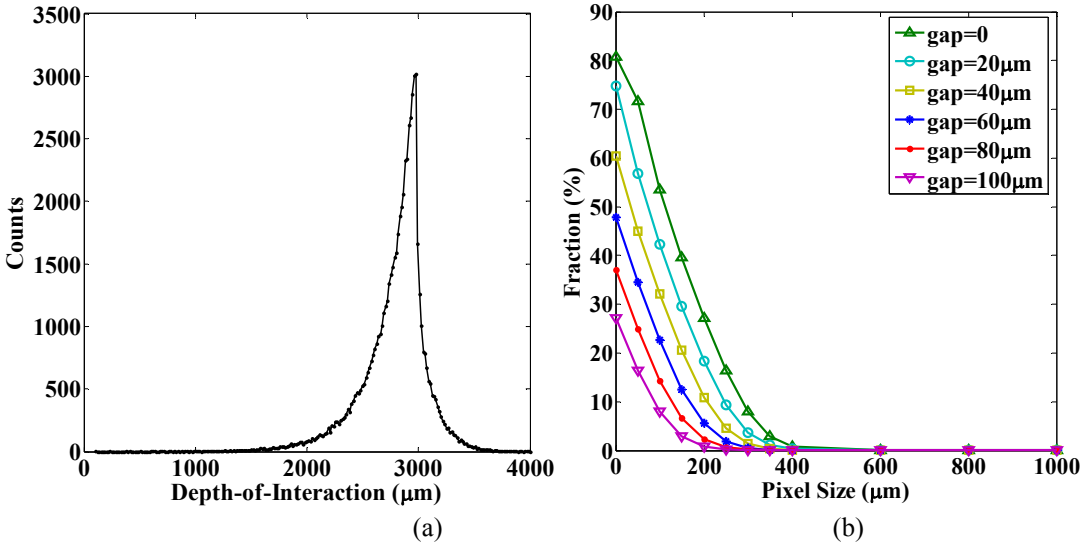

Figure 5-4, (a) The absorption depth of the K X-rays. (b) The fraction of side-escape K X-rays as the function of both pixel size and gap width.

Table 5-1, The fraction of frontward-escape, backward-escape and reabsorption K X-ray

	Cd K X-ray	**Te K X-ray**	**Total**
Forward-escape	0	0	0
Backward-escape	6.2%	12.4%	18.6%
Reabsorption	33.8%	47.6%	81.4%

5.1.3. Intrinsic Energy Loss of Signal Generation

In practice, the output signal of an electrode is affected not only by the deposited photon energy, but also by the "small pixel effect", DoI and trapping of charge carriers. In this part, the transport of charge carriers within detector is modeled by the finite element method (FEM) as illustrated in Chapter 2. The induced charge is also analyzed based on the Shockley-Ramo theory. The trapping effect was modeled in our previous work [4] for three depths (10%, 50% and 90% of the detector thickness L relative to the anode surface). The induced signal consisted of two parts: electron-

included charge (fast rising part) and hole-induced charge (slow rising part). One important result was that the signal amplitude of the near anode field interaction was visibly lower than that of the far anode field case. This was due to hole trapping near the anode electrode's sensitive area, which induced a signal of reverse polarity to the electron-induced signal. The results also revealed that the DoI effect would cause varying output amplitudes with incident photons of the same energy.

5.1.4. Charge Diffusion

The size of electron cloud increases with DoI due to charge diffusion. Either a longer traveling distance or a longer traveling time yields a more noticeable broadening. The same analysis and theory as in Chapter 4 are used here to evaluate the influence of charge diffusion and charge sharing effect. However, the modeling is modified to be specific for X-ray imaging. The maximum value of broadening (sigma σ, assuming a Gaussian shape) is ~33.9 μm. This is when the electron cloud was generated very close to the cathode (i.e. DoI = 3 mm here) with the bias of 400V. Figure 5-5 (a) shows two electron cloud profiles with charge sharing involved at DoIs of 0.5 mm and 1 mm, respectively. The centroid of the electron cloud is located at the center of gap (beam location=0 mm). Figure 5-5 (b) shows the behavior of the normalized signal intensity of the left pixel (I_1), gap (I_2) and right pixel (I_3) with a collimated 60keV beam shifting from the left to the right side (100 μm gap width), when no electronic noise is included.

Then, the dependences of VR_{CSE} on gap width, DoI and bias voltage are illustrated in Figure 5-5 (c) and (d). First, for those missing data points at a given configuration (i.e., 150 μm gap, 0.5 mm DoI), no charge sharing occurs because the size of the electron cloud is relatively small compared to the gap width. Second, an approximately linear relationship is found between VR_{CSE} and DoI for various gap widths, as shown in Figure 5-5 (c). For example, at a fixed DoI of 3 mm, VR_{CSE} is ~ 22.2 μm and ~58.2 μm for the gap width of 100 μm and 50 μm, respectively. Third, the dependence of VR_{CSE} on bias voltage and DoI (gap width is constant) is presented in Figure 5-5 (d). At a DoI of 1 mm, VR_{CSE} is ~86.2 μm and ~9.89 μm, for a bias of 200 V and 800 V, respectively. While at a DoI of 3 mm, the corresponding VR_{CSE} increases up to ~93.7 μm and ~31.3 μm, respectively. The lower bias voltage causes

the slower electron velocity, i.e. the longer traveling time. Meanwhile, the larger DoI means longer traveling distance. As a result, the bigger difference among VR_{CSE} is observed at the right edge of Figure 5-5 (d). These results indicate that the charge sharing effect can be effectively suppressed by increasing the bias voltage.

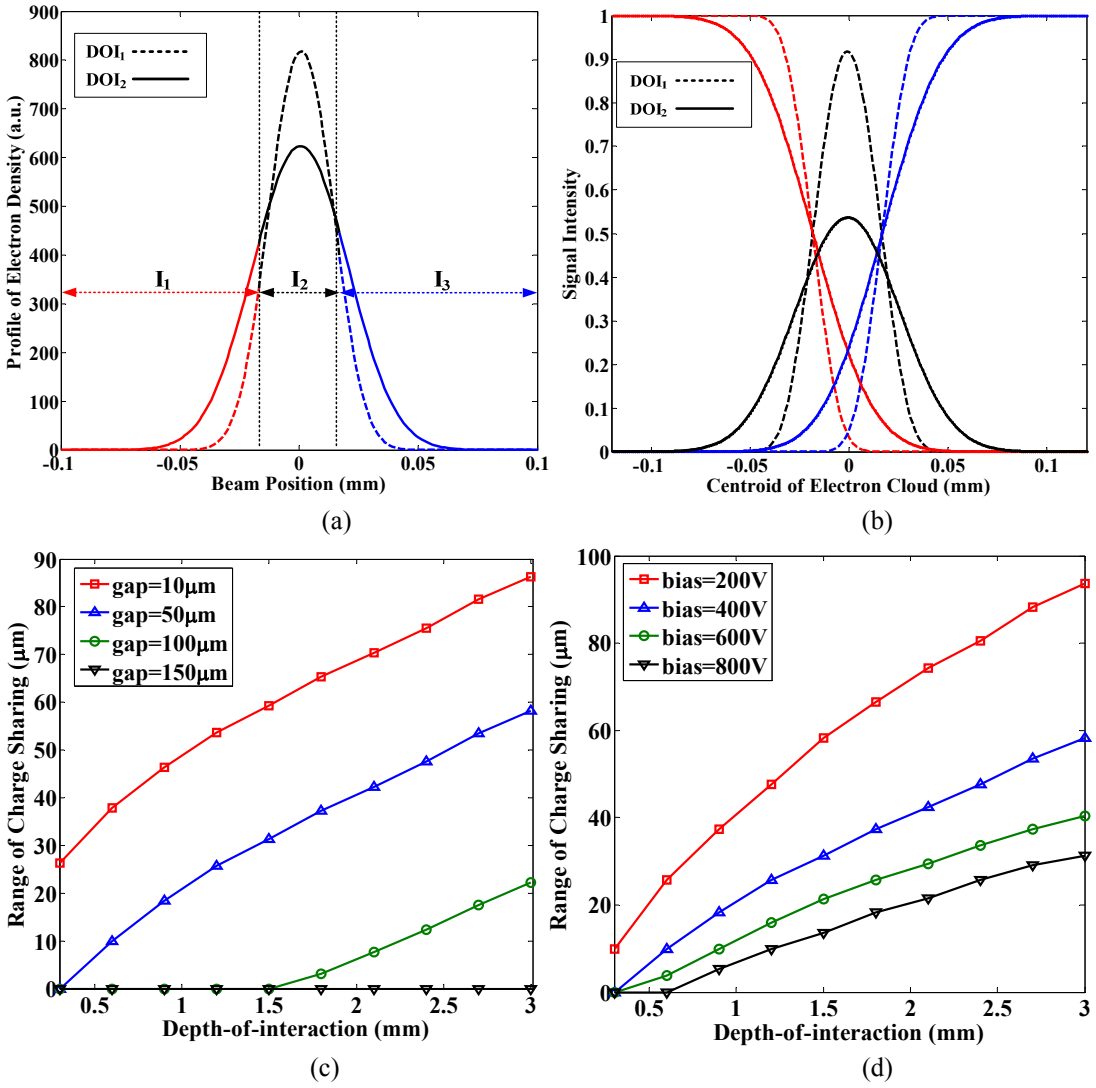

Figure 5-5, (a) Illustration of the profiles of the electron clouds at two different DoIs (the gap width is 50 μm). (b) Signal intensity $I_1/I_2/I_3$ for two DoIs. (c) The VR_{CSE} as a function of gap width and DoI (the bias voltage is 400V). (d) The VR_{CSE} as a function of detector bias and DoI (the gap width is 50μm). A DoI of 1 mm corresponds to a depth of 1 mm distance from the anode. The triggering threshold was set to be 10% of the energy of the incident photons.

5.2. Detector Response and Energy Spectra

5.2.1. Simulation Setup

Both intrinsic energy loss and the charge sharing effect stated in section 5.1 are

considered to evaluate the total detector response and the energy spectra. From the analysis in section 5.1.4, we note that VR_{CSE} is affected by several parameters such as bias voltage, gap width and DoI. Therefore, the major task in this part is to determine whether a primary photoelectron or a K X-ray photon would cause charge sharing. This task is implemented by comparing the absorbed charge cloud with VR_{CSE} to see if its lateral location (x, y) falls into the range of VR_{CSE}. If charge sharing occurs, the energy loss is then calculated by following the procedure in the last section.

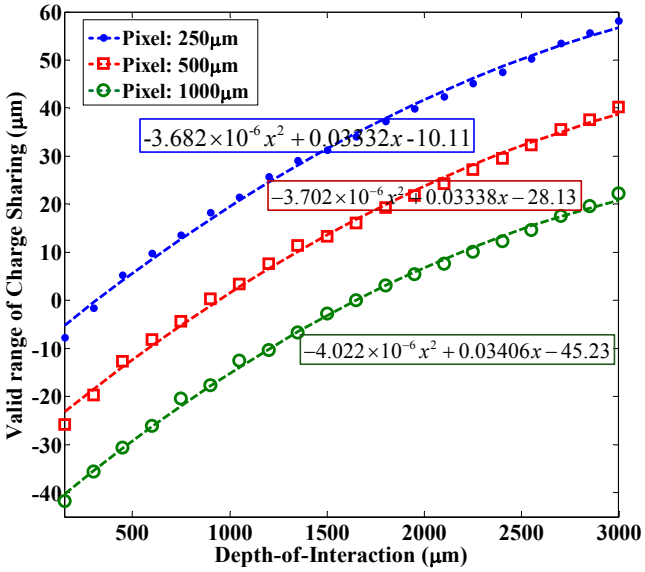

Figure 5-6, VR_{CSE} as a function of DoI for three pixel configurations.

The bias voltage is set to 400 V and three pixel configurations (pixel size/gap width) are chosen: 250 μm/50 μm (small pixel), 500 μm/75 μm (mid-pixel) and 1000 μm/100 μm (large pixel) based on the literature and practical clinical instruments. The detailed algorithm consists of the following steps.

- First, VR_{CSE} was calculated as the function of DoI for three pixel configurations as shown in Figure 5-6.
- Second, the data were fitted with quadratic polynomial equations.
- Third, the depth of each interaction extracted from Monte-Carlo simulations in section 5.1.1 was substituted into the fitting equations.
- Fourth, the corresponding VR_{CSE} of each interaction was obtained. It should be emphasized that the negative value of the vertical axis in Figure 5-6 implies that the probability of charge sharing is zero. In other words, since these interactions

are very close to anode, they have shorter traveling distances and thus smaller charge clouds with respect to the gap width.

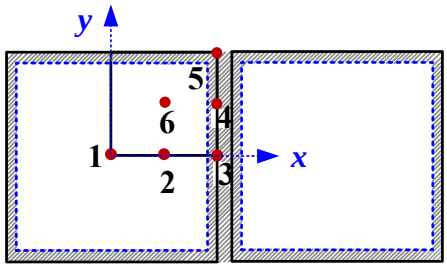

Figure 5-7, Illustration of six hit locations inside a single CZT pixel.

Instead of uniformly irradiating the whole pixel area, six beam hit locations (1 to 6 in Figure 5-7) were chosen to investigate the energy degradation. For this study, 200,000 photons were modeled at each location. Given the symmetry of a square pixel, by simple rotations and mirroring around the center, the analysis can be extended to the whole pixel surface. The possible scenarios taking into account both K X-ray photons and photoelectrons are shown in Figure 5-8.

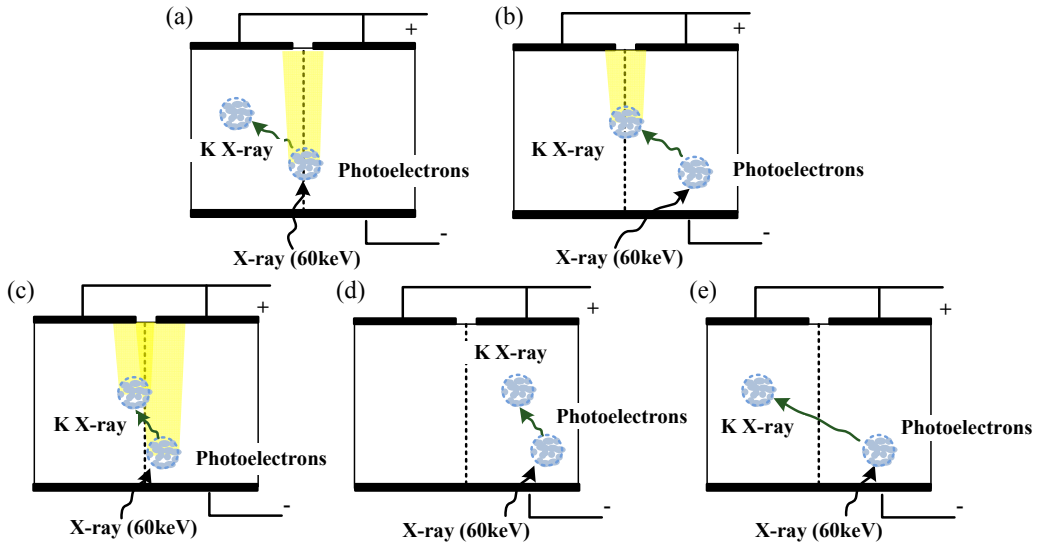

Figure 5-8, Transport of the absorbed photons between adjacent pixels. (a) Photoelectrons are absorbed within VR_{CSE}. (b) K X-rays are absorbed within VR_{CSE}. (c) Both photoelectrons and K X-rays are absorbed within VR_{CSE}. (d) Full absorption within the primary pixel. (e) Side-escape of K X-ray emission.

Two performance parameters were selected for quantitative analysis: the effective count rate and the energy conversion factor. The effective count rate is defined as the ratio between the number of detected photons without any charge loss to the number

of incoming photons, which is a good indicator for detection efficiency of a CZT detector. The energy conversion factor is defined as the ratio between the amplitude of the induced signal and that of the incoming photons. For example, the energy conversion factor of a full absorption event is 1. For an event involving charge sharing (i.e., within VR_{CSE}), the energy conversion factor is between 0 and 1.

5.2.2. Energy Spectra

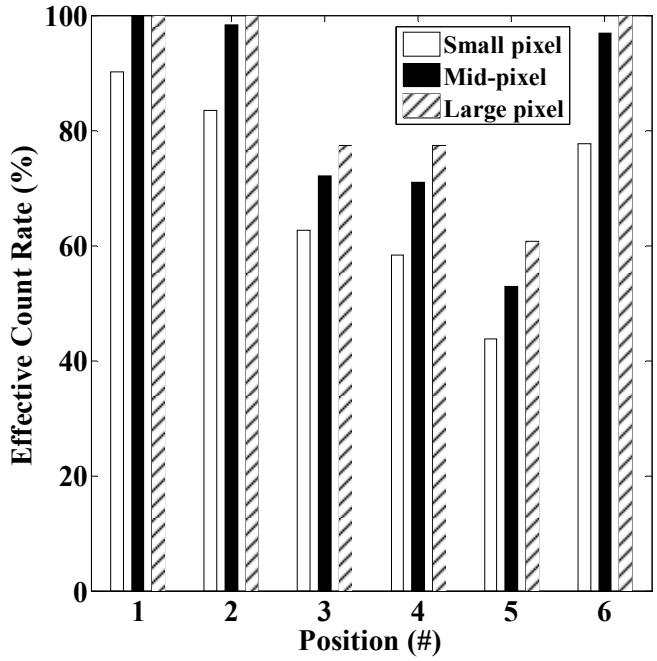

Figure 5-9, Effective count rate for pixels of different configurations.

Figure 5-9 gives the effective count rate with three pixel size/gap width configurations. The horizontal axis represents six incident beam positions (as the P_1-P_6 in Figure 5-7). First, the same trend is observed, that effective count rate decreases from the pixel's central area (P_1, P_2 and P_6) to the boundary (P_3 and P_4) down to the corner (P_5). Second, the effective count rate of the large pixel configuration increases by ~20% compared with that of the small pixel configuration. Third, the difference between effective count rates of mid-pixel and large pixel is around ~5% for all hit locations. This means that the pixel size can be reduced to 500 μm (mid-pixel size) without significant loss in the charge collection efficiency.

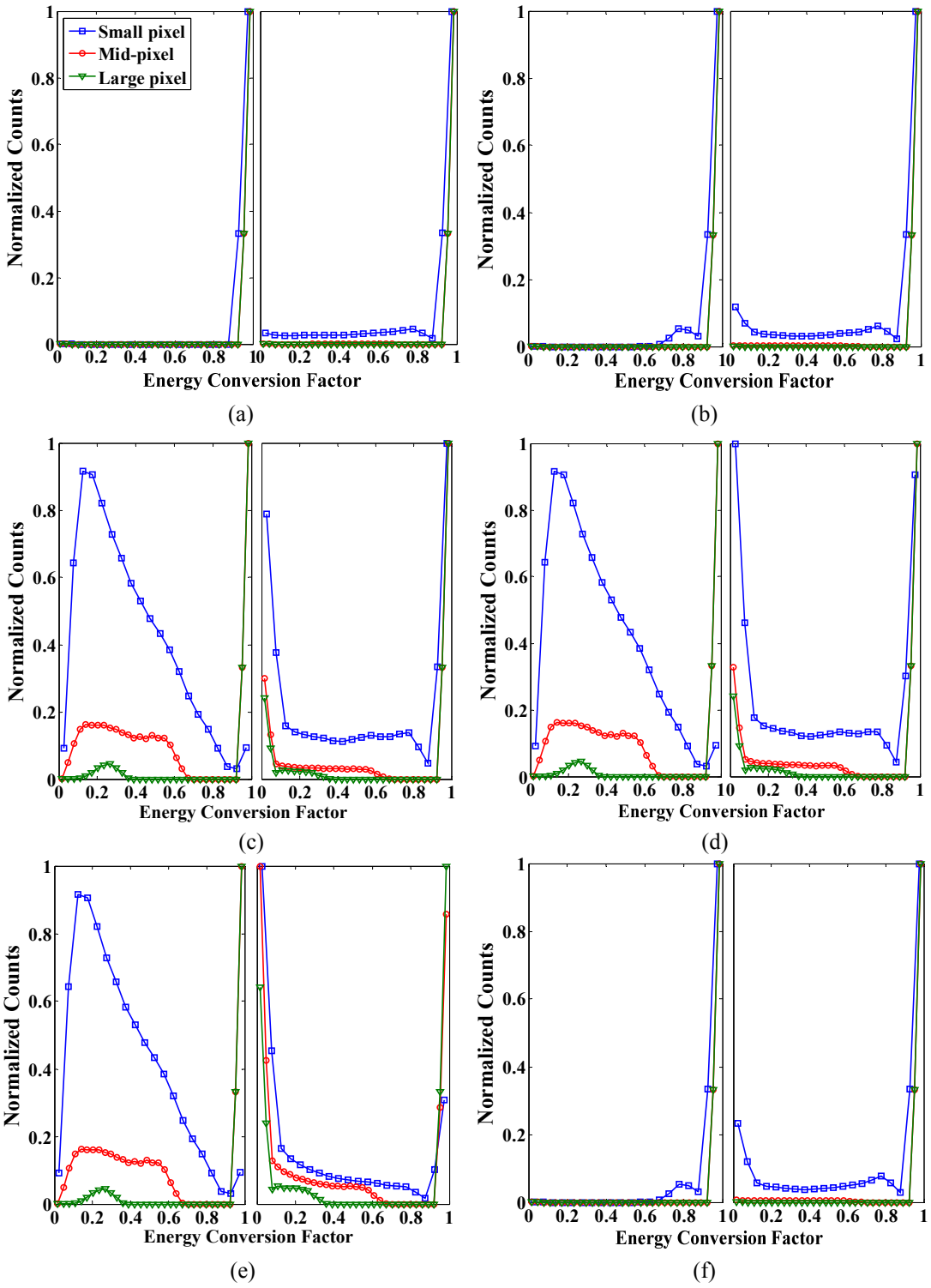

Figure 5-10, Energy conversion factor of photoelectrons (left column in each subplot) and characteristic X-rays (right column in each subplot) of pixels with three configurations. P_i in legend represents the incident beam position *i* in Fig. 4.

Next, the energy conversion factors are shown in Figure 5-10, for both photoelectrons and K X-rays. It is easy to separate all events into two clusters from the results: central cluster (P_1, P_2, and P_6) and the edge cluster (P_3, P_4, and P_5). Apparently, the energy conversion factor of edge cluster is lower than that of the central cluster. The peaks are observed in the region with a lower energy conversion factor (<0.4) in Figure 5-10 (c), (d), and (e). The reason is that the events of edge cluster are closer to the pixel boundary, which provides more opportunities of charge sharing or K X-rays escaping. In particular, the size of the photoelectron-induced electron clouds (<10 μm) is much smaller than the pixel size. Therefore, there is no difference in the energy conversion factor within the central cluster.

When the pixel size increases, the inter-cluster difference of the central cluster (P_1, P_2, and P_6) is smaller. For example, the energy conversion factors of all interactions are larger than 0.9 with mid- and large pixel in Figure 5-10 (b). However, for the edge cluster (P_3, P_4, and P_5), the energy conversion factor is profoundly affected by both pixel size and gap width. Therefore, a large difference is observed in Figure 5-10 (c), (d), and (e). For example, in Figure 5-10 (d), there are 40%, 20%, and 5% photoelectrons having energy conversion factor smaller than 0.2 for small, mid-, and large pixel configuration, respectively. At the same time, there are 40%, 29%, and 26% K X-ray photons having energy conversion factor less than 0.2 for small, mid-, and large pixel configuration, respectively. This is because the K X-ray photons have longer attenuation length λ (i.e. 116μm and 64μm for Cd and Te, respectively), so they can escape to adjacent pixels. Therefore, without smearing by intrinsic energy loss, the lower limitation of the pixel size can be set to 500 μm without degradation by the charge sharing effect or K X-ray emission.

Finally, the energy spectra in Figure 5-11 are formed by summing the photoelectron- and K X-ray- induced signals. A clear 60keV photopeak is shown for the spectra of the central cluster, which is consistent with the analysis for Figure 5-10. It is known that there is a pair of photoelectrons and K X-ray emission resulting from a single PE event. The photoelectron will be always detected due to its much shorter attenuation length compared with the pixel dimensions. However, the K X-rays escape to adjacent pixels with a higher probability as the pixel size decreases. This

results in some photopeak events shifting towards the lower low-energy region. Therefore, small peaks between 20keV and 40keV begin to appear. The decreased energy is equal to the energies of escaped K X-rays. Furthermore, the photopeak counts reduced sharply for the edge cluster due to the more charge loss. Also, no photopeak is observed for small pixel configuration.

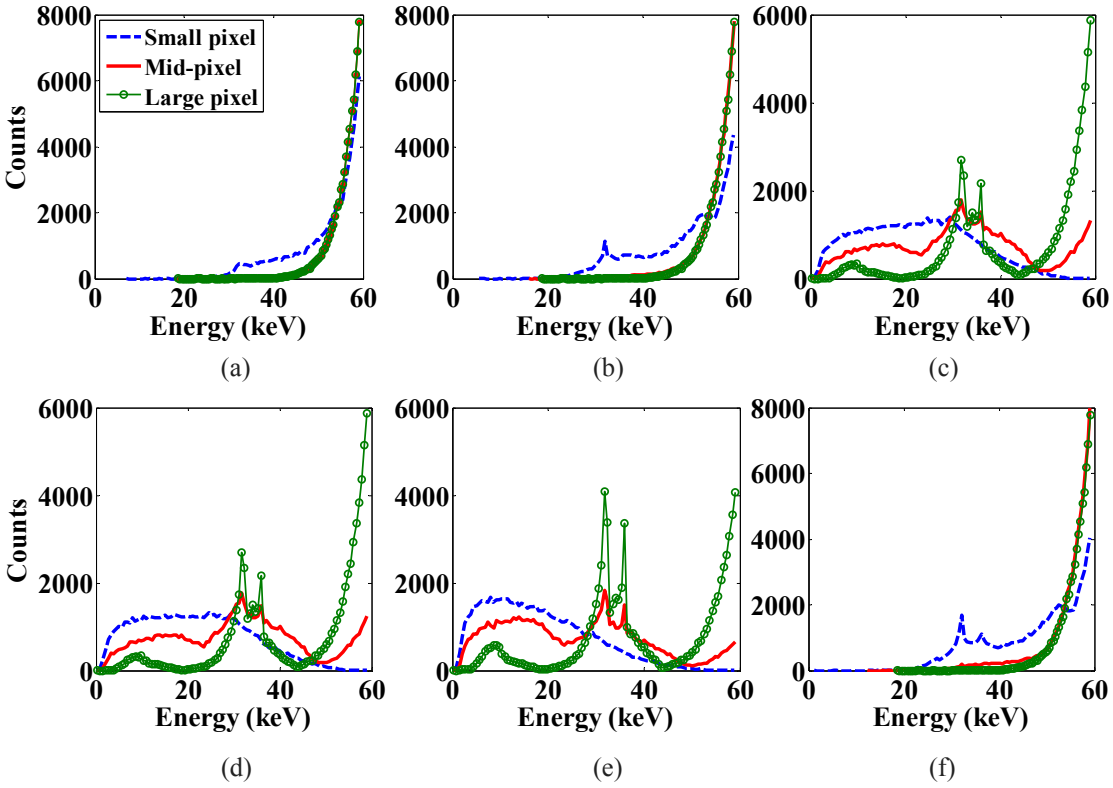

Figure 5-11, Energy spectra of six positions (P_1-P_6: left to right, up to down) for three pixel configurations. Pixel size/gap size are 250 µm/50 µm (small pixel), 500 µm/75 µm (mid-pixel) and 1000 µm/100 µm (large pixel).

5.3. Summary

The primary goal of this chapter is to better understand the effect of charge sharing and characteristic X-ray emission in CZT detectors for photon counting CT applications. This work was performed based upon our previous work with CZT detectors for the instrumentation in a PET system (511 keV) [151]. One critical requirement of photon counting CT is to accurately extract the energy information of individual incoming photons and assign them to different energy windows, either with or without average weighting schemes applied. However, as shown in our work,

the original energy information could be distorted (i.e., smaller amplitude) due to a number of factors, such as intrinsic energy loss, cross-talk of characteristic X-rays and the charge sharing effect. Though not within the scope of current work, we expect that the shift towards the lower energy would yield an underestimation of HU at a lower energy, but an overestimation of HU at a higher energy. In this chapter, we systematically investigated the effects of beam hit location and pixel configuration on charge loss and energy spectral distortion. These results are expected to help us to optimize the design parameters and operation conditions of CZT detectors for photon counting CT application. They can also be used to identify the relationship between the performances of CZT detectors (i.e., count loss and energy spectral) and quantitative derivation of Housefield Unit from CT images.

It was found that the small pixel effect does help to mitigate the impact of intrinsic energy loss. However, 70% of the incoming photons will produce K X-rays and a large fraction of them will escape from the pixel where the primary interaction occurs. The reabsorption of those K X-ray photons in other pixels contributes to cross-talk. The fraction of cross-talk can be reduced by using a relatively larger pixel. Also, the detection efficiency increases with pixel size, but the penalty is an inferior spatial resolution. Therefore, there is the tradeoff for the pixel design. From the comprehensive analysis and energy spectral studied in this work, we conclude that the pixel size can be reduced to 500 μm without performance degradation due to charge sharing effect or characteristic X-ray emission, as well as no significant charge collection efficiency loss.

Chapter 6

CONCLUSIONS AND RECOMMENDATIONS

This thesis stemmed from the recognition that the CZT semiconductor's material properties make it an excellent candidate detector material for use in medical imaging applications. The research conducted in this thesis consisted of three parts: analytical modeling of the CZT detector's performance, experiments and improvements performed with CZT detector for PET imaging, and the feasibility study for photon counting CT. A number of important findings and conclusions are summarized in this chapter. In addition, recommend future work is discussed.

6.1. Conclusions

The most significant contribution of this work comprises the comprehensive experimental and theoretical studies of CZT detector. First, in chapter 2, an analytical modeling for semiconductor radiation detectors was proposed, including photon interaction within detector, charge transportation and induction on electrodes. This provides a powerful tool for understanding the detector's behavior to optimize detector design and configuration. It is a cost-effective way to perform relevant studies of semiconductor photon detectors. The model was derived from the general radiation detection Shockley-Ramo theory. However, we extend it for two specific medical imaging applications: PET (511 keV) and CT (60 keV). In addition, due to the unique properties of CZT detectors, the Shockley-Ramo theory has also been studied for different detector geometries and electrode patterns. The results demonstrated depth sensing technique achieved by C/A ratio and electron drift time, which was successfully used for depth calibrations and performance improvement.

Second, in chapter 3, experiments were designed and performed to investigate the achievable energy resolution and time resolution of a PET prototype image based on the pixelated CZT detector. A number of factors emerged as the primary technical challenges for this project. The pixel size and brittleness of the CZT made electrode metallization and module assembly extremely challenging. This limited the speed of CZT photon detector module development and manufacturing, and reduced the process yield. The lack of intrinsic gain meant that the induced charge signal was easily overwhelmed by electronic noise. As a result, a lot of time was spent on design iterations to optimize components in the adapter PCBs.

Through extensive studies of CZT's material properties, the customized assembly of bare crystals with low cost and robust electronic connections was developed. The spring loaded pogo pins on regular PCB and holder were designed to align with individual small anodes. In order to protect detector's surfaces, ZEBRA, a silicon rubber sheet with conductive property, was used. The experimental results were also optimized with regard to applied bias and offline calibration algorithms. With depth calibration applied, the energy resolution of 2.26±0.84% at 662keV for single anode events was obtained. The time resolution was 19±3 ns FWHM with a bias voltage of 500V after electron drift time calibration.

Third, a novel algorithm was proposed and described in chapter 4 to achieve sub-pitch spatial resolution of PET system. Reducing the electrode size to achieve high spatial resolution would cause several practical problems, such as in manufacturing and fabrication of the detector, high cost, large number of readout electronics channels, and significant charge sharing and cross talk between electrodes. The proposed algorithm in this thesis was based on charge sharing effect and transient signal analysis. It allowed for a new level of precision of measuring the interaction sites in pixelated semiconductor detectors. Furthermore, the valid range of charge sharing effect was introduced for the first time, and its dependence on DoI, gap width and bias voltage were studied quantitatively. For 511keV incoming gamma rays, the sub-pitch spatial resolution of ~30 μm and ~250 μm within the valid ranges of charge sharing and transient signal analysis methods can be achieved, respectively.

Fourth, in chapter 5 the feasibility and capabilities of the CZT detector in photo-counting CT imaging was investigated. The characterization of the CZT detector explored low energy tailing of energy spectra caused by intrinsic charge loss, characteristic X-rays emission and reabsorption, and charge sharing caused by charge diffusion. A smaller pixel can decrease the hole trapping effect, but at the same time would increase the probabilities of characteristic X-rays escaping and charge sharing. Through extensive modeling with different pixel configuration and incident beam position, the results indicate that a detector configuration of 500 μm yields negligible count loss and charge loss. These results are expected to help us optimize the design parameters and operating conditions of CZT detectors for photon counting CT imaging.

6.2. Recommendations

There are several topics not addressed in this work that should be studied in the future to further improve the performances of CZT detectors and lead to the deployment of CZT detectors in practical medical applications.

- Currently, only the system response function for single-pixel events was modeled and investigated. For example, at 662 keV, the fractions of one, two, and three-or-more pixel events are 31%, 37%, and 32%, respectively [159]. As incident photon energy increases, the fraction of three-or-more pixel events also increases. In order to accomplish large detection efficiency, the incorporation of multiple-pixel events is necessary. This is a challenging task because, 1) from the ADC output value or waveforms, a multiple-pixel event is difficult to be distinguished from charge sharing effect; and 2) because of random amplitude that is lower than that of photopeak event, a multiple-pixel event is easily overwhelmed by electronic noise. Therefore, the coincident multiple-pixel events from several pixels require the readout system to have a higher SNR. In addition, the slope of cathode may provide useful information to help identify charge sharing effect and multiple-pixel events.

- In this work, a commercial ASIC chip was used to readout 36 anode channels simultaneously. This ASIC chip and its evaluation board are generic designs for instrumentation of semiconductor detectors. Each channel contains a charge-sensitive input amplifier with resistive-multiplier feedback, a differentiator, gain circuit, and two shaping amplifiers ("slow" and "fast") that operate in parallel. For different detector, its performances are optimized first by adjusting parameters, such as shaping time, amplifier gain, and threshold level. Therefore, based on these optimized parameters, the specialized readout electronics can be designed for custom CZT detector to make more compact system with lower noise and at lower cost.
- A novel sub-pitch spatial resolution algorithm has been developed for PET system with CZT detector, which requires experimental validation in the future. One of the challenges is to design detectors with various electrode configurations (pixel size and gap width). As noted in several places through this thesis, the size, brittleness and operation temperature of the CZT crystals made fabrication, electrode metallization and module assembly extremely challenging. Therefore, a commercial solution for detector packaging is required or can be developed to address these issues in a timely manner.
- All calibration processes to improve energy resolution and coincidence time resolution are accomplished offline. It may be more beneficial to integrate them with current components at hardware-level to make the prototype commercially viable. For example, the implementation on FPGA is suggested. And 3D integration can be used to locate dense and complex electronics. In addition, studies of temperature dependence and long term stability must also be carried out before the prototype can be used in PET and photon counting CT applications.
- In practice, the glucose metabolic rate is estimated to be ~ MHz, which is slower than available clock rate of FPGA/ASIC (few hundreds MHz). Therefore, the information of radiotracer concentration in patient body are finely sampled and processed in PET and photon-counting CT. The

running time of proposed algorithms with Matlab in PC is less than 10 minutes when dealing with relative large data size (100000 events), that is expected to be shorter when they are implemented by FPGA/ASIC.

- Compare to the pixelated pattern, the cross-strip electrode pattern can achieve the same high spatial resolution while using a lower number of electronic readout channels, i.e. 2N vs. N^2. At the same pixel pitches, x-y localization of photon interactions can be achieved by finding the intersection of the electrode strips producing the signal. In addition, the small pixel effect and single polarity sensing technique can be achieved by modifying the width of anode electrode. Thus, cross-strip CZT detector is worth to be investigated in future.
- Currently, the pulse height correction for single pixel events is performed using depth sensing by C/A ratio or electron drift time. The measured C/A ratio and the electron drift time are two independent depth parameters. It would be an interesting topic to identify the relationship between them. Theoretically C/A ratio and electron drift time can be used together to get a better result of pulse height correction and achieve the optimized spectroscopic performance of CZT detector from the single pixel events. This is a recommended topic for future work.
- The work in this thesis proved the 3D imaging capability of CZT detector in PET system. The depth resolution under 500V bias voltage for a 5mm thick CZT detector was derived to be ~0.89mm. For the identification of the practical depth resolution in the future, a pinhole (~μm) collimator moving in depth direction can be used. The length and pinhole's diameter of collimator are required to be chosen carefully to produce proper photon beam size at the end nearest to the test detector. As expected, this would results in lower sampling rate and longer sampling time.
- Because in a thinner crystal the holes are more effectively drifted and trapping probability is smaller. The hole trapping in CZT can be decreased by reducing the thickness of detector. However, detector with small thickness has low photon attenuation for energies of practical interest.

When the radiation beam is directed at a tilted angle with respect to the CZT surface [69], [160], the path of the radiation is increased so that photon attenuation is high, while the CZT thickness is kept small enough to maintain hole trapping at a low level. Furthermore, the small CZT thickness will minimize spreading of the charge and charge sharing between pixels and charge buildup in CZT. In our experiments, the source irradiated detectors' surface with the right angle (90°). Therefore, the dependence of system's performance on tilted angle of source irradiation would be another interesting research topic.

The work presented in this thesis was a pilot research to investigate a novel semiconductor detector, targeting the PET and photon counting CT imaging applications. We have already seen the use of semiconductor photon detector giving rise to new calibration and coincidence event identification algorithms. The CZT-based medical imaging system will open the door to entirely new classes of imaging algorithms and capabilities that will, for example, exploit the system's superior energy resolution for random rejection, LoR placement and Compton imaging.

REFERENCES

[1] P. Vaska, A. Bolotnikov, G. Carini, G. Camarda, J. Pratte, F. A. Dilmanian, S. Park, and R. B. James, "Studies of CZT for PET Applications," 2005, pp. 2799–2802.

[2] H. Peng and C. S. Levin, "Design study of a high-resolution breast-dedicated PET system built from cadmium zinc telluride detectors," *Phys. Med. Biol.*, vol. 55, no. 9, pp. 2761–2788, May 2010.

[3] P. Vaska, A. Dragone, W. Lee, D. H. Kim, J. F. Pratte, Y. G. Cui, J. Fried, S. Krishnamoorthy, A. Bolotnikov, S. J. Park, P. O'Connor, F. a. Dilmanian, and R. B. James, "A prototype CZT-based PET scanner for high resolution mouse brain imaging," in *IEEE Nuclear Science Symposium Conference Record*, 2007, vol. 5, pp. 3816–3819.

[4] X. Zheng, M. J. Deen, and H. Peng, "Performance Characteristics of CZT Detectors for PET Imaging Applications," *ECS Trans.*, vol. 61, no. 35, pp. 7–13, Sep. 2014.

[5] H. Peng and L. Craig S., "Recent Developments in PET Instrumentation," *Curr. Pharm. Biotechnol.*, vol. 11, no. 6, pp. 555–571, 2010.

[6] Z. He, "Review of the Shockley–Ramo theorem and its application in semiconductor gamma-ray detectors," *Nucl. Instruments Methods Phys. Res. Sect. A Accel. Spectrometers, Detect. Assoc. Equip.*, vol. 463, no. 1–2, pp. 250–267, May 2001.

[7] E. Downie, X. Yang, and H. Peng, "Investigation of analog charge multiplexing schemes for SiPM based PET block detectors," *Phys. Med. Biol.*, vol. 58, no. 11, pp. 3943–3964, 2013.

[8] T. F. Budinger, "Time-of-flight positron emission tomography: status relative to conventional PET.," *J. Nucl. Med.*, vol. 24, no. 1, pp. 73–8, Jan. 1983.

[9] T. F. Budinger, "PET instrumentation: What are the limits?," *Semin. Nucl. Med.*, vol. 28, no. 3, pp. 247–267, Jul. 1998.

[10] E. M. Rohren, T. G. Turkington, and R. E. Coleman, "Clinical Applications of PET in Oncology," *Radiology*, vol. 231, no. 2, pp. 305–332, May 2004.

[11] F. Y. J. Keng, "Clinical applications of positron emission tomography in cardiology: a review.," *Ann. Acad. Med. Singapore*, vol. 33, no. 2, pp. 175–82, Mar. 2004.

[12] S. Kitson, V. Cuccurullo, A. Ciarmiello, D. Salvo, and L. Mansi, "Clinical Applications of Positron Emission Tomography (PET) Imaging in Medicine: Oncology, Brain Diseases and Cardiology," *Curr. Radiopharm.*, vol. 2, no. 4, pp. 224–253, Oct. 2009.

[13] A. Kadir, O. Almkvist, A. Forsberg, A. Wall, H. Engler, B. Långström, and A. Nordberg, "Dynamic changes in PET amyloid and FDG imaging at different stages of Alzheimer's disease," *Neurobiol. Aging*, vol. 33, no. 1, p. 198.e1-198.e14, Jan. 2012.

[14] M. N. Wernick and J. N. Aarsvold, *Emission Tomography : The Fundamentals of PET and SPECT*. 2004.

[15] J. T. Bushberg, A. J. Seibert, E. M. Leidholdt, and J. M. Boone, *The Essential Physics of Medical Imaging*. Philadelphia: Lippincott Williams & Wilkins, 2002.

[16] P. M. Shikhaliev, "Computed tomography with energy-resolved detection: a feasibility study," *Phys. Med. Biol.*, vol. 53, no. 5, pp. 1475–1495, Mar. 2008.

[17] P. M. Shikhaliev, "Energy-resolved Computed Tomography: First Experimental Results," *Phys. Med. Biol.*, vol. 53, no. 20, pp. 5595–5613, 2008.

[18] M. Overdick, C. Baumer, K. J. Engel, J. Fink, C. Herrmann, H. Kruger, M. Simon, R. Steadman, and G. Zeitler, "Towards direct conversion detectors for medical imaging with X-rays," in *2008 IEEE Nuclear Science Symposium Conference Record*, 2008, pp. 1527–1535.

[19] G. B. Saha, *Basics of PET Imaging: Physics, Chemistry, and Regulations*, 3rd

ed. Cleveland, OH, USA: Springer International Publishing, 2015.

[20] J. S. Kim, J. S. Lee, K. C. Im, S. J. Kim, S.-Y. Kim, D. S. Lee, and D. H. Moon, "Performance Measurement of the microPET Focus 120 Scanner," *J. Nucl. Med.*, vol. 48, no. 9, pp. 1527–1535, Sep. 2007.

[21] Y. Gu, "High-Resolution Small Animal Positron Emission Tomography System Based on 3-D Position-Sensitive Cadmium Zinc Telluride Photon Detectors," Stanford University, 2014.

[22] V. C. Spanoudaki and C. S. Levin, "Photo-Detectors for Time of Flight Positron Emission Tomography (ToF-PET)," *Sensors*, vol. 10, no. 11, pp. 10484–10505, Nov. 2010.

[23] C. S. Levin and E. J. Hoffman, "Calculation of positron range and its effect on the fundamental limit of positron emission tomography system spatial resolution.," *Phys. Med. Biol.*, vol. 44, no. 3, pp. 781–99, Mar. 1999.

[24] S. R. Cherry, J. A. Sorenson, and M. E. Phelps, *Physics in Nuclear Medicine*, 4th ed. Philadelphia, PA, USA: Elsevier, 2012.

[25] G. F. Knoll, *Radiation Detection and Measurement*, 4th ed. Michigan, USA: Wiley, 2011.

[26] J. Langner, "Development of a parallel computing optimized head movement correction method in positron-emission-tomography," University of Applied Sciences, 2003.

[27] Wikipedia, "Positron emission tomography," 2016. .

[28] D. L. Bailey, D. W. Townsend, P. E. Valk, and M. N. Maisey, *Positron Emission Tomography: Basic Sciences*. London: Springer-Verlag London Limited, 2005.

[29] M. Magdy and Khalil, *Basic sciences of nuclear medicine*. Springer-Verlag Berlin Heidelberg, 2011.

[30] S. E. Derenzo, M. J. Weber, E. Bourret-Courchesne, and M. K. Klintenberg, "The quest for the ideal inorganic scintillator," *Nucl. Instruments Methods Phys. Res. Sect. A Accel. Spectrometers, Detect. Assoc. Equip.*, vol. 505, no. 1–2, pp. 111–117, Jun. 2003.

[31] C. L. Melcher, "Scintillation crystals for PET.," *J. Nucl. Med.*, vol. 41, no. 6,

pp. 1051–5, Jun. 2000.

[32] W. W. Moses and S. . Derenzo, “Scintillators for positron emission tomography,” in *Proceedings of The Scint.*, 1995, pp. 234–237.

[33] M. Aykac, F. Bauer, C. W. Williams, M. Loope, and M. Schmand, “Timing performance of Hi-Rez detector for time-of-flight (TOF) PET,” *IEEE Trans. Nucl. Sci.*, vol. 53, no. 3, pp. 1084–1089, Jun. 2006.

[34] R. Lecomte, “Novel detector technology for clinical PET,” *Eur. J. Nucl. Med. Mol. Imaging*, vol. 36, no. S1, pp. 69–85, Mar. 2009.

[35] W. W. Moses, “Current trends in scintillator detectors and materials,” *Nucl. Instruments Methods Phys. Res. Sect. A Accel. Spectrometers, Detect. Assoc. Equip.*, vol. 487, no. 1–2, pp. 123–128, Jul. 2002.

[36] T. Ludziejewski, K. Moszynska, M. Moszynski, D. Wolski, W. Klamra, L. O. Norlin, E. Devitsin, and V. Kozlov, “Advantages and limitations of LSO scintillator in nuclear physics experiments,” *IEEE Trans. Nucl. Sci.*, vol. 42, no. 4, pp. 328–336, 1995.

[37] Y. Shao, “A new timing model for calculating the intrinsic timing resolution of a scintillator detector,” *Phys. Med. Biol.*, vol. 52, no. 4, pp. 1103–1117, Feb. 2007.

[38] S. R. Cherry and M. Dahlbom, *PET: Physics, Instrumentation, and Scanners*. Springer Science Business Media, 2006.

[39] Z. Cheng, X. Zheng, D. Palubiak, M. J. Deen, and H. Peng, “A Comprehensive and Accurate Analytical SPAD Model for Circuit Simulation,” *IEEE Trans. Electron Devices*, vol. 63, no. 5, pp. 1940–1948, May 2016.

[40] D. Palubiak and M. J. Deen, “CMOS SPADs : Design Issues and Research Challenges for Detectors , Circuits , and Arrays,” *IEEE J. Sel. Top. Quantum Electron.*, vol. 20, no. 6, p. 6000718:1-6000718:18, 2014.

[41] D. Palubiak, M. M. El-Desouki, O. Marinov, M. J. Deen, and Q. Fang, “High-speed, single-photon avalanche-photodiode Imager for Biomedical Applications,” *IEEE Sens. J.*, vol. 11, no. 10, pp. 2401–2412, 2011.

[42] Z. Cheng, X. Zheng, M. J. Deen, and H. Peng, “Development of a High Performance Digital Silicon Photomultiplier (dSiPM) for ToF PET Imaging,”

J. Nucl. Med., vol. 56, no. supplement 3, p. 603, May 2015.

[43] M. J. Deen and P. K. Basu, *Silicon Photonics: Fundamentals and Devices*. West Sussex, United Kingdom: Wiley, 2012.

[44] Wikipedia, "Photomultiplier," 2016. .

[45] V. C. Spanoudaki and C. S. Levin, "Scintillation induced response in passively-quenched Si-based single photon counting avalanche diode arrays," *Opt. Express*, vol. 19, no. 2, p. 1665, Jan. 2011.

[46] W. R. Willig, "Mercury iodide as a gamma spectrometer," *Nucl. Instruments Methods*, vol. 96, no. 4, pp. 615–616, Nov. 1971.

[47] H. L. Malm, "A Mercuric Iodide Gamma-Ray Spectrometer," *IEEE Trans. Nucl. Sci.*, vol. 19, no. 3, pp. 263–265, 1972.

[48] K. Hull, A. Beyerle, B. Lopez, J. Markakis, C. Ortale, W. Schnepple, and L. van den Berg, "Recent Developments in Thick Mercuric Iodide Spectrometers," *IEEE Trans. Nucl. Sci.*, vol. 30, no. 1, pp. 402–404, 1983.

[49] P. Olmos, G. Garcia-Belmonte, J. M. Perez, and J. C. Diaz, "Use of thick HgI2 detectors as intelligent spectrometers," *Nucl. Instruments Methods Phys. Res. Sect. A Accel. Spectrometers, Detect. Assoc. Equip.*, vol. 299, no. 1–3, pp. 45–50, Dec. 1990.

[50] H. Zhong and R. D. Vigil, "Investigation of pixellated HgI2 gamma-ray spectrometers," *Nucl. Instruments Methods Phys. Res. A*, vol. 492, no. 3, pp. 387–401, 2002.

[51] J. E. Baciak and Zhong He, "Spectroscopy on thick HgI/sub 2/ detectors: a comparison between planar and pixelated electrodes," *IEEE Trans. Nucl. Sci.*, vol. 50, no. 4, pp. 1220–1224, Aug. 2003.

[52] Yuefeng Zhu, Willy Kaye, Zhong He, and Feng Zhang, "Stability and characteristics of 3D HgI2 detectors at different cathode bias," in *2007 IEEE Nuclear Science Symposium Conference Record*, 2007, pp. 1537–1540.

[53] M. R. Saleno, L. van den Berg, R. D. Vigil, J. T. Baker, W. R. Kaye, Y. Zhu, F. Zhang, and Z. He, "Use of pixelated detectors for the identification of defects and charge collection effects in mercuric iodide (HgI2) single crystal material," *Nucl. Instruments Methods Phys. Res. Sect. A Accel. Spectrometers,*

Detect. Assoc. Equip., vol. 652, no. 1, pp. 197–200, Oct. 2011.

[54] C. L. Thrall, W. R. Kaye, Z. He, H. Kim, L. Cirignano, and K. Shah, "Transient Behavior in TlBr Gamma-Ray Detectors and Its Analysis Using 3-D Position Sensing," *IEEE Trans. Nucl. Sci.*, vol. 60, no. 2, pp. 1162–1167, Apr. 2013.

[55] H. Kim, A. Churilov, G. Ciampi, L. Cirignano, W. Higgins, S. Kim, P. O'Dougherty, F. Olschner, and K. Shah, "Continued development of thallium bromide and related compounds for gamma-ray spectrometers," *Nucl. Instruments Methods Phys. Res. Sect. A Accel. Spectrometers, Detect. Assoc. Equip.*, vol. 629, no. 1, pp. 192–196, Feb. 2011.

[56] K. Hitomi, Y. Kikuchi, T. Shoji, and K. Ishii, "Polarization Phenomena in TlBr Detectors," *IEEE Trans. Nucl. Sci.*, vol. 56, no. 4, pp. 1859–1862, Aug. 2009.

[57] B. Donmez, C. L. Thrall, Zhong He, L. J. Cirignano, Hadong Kim, and K. S. Shah, "Investigation of polarization effect with TlBr detectors at different operating temperatures," in *IEEE Nuclear Science Symposuim & Medical Imaging Conference*, 2010, pp. 3773–3775.

[58] F. Zhang, C. Herman, Z. He, G. De Geronimo, E. Vernon, and J. Fried, "Characterization of the H3D ASIC Readout System and 6.0 cm<formula formulatype='inline'><tex Notation='TeX'>^{3}</tex></formula> 3-D Position Sensitive CdZnTe Detectors," *IEEE Trans. Nucl. Sci.*, vol. 59, no. 1, pp. 236–242, Feb. 2012.

[59] R. H. Redus, J. A. Pantazis, A. C. Huber, V. T. Jordanov, J. F. Butler, and B. Apotovsky, "Fano factor determination for CZT," in *Material research society symposium proceedings: Semiconductors for room-temperature radiation detector applications II*, 1997, pp. 101–107.

[60] E. C. McCullough, "Photon attenuation in computed tomography," *Med. Phys.*, vol. 2, no. 6, pp. 307–320, Nov. 1975.

[61] M. Soleimani and T. Pengpen, "Introduction: a brief overview of iterative algorithms in X-ray computed tomography," *Philos. Trans. R. Soc. A Math. Phys. Eng. Sci.*, vol. 373, no. 2043, pp. 20140399–20140399, May 2015.

[62] L. W. Goldman, "Principles of CT and CT Technology," *J. Nucl. Med.*

Technol., vol. 35, no. 3, pp. 115–128, Sep. 2007.

[63] W. A. Kalender, *Computed Tomography: Fundamentals, System Technology, Image Quality, Applications*, 3rd ed. Wiley, 2011.

[64] K. Iniewski, *Medical Imaging: Principles, Detectors, and Electronics*. Wiley, 2009.

[65] J. P. Schlomka, E. Roessl, R. Dorscheid, S. Dill, G. Martens, T. Istel, C. Bäumer, C. Herrmann, R. Steadman, G. Zeitler, A. Livne, and R. Proksa, "Experimental feasibility of multi-energy photon-counting K-edge imaging in pre-clinical computed tomography," *Phys. Med. Biol.*, vol. 53, no. 15, pp. 4031–4047, Aug. 2008.

[66] P. M. Shikhaliev, "Energy-resolved computed tomography: first experimental results," *Phys. Med. Biol.*, vol. 53, no. 20, pp. 5595–5613, Oct. 2008.

[67] K. Taguchi and J. S. Iwanczyk, "Vision 20/20: Single photon counting x-ray detectors in medical imaging," *Med. Phys.*, vol. 40, no. 10, p. 100901, Sep. 2013.

[68] M. J. Tapiovaara and R. Wagner, "SNR and DQE analysis of broad spectrum X-ray imaging," *Phys. Med. Biol.*, vol. 30, no. 6, pp. 519–529, Jun. 1985.

[69] P. M. Shikhaliev, "Tilted angle CZT detector for photon counting/energy weighting x-ray and CT imaging," *Phys. Med. Biol.*, vol. 51, no. 17, pp. 4267–4287, Sep. 2006.

[70] J. F. Butler, C. L. Lingren, and F. P. Doty, "Cd/sub 1-x/Zn/sub x/Te gamma ray detectors," in *Conference Record of the 1991 IEEE Nuclear Science Symposium and Medical Imaging Conference*, pp. 129–133.

[71] J. . Toney, B. . Brunett, T. . Schlesinger, J. . Van Scyoc, R. . James, M. Schieber, M. Goorsky, H. Yoon, E. Eissler, and C. Johnson, "Uniformity of Cd1 − xZnxTe grown by high-pressure Bridgman," *Nucl. Instruments Methods Phys. Res. Sect. A Accel. Spectrometers, Detect. Assoc. Equip.*, vol. 380, no. 1–2, pp. 132–135, Oct. 1996.

[72] S. Del Sordo, L. Abbene, E. Caroli, A. M. Mancini, A. Zappettini, and P. Ubertini, "Progress in the Development of CdTe and CdZnTe Semiconductor Radiation Detectors for Astrophysical and Medical Applications.," *Sensors*

(Basel)., vol. 9, no. 5, pp. 3491–526, Jan. 2009.

[73] V. . Jordanov, J. . Pantazis, and A. . Huber, "Compact circuit for pulse rise-time discrimination," *Nucl. Instruments Methods Phys. Res. Sect. A Accel. Spectrometers, Detect. Assoc. Equip.*, vol. 380, no. 1–2, pp. 353–357, Oct. 1996.

[74] M. Richter and P. Siffert, "High resolution gamma ray spectroscopy with CdTe detector systems," *Nucl. Instruments Methods Phys. Res. Sect. A Accel. Spectrometers, Detect. Assoc. Equip.*, vol. 322, no. 3, pp. 529–537, Nov. 1992.

[75] N. Auricchio, L. Amati, A. Basili, E. Caroli, A. Donati, T. Franceschini, F. Frontera, G. Landini, A. Roggio, F. Schiavone, J. B. Stephen, and G. Ventura, "Twin shaping filter techniques to compensate the signals from CZT/CdTe detectors," *IEEE Trans. Nucl. Sci.*, vol. 52, no. 5, pp. 1982–1988, Oct. 2005.

[76] D. S. McGregor, Z. He, H. A. Seifert, D. K. Wehe, and R. A. Rojeski, "Single charge carrier type sensing with a parallel strip pseudo-Frisch-grid CdZnTe semiconductor radiation detector," *Appl. Phys. Lett.*, vol. 72, no. 7, pp. 792–794, Feb. 1998.

[77] A. E. Bolotnikov, G. C. Camarda, G. A. Carini, M. Fiederle, L. Li, D. S. McGregor, W. McNeil, G. W. Wright, and R. B. James, "Performance characteristics of Frisch-ring CdZnTe detectors," *IEEE Trans. Nucl. Sci.*, vol. 53, no. 2, pp. 607–614, Apr. 2006.

[78] H. Barrett, J. Eskin, and H. Barber, "Charge Transport in Arrays of Semiconductor Gamma-Ray Detectors," *Phys. Rev. Lett.*, vol. 75, no. 1, pp. 156–159, Jul. 1995.

[79] L. Abbene, S. Del Sordo, G. Agnetta, B. Biondo, E. Caroli, A. Mangano, F. Russo, J. B. Stephen, G. Ventura, A. Carlino, G. Gerardi, and G. Bertuccio, "Investigation on pixellated CZT detectors coupled with a low power readout ASIC," in *2008 IEEE Nuclear Science Symposium Conference Record*, 2008, pp. 478–483.

[80] P. N. Luke, "Unipolar charge sensing with coplanar electrodes-application to semiconductor detectors," *IEEE Trans. Nucl. Sci.*, vol. 42, no. 4, pp. 207–213, 1995.

[81] a. Shor, Y. Eisen, and I. Mardor, "Optimum spectroscopic performance from CZT ??- and X-ray detectors with pad and strip segmentation," *Nucl. Instruments Methods Phys. Res. Sect. A Accel. Spectrometers, Detect. Assoc. Equip.*, vol. 428, no. 1, pp. 182–192, 1999.

[82] E. Perillo, A. Cola, A. Donati, W. Dusi, G. Landini, A. Raulo, G. Ventura, and S. Vitulli, "Spectroscopic response of a CdTe microstrip detector when irradiated at various impinging angles," *Nucl. Instruments Methods Phys. Res. Sect. A Accel. Spectrometers, Detect. Assoc. Equip.*, vol. 531, no. 1–2, pp. 125–133, Sep. 2004.

[83] C. L. Lingren, B. Apotovsky, J. F. Butler, R. Conwell, F. P. Doty, S. J. Friesenhahn, A. Oganesyan, B. Pi, and S. Zhao, "Cadmium-zinc-telluride, multiple-electrode detectors achieve good energy resolution with high sensitivity at room-temperature," *IEEE Trans. Nucl. Sci.*, vol. 45, no. 3, pp. 433–437, Jun. 1998.

[84] H. Kim, L. Cirignano, K. Shah, M. Squillante, and P. Wong, "Investigation of the energy resolution and charge collection efficiency of Cd(Zn)Te detectors with three electrodes," *IEEE Trans. Nucl. Sci.*, vol. 51, no. 3, pp. 1229–1234, Jun. 2004.

[85] L. Abbene, S. Del Sordo, F. Fauci, G. Gerardi, A. La Manna, G. Raso, A. Cola, E. Perillo, A. Raulo, V. Gostilo, and S. Stumbo, "Spectroscopic response of a CdZnTe multiple electrode detector," *Nucl. Instruments Methods Phys. Res. Sect. A Accel. Spectrometers, Detect. Assoc. Equip.*, vol. 583, no. 2–3, pp. 324–331, Dec. 2007.

[86] M. A. J. van Pamelen and C. Budtz-Jørgensen, "CdZnTe drift detector with correction for hole trapping," *Nucl. Instruments Methods Phys. Res. Sect. A Accel. Spectrometers, Detect. Assoc. Equip.*, vol. 411, no. 1, pp. 197–200, Jul. 1998.

[87] C. S. Levin, A. M. K. Foudray, and F. Habte, "Impact of high energy resolution detectors on the performance of a PET system dedicated to breast cancer imaging," *Phys. Med.*, vol. 21, no. SUPPL. 1, pp. 28–34, 2006.

[88] A. J. Ball, S. Gadomski, M. Banaszkiewicz, T. Spohn, T. J. Ahrens, M.

Whyndham, and J. C. Zarnecki, "An instrument for in situ comet nucleus surface density profile measurement by gamma ray attenuation," *Planet. Space Sci.*, vol. 49, no. 9, pp. 961–976, Aug. 2001.

[89] R. D. Evans, *The Atomic Nucleus*. New York: Krieger, 1982.

[90] S. Jan, G. Santin, D. Strul, S. Staelens, K. Assié, D. Autret, S. Avner, R. Barbier, M. Bardiès, P. M. Bloomfield, D. Brasse, V. Breton, P. Bruyndonckx, I. Buvat, A. F. Chatziioannou, Y. Choi, Y. H. Chung, C. Comtat, D. Donnarieix, L. Ferrer, S. J. Glick, C. J. Groiselle, D. Guez, P. F. Honore, S. Kerhoas-Cavata, A. S. Kirov, V. Kohli, M. Koole, M. Krieguer, D. J. van der Laan, F. Lamare, G. Largeron, C. Lartizien, D. Lazaro, M. C. Maas, L. Maigne, F. Mayet, F. Melot, C. Merheb, E. Pennacchio, J. Perez, U. Pietrzyk, F. R. Rannou, M. Rey, D. R. Schaart, C. R. Schmidtlein, L. Simon, T. Y. Song, J. M. Vieira, D. Visvikis, R. Van de Walle, E. Wieërs, and C. Morel, "GATE: a simulation toolkit for PET and SPECT.," *Phys. Med. Biol.*, vol. 49, no. 19, pp. 4543–61, Oct. 2004.

[91] J. R. Stickel and S. R. Cherry, "High-resolution PET detector design: modelling components of intrinsic spatial resolution," *Phys. Med. Biol.*, vol. 50, no. 2, pp. 179–195, Jan. 2005.

[92] C. K. Jen, "On the Induced Current and Energy Balance in Electronics," *Proc. IRE*, vol. 29, no. 6, pp. 345–349, Jun. 1941.

[93] G. Cavalleri, E. Gatti, G. Fabri, and V. Svelto, "Extension of Ramo's theorem as applied to induced charge in semiconductor detectors," *Nucl. Instruments Methods*, vol. 92, no. 1, pp. 137–140, Mar. 1971.

[94] Y. Gu, "Studies of Electrode Design for a Sub-mm Resolution 3-D Position Sensitive CZT PET Detector," in *IEEE Nuclear Science Symposium Conference Record*, 2011, pp. 2303–2305.

[95] Z. He, G. F. Knoll, D. K. Wehe, R. Rojeski, C. H. Mastrangelo, M. Hammig, C. Barrett, and A. Uritani, "1-D position sensitive single carrier semiconductor detectors," *Nucl. Instruments Methods Phys. Res. Sect. A Accel. Spectrometers, Detect. Assoc. Equip.*, vol. 380, no. 1–2, pp. 228–231, Oct. 1996.

[96] Z. He, G. F. Knoll, D. K. Wehe, and J. Miyamoto, "Position-sensitive single

carrier CdZnTe detectors," *Nucl. Instruments Methods Phys. Res. A*, vol. 388, pp. 180–185, 1997.

[97] Z. He, F. Zhang, C. Lehner, D. Xu, G. F. Knoll, and D. K. Wehe, "3-D Position-Sensitive CdZnTe γ-Ray Spectrometers."

[98] W. Li, Z. He, G. F. Knoll, D. K. Wehe, and C. M. Stahle, "Spatial variation of energy resolution in 3-D position sensitive CZT gamma-ray spectrometers," *IEEE Trans. Nucl. Sci.*, vol. 46, no. 3, pp. 187–192, Jun. 1999.

[99] Z. He, W. Li, G. F. Knoll, D. K. Wehe, and C. M. Stahle, "Measurement of material uniformity using 3-D position sensitive CdZnTe gamma-ray spectrometers," *Nucl. Instruments Methods Phys. Res. Sect. A Accel. Spectrometers, Detect. Assoc. Equip.*, vol. 441, no. 3, pp. 459–467, Mar. 2000.

[100] W. Li, Z. He, G. F. Knoll, D. K. Wehe, and Y. F. Du, "A modeling method to calibrate the interaction depth in 3-Dposition sensitive CdZnTe gamma-ray spectrometers," *IEEE Trans. Nucl. Sci.*, vol. 47, no. 3, pp. 890–894, 2000.

[101] H. Chen, S. a. Awadalla, J. Mackenzie, R. Redden, G. Bindley, a. E. Bolotnikov, G. S. Camarda, G. Carini, and R. B. James, "Characterization of Traveling Heater Method (THM) grown $Cd_{0.9}Zn_{0.1}Te$ crystals," *IEEE Trans. Nucl. Sci.*, vol. 54, no. 4, pp. 811–816, 2007.

[102] "ZEBRA® W Series Matrix Connectors." [Online]. Available: http://www.fujipoly.com/usa/products/zebra-elastomeric-connectors/w-series-connectors.html.

[103] S. N. Ahmed, *Physics and Engineering of Radiation Detection*. Burlington: Elsevier Science, 2007.

[104] W. Hu, Y. Choi, J. H. Jung, J. H. Kang, B. J. Min, Y. S. Huh, S. H. Shin, H. K. Lim, and Y. H. Chung, "A simple and improved digital timing method for positron emission tomography," in *2009 IEEE Nuclear Science Symposium Conference Record (NSS/MIC)*, 2009, pp. 3893–3896.

[105] A. Codino, "The pulse digitization for measuring the time of flight of ionizing particles," *Nucl. Instruments Methods Phys. Res. Sect. A Accel. Spectrometers, Detect. Assoc. Equip.*, vol. 440, no. 1, pp. 191–201, Jan. 2000.

[106] M. A. Nelson, B. D. Rooney, D. R. Dinwiddie, and G. S. Brunson, "Analysis

of digital timing methods with BaF2 scintillators," *Nucl. Instruments Methods Phys. Res. Sect. A Accel. Spectrometers, Detect. Assoc. Equip.*, vol. 505, no. 1–2, pp. 324–327, Jun. 2003.

[107] A. Fallu-Labruyere, H. Tan, W. Hennig, and W. K. Warburton, "Time resolution studies using digital constant fraction discrimination," *Nucl. Instruments Methods Phys. Res. Sect. A Accel. Spectrometers, Detect. Assoc. Equip.*, vol. 579, no. 1, pp. 247–251, Aug. 2007.

[108] H. Peng, P. D. Olcott, A. M. K. Foudray, and C. S. Levin, "Evaluation of free-running ADCs for high resolution PET data acquisition," in *2007 IEEE Nuclear Science Symposium Conference Record*, 2007, pp. 3328–3331.

[109] V. B. Cajipe, M. Clajus, S. Hayakawa, J. L. Matteson, R. T. Skelton, T. O. Tumer, and A. Volkovskii, "Performance of the RENA-3 IC with position-sensitive CZT and CdTe detectors," *2008 IEEE Nucl. Sci. Symp. Conf. Rec.*, pp. 300–307, 2008.

[110] Y. Du, W. Li, B. Yanoff, J. Gordon, and D. Castleberry, "4 Pi Direction Sensitive Gamma Imager with RENA-3 Readout ASIC," *Proc. SPIE*, vol. 6706, p. 67060V–67060V–10, Sep. 2007.

[111] S. D. Kravis, T. O. Tümer, G. Visser, D. G. Maeding, and S. Yin, "A multichannel readout electronics for nuclear application (RENA) chip developed for position sensitive solid state detectors," *Nucl. Instruments Methods Phys. Res. Sect. A Accel. Spectrometers, Detect. Assoc. Equip.*, vol. 422, no. 1–3, pp. 352–356, Feb. 1999.

[112] T. O. Tumer, V. B. Cajipe, M. Clajus, F. Duttweiler, S. Hayakawa, J. L. Matteson, A. Shirley, and O. Yossifor, "Test results of a CdZnTe pixel detector read out by RENA-2 IC," in *IEEE Symposium Conference Record Nuclear Science 2004.*, vol. 7, pp. 4369–4372.

[113] S. D. Kravis, T. O. Tumer, G. Visser, D. G. Maeding, and Shi Yin, "Readout electronics for nuclear applications (RENA) chip," in *1997 IEEE Nuclear Science Symposium Conference Record*, pp. 700–703.

[114] N. Auricchio, A. Donati, W. Dusi, E. Perillo, and P. Siffert, "A comparison between the response of compound semiconductor detectors in single and

back-to-back configuration," *Nucl. Instruments Methods Phys. Res. Sect. B Beam Interact. with Mater. Atoms*, vol. 213, pp. 272–278, Jan. 2004.

[115] N. Auricchio, A. Basili, E. Caroli, C. Budtz-Jorgensen, R. M. C. da Silva, S. Del Sordo, I. Kuvvetli, A. Mangano, L. Milano, L. Natalucci, E. M. Quadrini, J. B. Stephen, M. Zanichelli, and A. Zappettini, "A CZT high efficiency detector with 3D spatial resolution for Laue lens applications," in *IEEE Nuclear Science Symposuim & Medical Imaging Conference*, 2010, pp. 3683–3688.

[116] F. Casali, D. Bollini, P. Chirco, M. Rossi, G. Baldazzi, W. Dusi, E. Caroli, G. DiCocco, A. Donati, G. Landini, and J. B. Stephen, "Characterization of small CdTe detectors to be used for linear and matrix arrays," in *Conference Record of the 1991 IEEE Nuclear Science Symposium and Medical Imaging Conference*, pp. 75–81.

[117] I. Kuvvetli, C. Budtz-Jørgensen, E. Caroli, and N. Auricchio, "CZT drift strip detectors for high energy astrophysics," *Nucl. Instruments Methods Phys. Res. Sect. A Accel. Spectrometers, Detect. Assoc. Equip.*, vol. 624, no. 2, pp. 486–491, Dec. 2010.

[118] M. Nakhostin, Y. Kikuchi, K. Ishii, S. Matsuyama, and H. Yamazaki, "Development of a digital front-end electronics for the CdTe PET systems," *Nucl. Instruments Methods Phys. Res. Sect. A Accel. Spectrometers, Detect. Assoc. Equip.*, vol. 614, no. 2, pp. 308–312, Mar. 2010.

[119] K. Ishii, Y. Kikuchi, K. Takahashi, K. Nakamura, S. Matsuyama, A. Terakawa, H. Yamazaki, and K. Hitomi, "Development of a new two-dimensional position-sensitive detection based on resistive charge division and using CdTe detectors for a high-resolution semiconductor-based PET scanning," *Nucl. Instruments Methods Phys. Res. Sect. A Accel. Spectrometers, Detect. Assoc. Equip.*, vol. 631, no. 1, pp. 138–143, Mar. 2011.

[120] E. Abuelhia, K. Alzimami, M. Alkhorayef, Z. Podolyák, and N. M. Spyrou, "Measurement of coincidence timing resolution of scintillation detectors compared to semiconductor detectors to image three-photon positron annihilation," *J. Radioanal. Nucl. Chem.*, vol. 278, no. 3, pp. 767–771, Dec.

2008.

[121] L. J. Meng and Z. He, "Exploring the limiting timing resolution for large volume CZT detectors with waveform analysis," *Nucl. Instruments Methods Phys. Res. Sect. A Accel. Spectrometers, Detect. Assoc. Equip.*, vol. 550, no. 1–2, pp. 435–445, Sep. 2005.

[122] Y. Okada, T. Takahashi, G. Sato, S. Watanabe, K. Nakazawa, K. Mori, and K. Makishima, "CdTe and CdZnTe detectors for timing measurements," *IEEE Trans. Nucl. Sci.*, vol. 49, no. 4, pp. 1986–1992, Aug. 2002.

[123] G. Ariño, M. Chmeissani, G. De Lorenzo, C. Puigdengoles, E. Cabruja, Y. Calderón, M. Kolstein, J. G. Macias-Montero, R. Martinez, E. Mikhaylova, and D. Uzun, "Energy and coincidence time resolution measurements of CdTe detectors for PET," *J. Instrum.*, vol. 8, no. 2, pp. C02015–C02015, Feb. 2013.

[124] S. Komarov, Y. Yin, H. Wu, J. Wen, H. Krawczynski, L.-J. Meng, and Y.-C. Tai, "Investigation of the limitations of the highly pixilated CdZnTe detector for PET applications.," *Phys. Med. Biol.*, vol. 57, no. 22, pp. 7355–80, 2012.

[125] C. S. Levin, "New imaging technologies to rnhance the molecular sensitivity of Positron Emission Tomography.," *Proc. IEEE*, vol. 96, no. 3, pp. 439–467, 2008.

[126] M. Maiorino, G. Pellegrini, G. Blanchot, M. Chmeissani, and J. Garcia, "Charge-Sharing Observations with a CdTe Pixel Detector Irradiated with a 57 Co Source."

[127] B. Yu, R. Beuttenmuller, W. Chen, D. C. Elliott, Z. Li, J. A. Mead, V. Radeka, M. E. Vazquez, K. A. Brown, and A. Rusek, "A novel 2D position sensitive silicon detector with micron resolution for heavy ion tracking," in *IEEE Symposium Conference Record Nuclear Science 2004.*, vol. 2, pp. 1165–1169.

[128] M. C. Veale, S. J. Bell, D. D. Duarte, A. Schneider, P. Seller, M. D. Wilson, and K. Iniewski, "Measurements of charge sharing in small pixel CdTe detectors," *Nucl. Inst. Methods Phys. Res. A*, vol. 767, pp. 218–226, 2014.

[129] C. Allwork, D. Kitou, S. Chaudhuri, P. J. Sellin, P. Seller, M. C. Veale, N. Tartoni, and P. Veeramani, "X-Ray Beam Studies of Charge Sharing in Small Pixel, Spectroscopic, CdZnTe Detectors," *IEEE Trans. Nucl. Sci.*, vol. 59, no.

4, pp. 1563–1568, Aug. 2012.

[130] Y. Gu and C. S. Levin, "Study of electrode pattern design for a CZT-based PET detector," *Phys. Med. Biol.*, vol. 59, no. 11, pp. 2599–2621, Jun. 2014.

[131] C. S. Williams, W. P. Baker, L. W. Burggraf, P. E. Adamson, and J. C. Petrosky, "Toward Simultaneous 2D ACAR and 2D DBAR: Sub-Pixel Spatial Characterization of a Segmented HPGe Detector Using Transient Charges," *IEEE Trans. Nucl. Sci.*, vol. 57, no. 2, pp. 860–869, Apr. 2010.

[132] T. Narita, J. E. Grindlay, J. Hong, and F. C. Niestemski, "Anode readout for pixellated CZT detectors," 2004, p. 542.

[133] W. K. Warburton, "An Approach to Sub-Pixel Spatial Resolution in Room Temperature X-Ray Detector Arrays with Good Energy Resolution," *MRS Proc.*, vol. 487, p. 531, Jan. 1997.

[134] Y. Zhu, S. E. Anderson, and Z. He, "Sub-pixel position sensing for pixelated, 3-D position sensitive, wide band-gap, semiconductor, gamma-ray detectors," *IEEE Trans. Nucl. Sci.*, vol. 58, no. 3 PART 3, pp. 1400–1409, 2011.

[135] J. C. Kim, S. E. Anderson, W. Kaye, S. J. Kaye, Y. Zhu, F. Zhang, A. P. Signals, and C. Detectors, "Study on Effect of Charge Sharing Events in Common-Grid Pixelated CdZnTe Detectors," pp. 1640–1646, 2009.

[136] M. Burks, E. Jordan, E. Hull, L. Mihailescu, and K. Vetter, "Signal interpolation in germanium detectors for improved 3-D position resolution," in *IEEE Symposium Conference Record Nuclear Science 2004.*, vol. 2, pp. 1114–1118.

[137] E. Kalemci and J. . Matteson, "Investigation of charge sharing among electrode strips for a CdZnTe detector," *Nucl. Instruments Methods Phys. Res. Sect. A Accel. Spectrometers, Detect. Assoc. Equip.*, vol. 478, no. 3, pp. 527–537, Feb. 2002.

[138] A. Meuris, O. Limousin, and C. Blondel, "Charge sharing in CdTe pixilated detectors," *Nucl. Instruments Methods Phys. Res. Sect. A Accel. Spectrometers, Detect. Assoc. Equip.*, vol. 610, no. 1, pp. 294–297, Oct. 2009.

[139] T. R. C. Johnson, B. Krauß, M. Sedlmair, M. Grasruck, H. Bruder, D. Morhard, C. Fink, S. Weckbach, M. Lenhard, B. Schmidt, T. Flohr, M. F.

Reiser, and C. R. Becker, “Material differentiation by dual energy CT: initial experience,” *Eur. Radiol.*, vol. 17, no. 6, pp. 1510–1517, May 2007.

[140] S. Leschka, P. Stolzmann, F. T. Schmid, H. Scheffel, B. Stinn, B. Marincek, H. Alkadhi, and S. Wildermuth, “Low kilovoltage cardiac dual-source CT: attenuation, noise, and radiation dose,” *Eur. Radiol.*, vol. 18, no. 9, pp. 1809–1817, Sep. 2008.

[141] R. K. Kaza, E. M. Caoili, R. H. Cohan, and J. F. Platt, “Distinguishing Enhancing From Nonenhancing Renal Lesions With Fast Kilovoltage-Switching Dual-Energy CT,” *Am. J. Roentgenol.*, vol. 197, no. 6, pp. 1375–1381, Dec. 2011.

[142] L. L. Geyer, M. Scherr, M. Körner, S. Wirth, P. Deak, M. F. Reiser, and U. Linsenmaier, “Imaging of acute pulmonary embolism using a dual energy CT system with rapid kVp switching: Initial results,” *Eur. J. Radiol.*, vol. 81, no. 12, pp. 3711–3718, Dec. 2012.

[143] L.-J. Zhang, J. Peng, S.-Y. Wu, Z. J. Wang, X.-S. Wu, C.-S. Zhou, X.-M. Ji, and G.-M. Lu, “Liver virtual non-enhanced CT with dual-source, dual-energy CT: a preliminary study,” *Eur. Radiol.*, vol. 20, no. 9, pp. 2257–2264, Sep. 2010.

[144] A. N. Primak, J. C. Ramirez Giraldo, X. Liu, L. Yu, and C. H. McCollough, “Improved dual-energy material discrimination for dual-source CT by means of additional spectral filtration,” *Med. Phys.*, vol. 36, no. 4, p. 1359, 2009.

[145] M. Qu, J. C. Ramirez-Giraldo, S. Leng, J. C. Williams, T. J. Vrtiska, J. C. Lieske, and C. H. McCollough, “Dual-Energy Dual-Source CT With Additional Spectral Filtration Can Improve the Differentiation of Non–Uric Acid Renal Stones: An Ex Vivo Phantom Study,” *Am. J. Roentgenol.*, vol. 196, no. 6, pp. 1279–1287, Jun. 2011.

[146] S. Lee, Y.-N. Choi, and H.-J. Kim, “Quantitative material decomposition using spectral computed tomography with an energy-resolved photon-counting detector,” *Phys. Med. Biol.*, vol. 59, no. 18, pp. 5457–5482, Sep. 2014.

[147] M. D. Wilson, R. Cernik, H. Chen, C. Hansson, K. Iniewski, L. L. Jones, P. Seller, and M. C. Veale, “Small pixel CZT detector for hard X-ray

spectroscopy," *Nucl. Instruments Methods Phys. Res. Sect. A Accel. Spectrometers, Detect. Assoc. Equip.*, vol. 652, no. 1, pp. 158–161, Oct. 2011.

[148] M. D. Wilson, P. Seller, M. C. Veale, and P. J. Sellin, "Investigation of the small pixel effect in CdZnTe detectors," in *2007 IEEE Nuclear Science Symposium Conference Record*, 2007, pp. 1255–1259.

[149] D. Palubiak, M. M. El-Desouki, O. Marinov, M. J. Deen, and Q. Fang, "High-Speed, Single-Photon Avalanche-Photodiode Imager for Biomedical Applications," *IEEE Sens. J.*, vol. 11, no. 10, pp. 2401–2412, Oct. 2011.

[150] T. G. Schmidt, "CT energy weighting in the presence of scatter and limited energy resolution," *Med. Phys.*, vol. 37, no. 3, p. 1056, 2010.

[151] X. Zheng, Z. Cheng, M. J. Deen, and H. Peng, "Improving the spatial resolution in CZT detectors using charge sharing effect and transient signal analysis: Simulation study," *Nucl. Instruments Methods Phys. Res. Sect. A Accel. Spectrometers, Detect. Assoc. Equip.*, vol. 808, pp. 60–70, Feb. 2016.

[152] P. M. Shikhaliev, S. G. Fritz, and J. W. Chapman, "Photon counting multienergy x-ray imaging: Effect of the characteristic x rays on detector performance," *Med. Phys.*, vol. 36, no. 11, p. 5107, 2009.

[153] M. O. Krause, "Atomic radiative and radiationless yields for K and L shells," *J. Phys. Chem. Ref. Data*, vol. 8, no. 2, p. 307, 1979.

[154] C. M. H. Chen, S. E. Boggs, A. E. Bolotnikov, W. R. C. Iii, F. A. Harrison, and S. M. Schindler, "Numerical Modelling of Charge-Sharing in CdZnTe Pixel Detectors."

[155] E. Gros d'Aillon, J. Tabary, A. Glière, and L. Verger, "Charge sharing on monolithic CdZnTe gamma-ray detectors: A simulation study," *Nucl. Instruments Methods Phys. Res. Sect. A Accel. Spectrometers, Detect. Assoc. Equip.*, vol. 563, no. 1, pp. 124–127, Jul. 2006.

[156] P. Guerra, a Santos, and D. G. Darambara, "Development of a simplified simulation model for performance characterization of a pixellated CdZnTe multimodality imaging system.," *Phys. Med. Biol.*, vol. 53, no. 4, pp. 1099–1113, Feb. 2008.

[157] A. Glière, A. Koenig, F. Mathy, and P. Hugonnard, "A Physics Based Model

of Pixellated Semiconductor Gamma Camera," no. 3, pp. 1–5, 2000.

[158] C. Xu, M. Danielsson, and H. Bornefalk, "Evaluation of energy loss and charge sharing in cadmium telluride detectors for photon-counting computed tomography," *IEEE Trans. Nucl. Sci.*, vol. 58, no. 3 PART 1, pp. 614–625, 2011.

[159] F. Zhang, Z. He, S. Member, D. Xu, and L. J. Meng, "Feasibility Study of Using Two 3-D Position Sensitive CZT Detectors for Small Animal PET," in *IEEE Nuclear Science Symposium Conference Record*, 2005, pp. 1582–1585.

[160] S. G. Fritz and P. M. Shikhaliev, "CZT detectors used in different irradiation geometries: Simulations and experimental results," *Med. Phys.*, vol. 36, no. 4, p. 1098, 2009.